Skoltech

Proceedings of the Skoltech Energy PhD Seminar

2019/20

УДК 620.9(082)
ББК 31.1я43
Р93

ISBN 978-5-902271-33-8

The Proceedings is a collection of the original research papers written by the participants of the third Skoltech PhD Energy Seminar in the 2019-2020 academic year.

УДК 620.9(082)
ББК 31.1я43

ISBN 978-5-6042289-2-0

Proceedings of the Skoltech Energy PhD Seminar 2019/20

The Proceedings is a collection of the original research papers written by the participants of the forth Skoltech Energy PhD Seminar in the 2019-2020 academic year.

The Skoltech PhD Energy Seminar unites students enrolled on Skoltech PhD Programs associated with the Centers of Energy Science and Technology, Hydrocarbon Recovery, Photonics & Quantum Materials, and eventually some others.

The Seminar promotes the exchange of knowledge, methodologies, and research questions across the fundamentally different scientific areas in accordance with the Skoltech vision of multidisciplinary research and education oriented to innovation. The main goal of the Seminar is to create and maintain interdisciplinary links between students doing research related to energy resources, generation, storage and distribution, as well as methods, models, devices and materials for efficient energy use.

Besides its immediate research-oriented goal, the pragmatic aim of the Seminar is to engage PhD students in professional academic communication activities based on the principles of ethics and peer review. During the Seminar, students were required to present the results of their research, write an article for the Proceedings according to a template, and peer review two papers submitted by the Seminar participants.

In preparation for the Proceedings, each paper was anonymously reviewed by two peers and checked by a language instructor. The final versions had to incorporate comments from the referees and editors to be accepted for the Proceedings.

We believe that this exercise provides the students with useful experience as well as results in the Proceedings of reasonable quality. We appreciate that the students may prefer to disseminate their outstanding research results in more impactful publications.

We are pleased to use this occasion to congratulate the participants of the past Skoltech PhD Energy Seminars who had received Skoltech PhD degree this academic year, Mazhar Ali (Engineering systems), Timur Yagafarov and Anton Baranikov (Physics), Timur Saifutdinov (Engineering systems) and Aleksandra Boldyreva (Sveshnikova, Materials Science and Engineering).

We appreciate the concerted efforts and devotion of all the Seminar attendees and the contributions of their supervisors, especially important under the restrictions caused by COVID-19 pandemic. We are grateful to the Skoltech Dean of Education Dr. Anna Derevnina for supporting the Seminar initiative. We also thank Ms. Ksenia Sattarova for preparing this Proceedings for publication.

Alexei Buchachenko (Seminar instructor)
Anna Sharova
Elizaveta Tikhomirova

CONTENTS

RESEARCH ARTICLES

FOCUS

Research articles

Revealing Impact of Spiro-based Derivatives Structure on Perovskite Stability

Marina M. Tepliakova

Abstract

Perovskite solar cells is a rapidly developing photovoltaic technology, which has achieved high power conversion efficiencies but still doesn't provide long-term operational stability. Recently it was shown, that the hole-transport material can affect the stability of perovskites that is why plenty of works focus on developing various new p-type molecules for this purpose. The spiro-based derivatives are widely used as hole-transport materials in perovskite solar cells. Herein we report the influence of the structure of spiro-based molecules on the photostability of thin perovskite films. We demonstrate that the stability of perovskite films covered by spiro-based derivatives improves with increasing the number of redox-sites in the structure of the material. In particular, Spiro-OMeTAD, which contains twelve redox-active sites, remains stable for more than 250h under illumination in inert atmosphere, while spiro-derivatives with four and zero redox-active sites undergo severe absorption loss at 750 nm up to 100% after 250h of light soaking, which is equal to complete decomposition of the photoactive material. Perusal of our results suggests that additional redox-sites in the structure enhance the stability of perovskite solar cells.

Our results reveal some basic principles for the future ra-tional design of hole transport materials for perovskite solar cells with enhanced stability.

Index Terms

Hole Transport Materials; Perovskite Solar Cells; Perovskite Stability; Spiro-OMeTAD

I. NOMENCLATURE AND ABBREVIATIONS

VOC	open-circuit voltage (mV)
PCE	power conversion efficiency (%)
HOMO	highest occupied molecular orbital (eV)
XRD	X-ray diffraction
UV-Vis	ultraviolet-visible (spectroscopy)
AM 1.5G	Air mass 1.5 global standard

Center for Energy Science and Technology, Skolkovo Institute of Science and Technology, Skolkovo Innovation Center, Building 3, Moscow, 121205, Russia. **marina.tepliakova@skoltech.ru**

II. INTRODUCTION

PEROVSKITE solar cells is an emerging technology, which developed from the first report of 3.8% [1] to 25.2% [2] light to energy conversion efficiency and continues to rise. Perovskite solar cell structure includes photoactive material with perovskite structure, sandwiched between charge transport layers: n-type and p-type materials that selectively extract electrons and holes, respectively, and transfer the charges to the electrodes. In classical n-i-p configuration, the highly transparent electron-transport layer (ETL) is placed between the transparent electron-collecting electrode and perovskite. ETLs are usually presented by inorganic metal oxides with high transparency, such as TiO_2, SnO_2, ZnO, etc.

The hole transport material (HTM) in n-i-p configuration is situated on the top of the perovskite and transfers holes to the metal hole-collecting electrode. The basic requirements applied to HTM can be summarized into the following list: (a) the highest occupied energy level of the material should match the valence band of the perovskite for effective hole extraction; (b) the lowest occupied energy level of the HTM should stay much higher than the conduction band of the perovskite for effective electron blocking; (c) the glass transition temperature of the HTM should be higher than the device operational temperature to avoid the crystallization of the material; (d) the hole mobility should be higher than 10^{-3} $cm^2V^{-1}s^{-1}$ for fast charge transport [3], [4]. It should be noted, that most of the requirements are related to the physical properties of the material. However, to the best of our knowledge, in modern literature there are no studies of relations between the HTM chemical structure and its performance in perovskite.

State-of-the-art HTMs are organic materials and the most studied of them is a small molecule 2,2′,7,7′-tetrakis-(N,N-di-p-methoxyphenyl-amine)-9,9′-spirobiuorene (Spiro-OMeTAD) (Fig. 1). Perovskite solar cells with Spiro-OMeTAD achieve efficiencies of 20% [5]. However, the hole mobility in this material is equal to $\mu_h=10^{-5}$ $cm^2V^{-1}s^{-1}$, which is insufficient for effective charge transport [6]. That is why the application of Spiro-OMeTAD as HTM is usually accompanied with additional p-doping by different substances [5], [7]-[9], the most effective of which is a combination of Lithium bis(trifluoromethylsulfonyl)imide (LiTFSI) with tert-butylpyridine (tBP), followed by the oxidation in the air [10], [11]. However, the hygroscopic nature of these salts leads to decreasing of the operational stability. What is more, under working conditions the severe morphological deformations in the hole-transport layer (HTL) can occur, leading to deterioration of the overall performance of the devices [12].

Another important issue of perovskite solar cells containing Spiro-OMeTAD is the huge cost of this HTM. Furthermore, the need to use additional doping leads to a greater increase of the cost of devices. In this regard, a search for Spiro-OMeTAD analogs is being carried out, which will make it possible to obtain high-performance perovskite photovoltaics without doping.

All modifications applied to the Spiro-OMeTAD structure reported in the literature can be divided into three categories: modification of substituents [13]-[15], modification of core [16]-[20] and modification of both substituents and core [21]-[27] (Fig. 2).

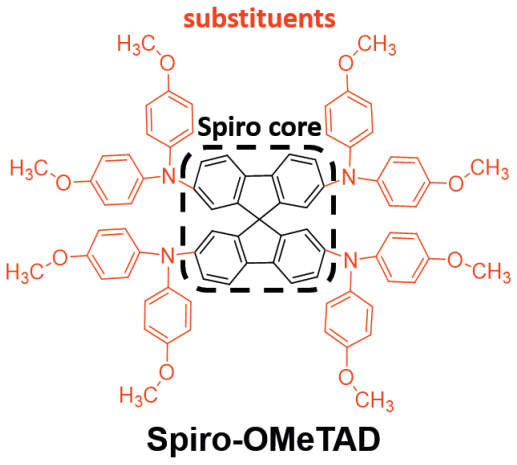

Fig. 1. Structure of Spiro-OMeTAD with the highlighted spiro-core (black) and substituents (red)

One of the popular modifications of Spiro-OMeTAD is modification of the methoxydiphenylamino substituents. In [13] two derivatives 2,4-Spiro-OMeTAD and 3,4-Spiro-OMeTAD with methoxy substituents in positions of 2,4 and 3,4 were synthesized and characterized (Fig. 2). According to photoluminescence spectroscopy, the derivative with additional methoxy group in ortho-position provides more efficient hole injection compared to 3,4-Spiro-OMeTAD and conventional Spiro-OMeTAD. What is more, devices with HTM based on 2,4-Spiro-OMeTAD demonstrated superior performance of 17.2% compared to devices with the Spiro-OMeTAD-based HTM with efficiencies of 15.0%. Besides, introducing substituents into meta-position led to decreasing of the HOMO energy level of the molecule to -5.45 eV, thus deteriorating the device performance (PCE=9.1%) mostly impacted by low open-circuit voltage (VOC = 0.75 V). The decrease in VOC evidences the mismatching of the HOMO energy level of 3,4-Spiro-OMeTAD HTM and the perovskite valence band.

Another approach for the modification of substituents is presented in [14], where the 3,4-ethylenedioxythiophene unit was introduced between the spiro-core and the diphenylamino substituents. The target Spiro-tBuBED (Fig. 2) demonstrated excellent performance with impressive VOC=1.1V and the efficiency of 18.6% without additional oxidation in the air, whereas devices using Spiro-OMeTAD as HTM required oxidation with the oxygen of the air for 1h and achieved lower efficiency of 17.4%. What is more, the authors estimated the cost of 1mmol of both HTMs. The synthesis of Spiro-tBuBED was more economical compared to the Spiro-O-MeTAD due to the use of direct heteroarylation instead of the classic polycondensation reaction.

In [15] Spiro-derivatives with different alkyl substituents were compared. To affect the molecular packing with different alkyl substituents, new spiro-derivatives with the different length of the alkoxy chain as Spiro-OEtTAD, Spiro-OPrTAD, Spiro-OiPrTAD, and Spiro-OBuTAD were studied (Fig. 2). The glass transition temperature of new derivatives exceeded that of Spiro-OMeTAD (Tg=167 °C). The high Tg is a crucial requirement for a HTM that allows avoiding undesirable re-crystallization of the layer under operational conditions. The performance acquired from cells with spiro-derivatives was comparable. However, among all the derivatives Spiro-OEtTAD showed slightly superior performance with the efficiency

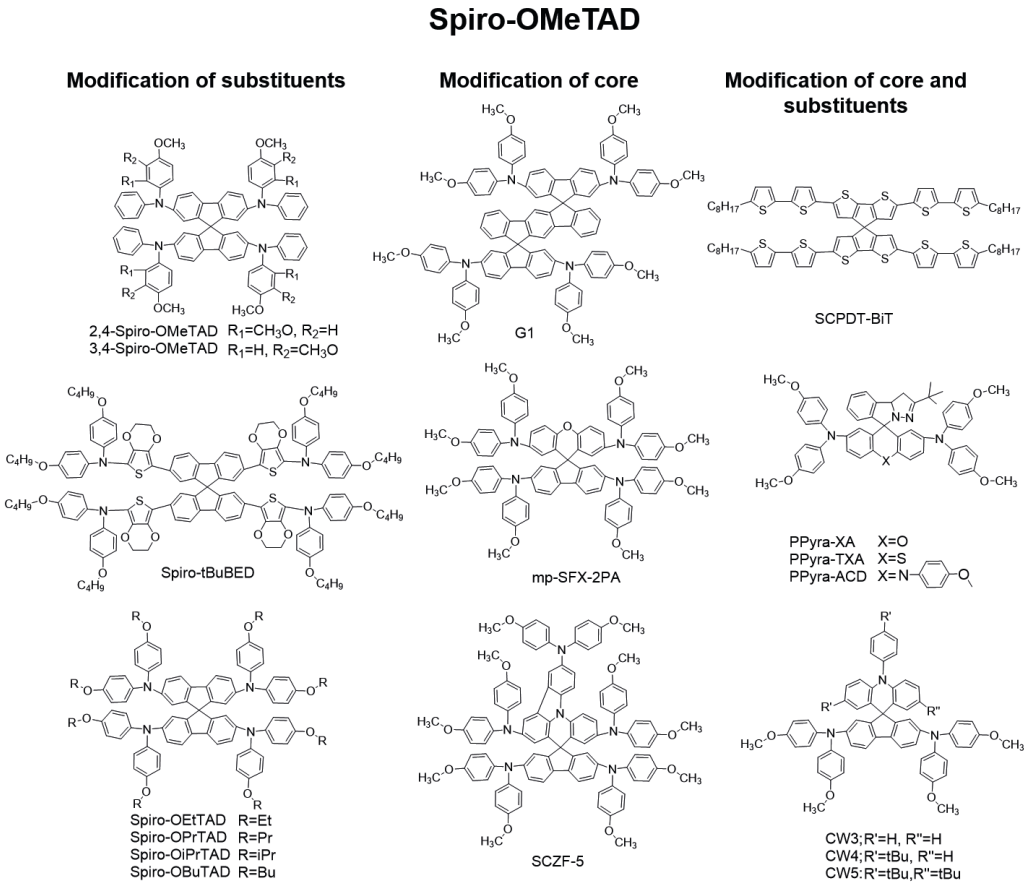

Fig. 2. Examples of possible modification of the Spiro-OMeTAD structure from the literature [13]-[27]

of 20.2%. Besides, the stability of unencapsulated devices in the ambient air and humidity of 30% was investigated. Surprisingly, the materials with butoxy and isopropoxy substituents demonstrated an efficiency loss of 15%, whereas ethoxy and methoxy substituted spiro-derivatives degraded up to 75% and 53% of initial efficiency respectively after 21 days of degradation.

In modern literature, various modifications of the structure are described. However, we believe that the thorough study of the correlation between the structure of the HTM and the stability of the perovskite material will lead to a more rational approach to further research in this area.

Herein we investigate four spiro-based molecules: conventional Spiro-OMeTAD, Spiro-derivative with four diphenylamino substituents (Spiro-TAD), unsymmetrical spiro-based molecule with two diphenylamino and two bisphenyl substituents (Spiro-DPSP) and a derivative with four bisphenyl substituents (Spiro-sexiphenyl). We systematically investigated the photostability of thin films with configuration glass/perovskite/HTM, where HTM is one of the abovementioned spiro-derivatives and Spiro-OMeTAD. Thin films were placed into the degradation chamber under inert atmosphere and constant illumination of 0.7 Suns. Using a set of complementary techniques, we were able to identify the influence of the structure of HTM on the stability of absorber material.

III. RESULTS AND DISCUSSION

In this work, we used a specially designed degradation chamber integrated inside MBraun glovebox with a metal-halide light source giving a spectrum close to AM1.5G. In this chamber, stable light power (70±3 mW/cm^2) and temperature (55±1 °C) conditions are realized by using a fan cooling system. We intentionally kept the temperature over 50 °C to speed up the degradation process of the perovskite absorber $CH_3NH_3PbI_3$ ($MAPbI_3$) and, therefore, to speed up the experiment. More details about the used setup can be found in the previous publications [28], [29].

The overall layout of the performed experiments is shown in Fig. 3. At the first stage, thin films with configuration glass/perovskite/HTM were prepared. As a perovskite material, conventional $MAPbI_3$ absorber was used. As for HTM, three spiro-derivatives and Spiro-OMeTAD were compared in this experiment. Structures of these four molecules are presented in Fig. 4a. Further, samples were placed into the degradation chamber under inert atmosphere of N_2 and constant illumination with an average light power of 0.7±0.03 Suns. It should be noted, that 1 Sun is equal to 1.5AM global standard.

In Fig. 4b the evolution of absorption spectra for all the systems is presented. According to UV-Vis spectroscopy analysis, the photobleaching effect was observed for systems with Spiro-TAD, Spiro-DPSP, and Spiro-sexiphenyl. Thus, in these cases the perovskite layer was not photostable. However, perovskite layer covered with Spiro-OMeTAD remains stable after 250h under constant light illumination. In the case of the UV-Vis spectroscopy, more attention should be paid to the evolution of absorption intensity in the ranges from 300 to 400 and 700 to 750 nm, because in these ranges the main contribution to

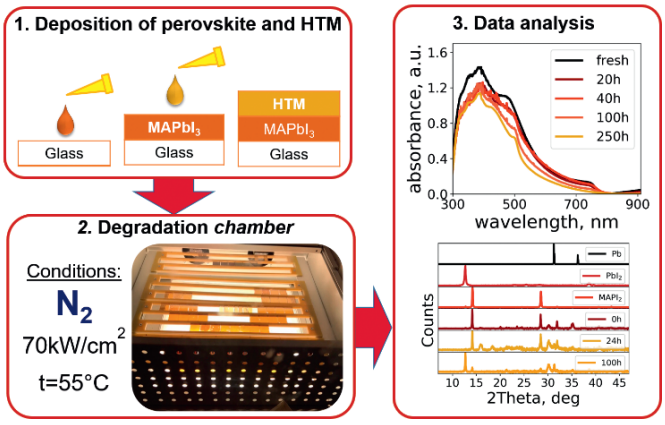

Fig. 3. Principal schematic description of the performed experiment

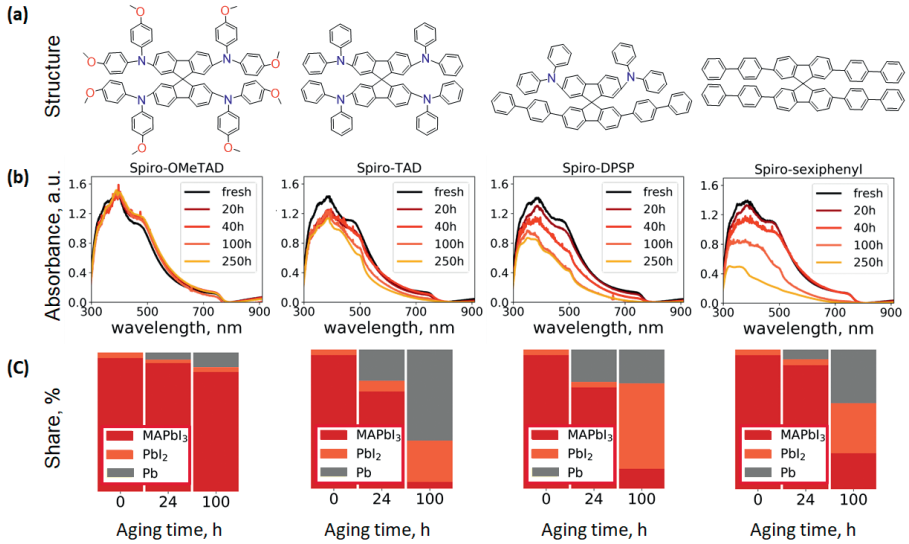

Fig. 4. Structures of four spiro-based derivatives (a), evolution of absorption spectra for devices with configuration glass/perovskite/HTM (b), XRD patterns (c)

the absorption is made by the perovskite material [30]. At the same time, in other parts of the spectrum, the total absorbance can be influenced by the absorbance of perovskite decomposition products. Taking this assumption into consideration, we can compare the speed of perovskite decomposition covered by different spiro-derivatives. Hence, samples with Spiro-OMeTAD coverage are the most stable. Intermediate stability is demonstrated by samples with Spiro-TAD derivative. Finally, the fastest decomposition of perovskite layer was observed for samples with Spiro-DPSP and Spiro-sexiphenyl. This dependence stays in correlation with the number of redox-active sites in the structure of the HTM. In the case of Spiro-OMeTAD, which contains four tertiary amine moieties and eight oxygen amine substituents, the perovskite layer degrades slower compared to Spiro-TAD. As for Spiro-DPSP and Spiro-sexiphenyl derivatives with two and zero heteroatoms in the structure, the perovskite material is almost completely decomposed, as we see no absorbance in the range of 700-750nm on the UV-Vis spectra after 100 hours from methoxy substituents, the absorber layer remains stable.

The XRD patterns of the studied systems were collected for fresh samples and after 24h and 100h of continuous light soaking. Recently it was reported that under light and heat the perovskite material undergoes reversible decomposition into solid (Pb, PbI_2) and gaseous (I_2, CH_3NH_2 etc.) substances [29], [31], [32]. Therefore, the XRD is a powerful tool that provides information about the appearance of solid decomposition products (Pb, 2Θ=31.3; PbI_2, 2Θ=12.7), which in turn evidences the occurrence of irreversible degradation processes of the perovskite ($MAPbI_3$, peak at 2Θ=14.2 was considered as the most intensive signal). In Fig. 4c the ratio between perovskite peak intensity and intensity of the decomposition products PbI_2 and Pb is presented. This estimation might not be fully accurate with respect to the real quantitative composition of the samples since it does not account for the amorphous phase. That is the reason for insignificant discrepancy between the evolution of stability observed from UV-Vis and the evolution observed from XRD patterns. For such experiments, UV-Vis should be considered as a more trustworthy source of information on the perovskite composition. Following Fig. 4c, the samples with the Spiro-OMeTAD coverage undergo insignificant decomposition after 100h of light soaking, whereas for other cases substantial decomposition of the absorber layer can be observed after 100h.

Finally, it was shown that the use of materials with a large number of redox-active centers leads to enhancement of the stability of the photoactive layer. To explain this phenomenon, the chemical processes occurring at the boundary between the photoactive layer and HTM should be considered. The redox-active sites in the structure of the HTM can interact with the perovskite layer, forming Lewis adducts and passivating the defects on the grain boundaries of the perovskite layer [33]. Therefore, we speculate the formation of the firmly connected interlayer between perovskite and redox-active sites of the HTM. Such protective layer prevents the migration of gaseous perovskite decomposition products from the structure. What is more, fixation of the HTM molecules on the surface of the photoactive layer results in mitigation of the HTM light-induced crystallization. Both these factors result in decreasing the number of paths for migration of the decomposition products from the structure.

IV. CONCLUSIONS

In conclusion, we systematically explored the photochemical stability of the conventional perovskite material covered with one of four spiro-derivatives: Spiro-OMeTAD, Spiro-TAD, Spiro-DPSP, and Spiro-sexiphenyl, that contain 12, 4, 2 and 0 redox-active sites respectively. The decomposition of photoactive material was controlled by collecting the UV-Vis absorption spectra and XRD patterns. It was observed that under inert atmosphere and constant illumination samples covered with Spiro-OMeTAD remain stable up to 250h. Significant degradation of the absorber material was observed for samples with Spiro-TAD coverage, which lose 80% of the initial absorbance at 750 nm after 250h. Even more severe degradation under constant illumination was observed for Spiro-DPSP and Spiro-sexiphenyl: perovskite covered with these materials completely decomposed after 250h. We strongly believe that this phenomenon is related to the formation of a firmly bonded interlayer between perovskite and redox-active units of hole transport material. This protective interlayer prevents perovskite irreversible decomposition and mitigates the hole transport material light-induced crystallization. These factors result in the enhancement of the stability of perovskite layer.

The obtained collection of data evidences that hole transport material with redox-active sites in the structure can mitigate decomposition processes of the perovskite layer. Our results pave a way for the rational design of perspective HTMs for stable perovskite photovoltaics.

V. APPENDIX: EXPERIMENTAL

All chemicals were purchased from Sigma-Aldrich, Acros or Ossila and applied without further purification.

A. Sample preparation

Glass substrates were cleaned by sonication in deionized water, acetone and isopropyl alcohol, dried in air, and placed under plasma (50W, 5 min). 0.5M $MAPbI_3$ solution was prepared by mixing PbI_2 and CH_3NH_3I powders in stoichiometric amounts and dissolving them in DMF. Filtered solution was deposited in glovebox at 4000 rpm followed by quenching with toluene antisolvent after 5 sec. $MAPbI_3$ films were slowly heated up to 80 °C and further annealed for 5 min.

Solutions of Spiro-based HTMs 10mg/ml in chlorobenzene filtered through PTFE were spin-coated on the top of the perovskite at 3000 rpm.

B. Film characterization

X-ray diffraction patterns from the films were measured using Bruker D8 diffractometer with a Cu Ka source. A fixed illumination mode in the range of 5–60 2Θ degrees was used.

UV-vis spectra were measured in an inert atmosphere using AvaSpec-2048-2UV-VIS spectrometer integrated with MBraun glovebox.

VI. ACKNOWLEDGMENT

The author gratefully acknowledges the contributions of P. A. Troshin for supervising, L. M. Tepliakov and E. V. Tikhomirova for their support on the original version of this document.

VII. REFERENCES

[1] A. Kojima, K. Teshima, Y. Shirai, and T. Miyasaka, "Organometal Halide Perovskites as Visible-Light Sensitizers for Photovoltaic Cells," JACS, vol. 131, pp. 6050–6051, 2009.

[2] NREL (18 march). Best certified Research-Cell Efficiency Chart. Available: https://www.nrel.gov/pv/cell-efficiency.html

[3] W. Zhou, Z. Wen, and P. Gao, "Less is More: Dopant-Free Hole Transporting Materials for High-Efficiency Perovskite Solar Cells," Adv. Energy Mater., vol. 8, p. 1702512, 2018.

[4] S. Gangala and R. Misra, "Spiro-linked organic small molecules as hole-transport materials for perovskite solar cells," J. Mater. Chem. A, vol. 6, pp. 18750–18765, 2018.

[5] X. Wang, J. Wu, Y. Yang, X. Liu, Q. Guo, Z. Song, G. Li, Z. Lan, and M. Huang, "High performance and stable perovskite solar cells using vanadic oxide as a dopant for spiro-OMeTAD," J. Mater. Chem. A, vol. 7, pp. 13256–13264, 2019.

[6] D. P. Tabor, V. A. Chiykowski, P. Friederich, Y. Cao, D. J. Dvorak, C. P. Berlinguette, and A. Aspuru-Guzik, "Design rules for high mobility xanthene-based hole transport materials," Chem. Sci., vol. 10, pp. 8360–8366, 2019.

[7] J. Seo, N. J. Jeon, W. S. Yang, H.-W. Shin, T. K. Ahn, J. Lee, J. H. Noh, and S. I. Seok, "Effective Electron Blocking of CuPC-Doped Spiro-OMeTAD for Highly Efficient Inorganic–Organic Hybrid Perovskite Solar Cells," Adv. Energy Mater., vol. 5, p. 1501320, 2015.

[8] X. Gu, Y. Li, Y. Mu, M. Zhang, T. Lu, and P. Wang, "$FeCl_3$ as a low-cost and efficient p-type dopant of Spiro-OMeTAD for high performance perovskite solar cells," RSC Adv., vol. 8, pp. 9409–9413, 2018.

[9] Q. Wang, "Influence of a cobalt additive in spiro-OMeTAD on charge recombination and carrier density in perovskite solar cells investigated using impedance spectroscopy," Phys. Chem. Chem. Phys., vol. 20, pp. 10114–10120, 2018.

[10] S. Wang, Z. Huang, X. Wang, Y. Li, M. Günther, S. Valenzuela, P. Parikh, A. Cabreros, W. Xiong, and Y. S. Meng, "Unveiling the Role of tBP–LiTFSI Complexes in Perovskite Solar Cells," JACS, vol. 140, pp. 16720–16730, 2018.

[11] S. Wang, W. Yuan, and Y. S. Meng, "Spectrum-Dependent Spiro-OMeTAD Oxidization Mechanism in Perovskite Solar Cells," ACS App. Mater. Interf., vol. 7, pp. 24791–24798, 2015.

[12] A. K. Jena, M. Ikegami, and T. Miyasaka, "Severe Morphological Deformation of Spiro-OMeTAD in (CH3NH3)PbI3 Solar Cells at High Temperature," ACS Energy Lett., vol. 2, pp. 1760–1761, 2017.

[13] M.-D. Zhang, D.-X. Zhao, L. Chen, N. Pan, C.-Y. Huang, H. Cao, and M.-D. Chen, "Structure-performance relationship on the asymmetric methoxy substituents of spiro-OMeTAD for perovskite solar cells," Sol. Energy Mater. Sol. Cells, vol. 176, pp. 318–323, 2018.

[14] P.-H. Lin, K.-M. Lee, C.-C. Ting, and C.-Y. Liu, "Spiro-tBuBED: a new derivative of a spirobifluorene-based hole-transporting material for efficient perovskite solar cells," J. Mater. Chem. A, vol. 7, pp. 5934–5937, 2019.

[15] F. Liu, S. Bi, X. Wang, X. Leng, M. Han, B. Xue, Q. Li, H. Zhou, and Z. Li, "Similar or different: the same Spiro-core but different alkyl chains with apparently improved device performance of perovskite solar cells," Sci. China Chem., vol. 62, pp. 739–745, 2019.

[16] K. Gao, B. Xu, C. Hong, X. Shi, H. Liu, X. Li, L. Xie, and A. K. Y. Jen, "Di-Spiro-Based Hole-Transporting Materials for Highly Efficient Perovskite Solar Cells," Adv. Energy Mater., vol. 8, p. 1800809, 2018.

[17] X.-D. Zhu, X.-J. Ma, Y.-K. Wang, Y. Li, C.-H. Gao, Z.-K. Wang, Z.-Q. Jiang, and L.-S. Liao, "Hole-Transporting Materials Incorporating Carbazole into Spiro-Core for Highly Efficient Perovskite Solar Cells," Adv. Func. Mater., vol. 29, p. 1807094, 2019.

[18] K. Liu, Y. Yao, J. Wang, L. Zhu, M. Sun, B. Ren, L. Xie, Y. Luo, Q. Meng, and X. Zhan, "Spiro[fluorene-9,9'-xanthene]-based hole transporting materials for efficient perovskite solar cells with enhanced stability," Mater. Chem. Front., vol. 1, pp. 100–110, 2017.

[19] Y.-K. Wang, Z.-C. Yuan, G.-Z. Shi, Y.-X. Li, Q. Li, F. Hui, B.-Q. Sun, Z.-Q. Jiang, and L.-S. Liao, "Dopant-Free Spiro-Triphenylamine/Fluorene as Hole-Transporting Material for Perovskite Solar Cells with Enhanced Efficiency and Stability," Adv. Func. Mater., vol. 26, pp. 1375–1381, 2016.

[20] P. Ganesan, K. Fu, P. Gao, I. Raabe, K. Schenk, R. Scopelliti, J. Luo, L. H. Wong, M. Grätzel, and M. K. Nazeeruddin, "A simple spiro-type hole transporting material for efficient perovskite solar cells," Energy Environ. Sci., vol. 8, pp. 1986–1991, 2015.

[21] T.-S. Su, H.-Y. Tsai, K. Kannankutty, C.-T. Chen, Y. Chi, and T.-C. Wei, "New Spiro-Phenylpyrazole/Dibenzosuberene Derivatives as Hole-Transporting Material for Perovskite Solar Cells," Solar RRL, vol. 3, p. 1900143, 2019.

[22] R. Nakar, F. J. Ramos, C. Dalinot, P. S. Marques, C. Cabanetos, P. Leriche, L. Sanguinet, M. Kobeissi, P. Blanchard, J. Faure-Vincent, F. Tran-Van, N. Berton, J. Rousset, and B. Schmaltz, "Cyclopentadithiophene and Fluorene Spiro-Core-Based Hole-Transporting Materials for Perovskite Solar Cells," J. Phys. Chem. C, vol. 123, pp. 22767–22774, 2019.

[23] G. Wu, Y. Zhang, R. Kaneko, Y. Kojima, K. Sugawa, T. H. Chowdhury, A. Islam, Q. Shen, M. Akhtaruzzaman, T. Noda, and J. Otsuki, "Hole-Transport Materials Containing Triphenylamine Donors with a Spiro[fluorene-9,9'-xanthene] Core for Efficient and Stable Large Area Perovskite Solar Cells," Solar RRL, vol. 1, p. 1700096, 2017.

[24] K. Guo, M. Wu, S. Yang, Z. Wang, J. Li, X. Liang, F. Zhang, Z. Liu, and Z. Wang, "Introduction of Fluorine Into spiro[fluorene-9,9'-xanthene]-Based Hole Transport Material to Obtain Sensitive-Dopant-Free, High Efficient and Stable Perovskite Solar Cells," Solar RRL, vol. 3, p. 1800352, 2019.

[25] V. Govindan, K.-C. Yang, Y.-S. Fu, and C.-G. Wu, "Low-cost synthesis of heterocyclic spiro-type hole transporting materials for perovskite solar cell applications," New J. Chem., vol. 42, pp. 7332–7339, 2018.

[26] S. Ma, H. Zhang, N. Zhao, Y. Cheng, M. Wang, Y. Shen, and G. Tu, "Spiro-thiophene derivatives as hole-transport materials for perovskite solar cells," J. Mater. Chem. A, vol. 3, pp. 12139–12144, 2015.

[27] M.-H. Li, C.-W. Hsu, P.-S. Shen, H.-M. Cheng, Y. Chi, P. Chen, and T.-F. Guo, "Novel spiro-based hole transporting materials for efficient perovskite solar cells," Chem. Commun., vol. 51, pp. 15518–15521, 2015.

[28] A. F. Akbulatov, L. A. Frolova, M. P. Griffin, I. R. Gearba, A. Dolocan, D. A. Vanden Bout, S. Tsarev, E. A. Katz, A. F. Shestakov, K. J. Stevenson, and P. A. Troshin, "Effect of Electron-Transport Material on Light-Induced Degradation of Inverted Planar Junction Perovskite Solar Cells," Adv. Energy Mater., vol. 7, p. 1700476, 2017.

[29] A. F. Akbulatov, S. Y. Luchkin, L. A. Frolova, N. N. Dremova, K. L. Gerasimov, I. S. Zhidkov, D. V. Anokhin, E. Z. Kurmaev, K. J. Stevenson, and P. A. Troshin, "Probing the Intrinsic Thermal and Photochemical Stability of Hybrid and Inorganic Lead Halide Perovskites," J. Phys. Chem. Lett., vol. 8, pp. 1211–1218, 2017.

[30] E. Belarbi, M. Vallés-Pelarda, B. Clasen Hames, R. S. Sanchez, E. M. Barea, H. Maghraoui-Meherzi, and I. Mora-Seró, "Transformation of PbI_2, $PbBr_2$ and $PbCl_2$ salts into $MAPbBr_3$ perovskite by halide exchange as an effective method for recombination reduction," Phys. Chem. Chem. Phys., vol. 19, pp. 10913–10921, 2017.

[31] E. J. Juarez-Perez, Z. Hawash, S. R. Raga, L. K. Ono, and Y. Qi, "Thermal degradation of $CH_3NH_3PbI_3$ perovskite into NH_3 and CH_3I gases observed by coupled thermogravimetry–mass spectrometry analysis," Energy Environ. Sci., vol. 9, pp. 3406–3410, 2016.

[32] D. Bryant, N. Aristidou, S. Pont, I. Sanchez-Molina, T. Chotchunangatchaval, S. Wheeler, J. R. Durrant, and S. A. Haque, "Light and oxygen induced degradation limits the operational stability of methylammonium lead triiodide perovskite solar cells," Energy Environ. Sci., vol. 9, pp. 1655–1660, 2016.

[33] C. Sun, Z. Wu, H.-L. Yip, H. Zhang, X.-F. Jiang, Q. Xue, Z. Hu, Z. Hu, Y. Shen, M. Wang, F. Huang, and Y. Cao, "Amino-Functionalized Conjugated Polymer as an Efficient Electron Transport Layer for High-Performance Planar-Heterojunction Perovskite Solar Cells," Adv. Energy Mater., vol. 6, p. 1501534, 2016.

Thiourea Assisted Enhanced Thermal Stability of $MAPbI_3$ Thin Films

Mayuribala Mangrulkar

Abstract **In recent years perovskite photovoltaics has made great developments. Yet, it is critical to achieve highly crystalline, stable and efficient perovskite thin films and solar cells. This study demonstrates that the addition of thiourea in methylammonium lead iodide precursor solution generates highly crystalline thin films and enhances the respective thermal controlled stability of perovskite thin films over pristine perovskite. To investigate thermal controlled stability, UV-Vis/absorbance and XRD measurements were employed.**

Index Terms **Perovskite; Additive; Methylammonium Lead Triiodide; Stability; Thiourea**

I. NOMENCLATURE

$MAPbI_3$	Methylammonium lead iodide
V_{oc}	Open circuit voltage
J_{sc}	Short circuit current density
PCE	Power conversion efficiency
MAI	Methylammonium Iodide
PCBA	Phenyl-C_{61}-butyric acid
PTA	Polytriarylamine
ITO	Indium tin oxide
UV-Vis	Ultraviolet-visible spectroscopy
XRD	X-ray Diffraction
FWHM	Full width at half maximum

Center for Energy Science and Technology, Skolkovo Institute of Science and Technology, Skolkovo Innovation Center, Building 3, Moscow, 121205, Russia. **Mayuribala.Mangrulkar@skoltech.ru**

II. INTRODUCTION

$CH_3NH_3PbI_3$ ($MAPbI_3$) is a perovskite material. It has become a point of interest for researchers in the last decade since the perovskite solar cell power conversion efficiencies were increased up to 25.2%. This is because the high absorbance coefficient, higher charge carrier mobility, and long carrier diffusion lengths of perovskite materials are comparable to silicon photovoltaics. In addition, it has low processing costs; this makes $MAPbI_3$ a potential candidate to replace existing silicon-based photovoltaic technology [1], [2]. Yet, perovskite solar cells are far from commercialization. The main reason behind it is poor intrinsic thermal and photo stability. Because of low thermal intrinsic stability, $MAPbI_3$ tends to completely degrade with temperature higher than 85 °C even in inert conditions. $MAPbI_3$ changes its phase from cubic to tetragonal phase at 57 °C. This causes strain and defects in $MAPbI_3$ lattice structure, thus making it intrinsically unstable at elevated temperatures [3].

To resolve this issue, additive engineering is often performed by researchers. Usage of an additive may deplete trap state, enlarge grain size, produce good crystalline perovskite film resulting in photo-stable thin film and highly efficient perovskite solar cell device [4]. In this study, we implemented the addition of thiourea into $MAPbI_3$ perovskite precursor solution. Reports have suggested that thiourea has high melting and boiling points, i.e. 182 and 263.89 °C, respectively [5], [6]. Further, thiourea can act as a Lewis base. Thiourea consists of two amino groups and one S-donor group. These amino groups can form hydrogen bonds with iodine atoms in perovskite crystals and S-donors can form Lewis acid-base adducts with lead atoms or hydrogen bonds with amino groups in perovskite crystal [7]-[9]. Thus, it can promote grain growth and produce good quality crystalline films, which can make absorber layer photo-stable [8], [9]. In this study we investigate the intrinsic stability of $MAPbI_3$ with thiourea in a thermally controlled environment. To examine the impact of thiourea in $MAPbI_3$ thin films thermally controlled UV-Vis and XRD measurements were performed. Further, concentration of thiourea was optimized to obtain the best solar cell performance.

III. EXPERIMENTAL METHODS

N,N-dimethylformamide (DMF, anhydrous, 99.99%), N-methyl-2-pyrrolidone (NMP), toluene, were purchased from Sigma-Aldrich and used as received. MAI, PbI_2, PCBA and PTA were homegrown and used as 99.999 % pure.

A. Film Preparation

0.3M $MAPbI_3$ films containing 5% thiourea (by weight) were prepared on glass substrate. Further, to test thermal stability, films were placed on a hotplate at 60 °C in the dark under inert environment (i.e., H_2O <0.1 ppm and O_2< 0.1 ppm) up to 1400 hrs. This allowed us to minimize the possibility of degradation due to moisture, air and other external factors. UV-Vis and XRD measurements were performed on both fresh and thermal controlled thin films with and without thiourea. UV-Vis spectra were measured using AvaSpec-2048-2 UV-Vis fiber spectrometer integrated inside the glove box.

X-ray diffraction patterns were measured using a Bruker D8 Advance powder diffractometer (Cu-Ka radiation, 5-60° 2 theta range, 0.0219° increment step). Measurements were carried out in fixed illumination mode with no sample rotation. The time interval of 0.2 seconds, voltage 40 kV, filament current 40 mA were used for all the measurements.

B. Device Preparation

1.4M of $MAPbI_3$ solution in DMF and NMP (4:1) was used to prepare solar cell devices. Solar cells were prepared in n-i-p configuration in the following architecture: Glass/ITO/SnO_2/ PCBA/$MAPbI_3$+thiourea/PTA/Polystyrene/MoO_3/Ag. Further, Current-Voltage measurements were performed under solar simulator with AM 1.5G (100 mW/cm^2) illumination inside the glovebox. This instrument was provided by a Newport Verasol AAA class solar simulator. The intensity of the illumination was checked before each measurement using a calibrated silicon diode with known spectral response. The J-V curves of all devices were measured while applying a metal mask with 0.041 cm^2 window using Advantest 6240A Source measurement units.

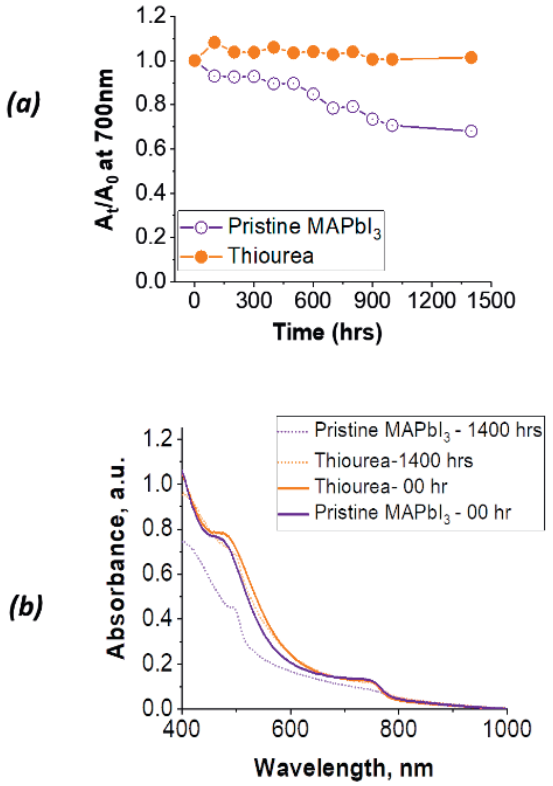

Fig. 1. Optical properties of thermally controlled $MAPbI_3$ thin films with and without thiourea. (a) Evolution of the thermal controlled UV-Vis absorbance of $MAPbI_3$ thin films with and without thiourea. (b) UV-Vis spectra of thermal controlled $MAPbI_3$ thin films with and without thiourea

IV. RESULTS AND DISCUSSION

A. UV-Vis Absorbance measurements

Thin film of $MAPbI_3$ with and without thiourea was spun onto a clean glass substrate. Further UV-Vis and XRD measurements were performed on fresh films. Upon measurements, these films were kept on a hot plate at 60 °C in the dark inside the glovebox. Evolution of UV-Vis spectra over a time span of 1400 hrs is shown in Fig. 1(a). The evolution of UV-Vis spectra presents the normalized values of absorbance. A_t/A_0 represents the normalized value of absorbance at 700 nm, where A_t is the absorbance at time interval t (hours) and A_0 is the absorbance at the fresh stage. As it can be seen, thermal controlled $MAPbI_3$ film with thiourea has normalized absorbance similar to that of fresh film. Hence, it can be said that thiourea containing $MAPbI_3$ film is stable after annealing for 1400 hrs. On the other hand, normalized absorbance of pristine $MAPbI_3$ decays overtime. The normalized absorbance shows that pristine $MAPbI_3$ loses 30% (estimated) of its initial value.

Comparison of UV-Vis absorption spectra of fresh and thermal controlled $MAPbI_3$ films with and without thiourea is shown in Fig. 1(b). It is visible in Fig. 1(b) that absorbance spectra of $MAPbI_3$ film with thiourea is wider than that of pristine $MAPbI_3$. This might be due to scattering caused by increased grain size upon thiourea addition in perovskite [1]. Other than this, the absorption feature at 750 nm, which corresponds to the formation of perovskite, appears in the fresh absorption spectra of pristine and $MAPbI_3$ film with thiourea. However, upon continuous annealing for 1400 hrs, this feature disappeared for pristine $MAPbI_3$ film and another absorption peak appeared near 500 nm. This can be associated with the formation of PbI_2 in pristine film. Whereas, the absorption feature at 750 nm remained the same for $MAPbI_3$ film with thiourea. This suggests that the addition of thiourea in $MAPbI_3$ precursor solution increased the thermal controlled stability of $MAPbI_3$. This matches with reports suggesting that thiourea acts as Lewis base and results in improved crystal quality of perovskite film, as well as reduces elemental iodine to iodine ions. These iodine ions further form an adduct with lead iodide that gets distributed over grain boundary [7], [8]. Thus, the addition of thiourea acts as passivation and increases thermal controlled stability.

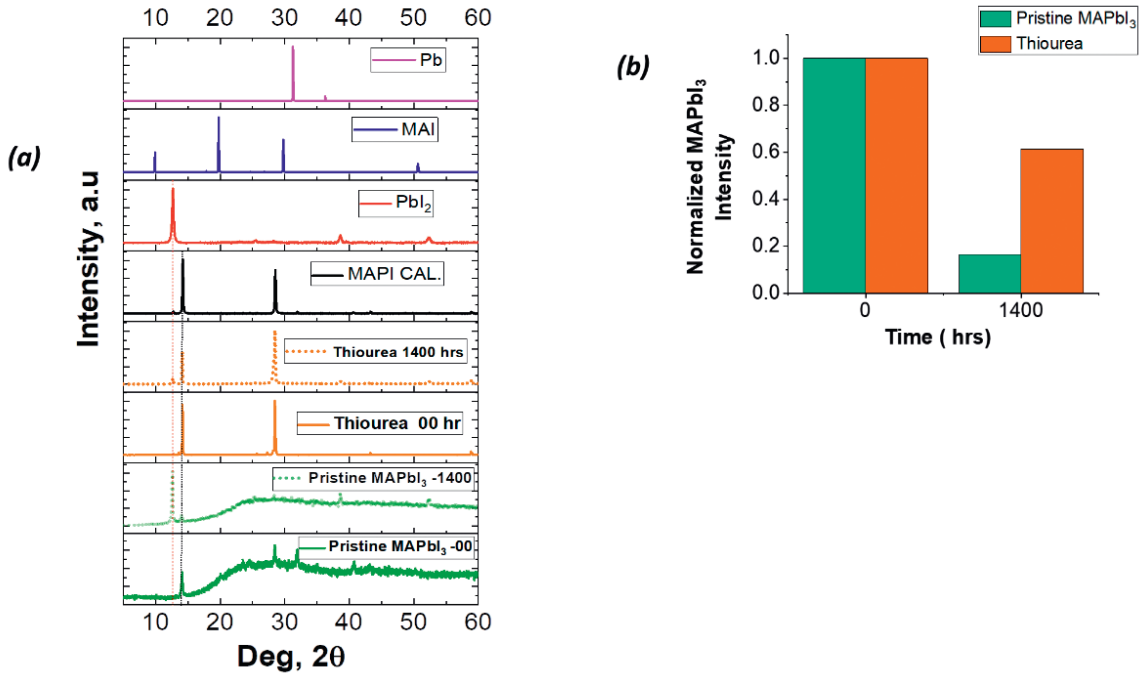

Fig. 2. XRD of thermally controlled $MAPbI_3$ thin film with and without thiourea. (a) XRD of fresh and thermal controlled (after1400 hrs) $MAPbI_3$ thin films with and without thiourea. (b) Comparison of normalized $MAPbI_3$ intensity of thermal controlled thin films with and without thiourea

B. XRD measurements

XRD patterns of fresh and thermal controlled films of pristine $MAPbI_3$ and $MAPbI_3$ with thiourea are shown at a glance in Fig. 2(a). XRD pattern of fresh pristine $MAPbI_3$ film presents peaks at 14.1°, 28.4°, 31.9°, 40.7° and 43.2°. This is consistent with previous reports [7], [8]. It should be noted that XRD of pristine $MAPbI_3$ represents here amorphous peak/pattern. For fresh $MAPbI_3$ films with thiourea peaks associated with $MAPbI_3$ perovskite can be seen at 14.1°, 28.4° and 43.2° as well. However, two additional peaks corresponding to the formation of PbI_2, are found at 12.8° and 25.7°. In addition, the XRD pattern of $MAPbI_3$ with thiourea presents a crystalline peak/pattern. Also, the peak intensity corresponding to $MAPbI_3$ is threefold higher than that of pristine film. This crystalline pattern occurs due to the presence of thiourea in $MAPbI_3$ precursor. Reports suggest that such a crystalline phase represents a perovskite grain size of 400-500 nm [4]. This indicates that the addition of thiourea in $MAPbI_3$ precursor solution increases the crystallinity of $MAPbI_3$ perovskite thin films. To verify crystallinity in our case, FWHM and crystallite size has been calculated from the obtained XRD data. It is known that the increase of diffraction peak intensities and the decrease of FWHM values indicate the good crystallinity of the perovskite film [4], [8]. The relationship between crystallite size and FWHM is given by the Scherer formula [2] as

$$D=0.89\lambda/(\beta.Cos\theta), \quad (1)$$

where D is average crystallite size, λ is the wavelength of X-ray (1.54 A°), θ is diffraction angle and β is FWHM of the peak in XRD pattern, respectively.

XRD analysis at 14.1° showed that FWHM was 0.21 for pristine $MAPbI_3$, which was reduced to 0.08 after the addition of thiourea into the precursor solution. Further, the crystallite size was calculated for all the perovskite peaks and average crystallite size was obtained. Table I compares average crystallite sizes with and without thiourea. It shows that the addition of thiourea increases crystallite size and hence increases crystallinity.

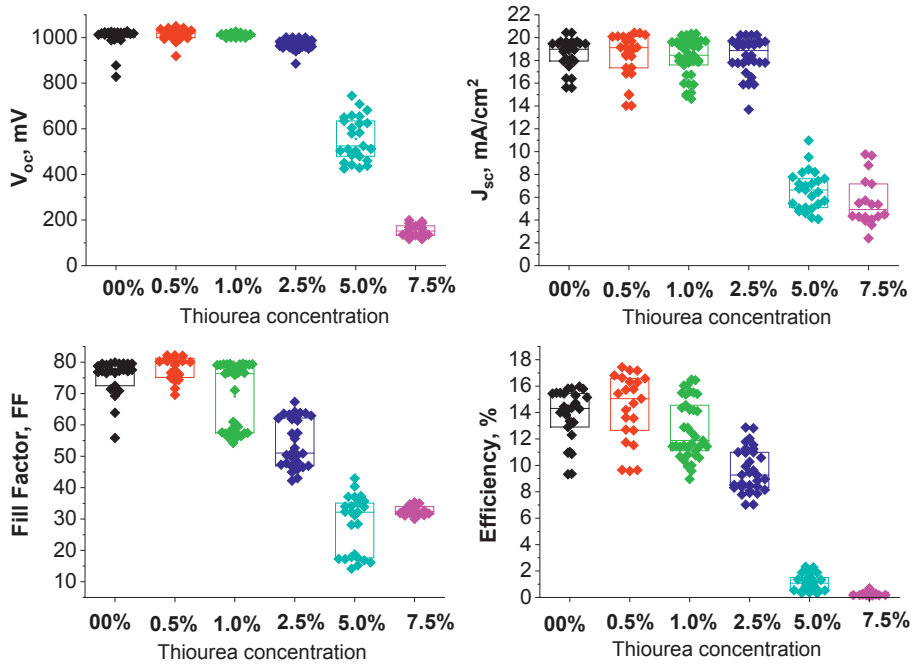

Fig. 3. Solar cell performance of $MAPbI_3$ with and without thiourea

TABLE I

Average crystallite sizes

Perovskite	**Crystallite size (nm)**
Pristine $MAPbI_3$	34.3
$MAPbI_3$ + Thiourea	72.0

Later, upon annealing of films for 1400 hrs, pristine $MAPbI_3$ converts into PbI_2. Whereas $MAPbI_3$ with thiourea maintains its crystalline peak with intense $MAPbI_3$ peaks similar to fresh stage. However, tiny peaks of PbI_2 can also be seen.

Further, the normalized intensities of the $MAPbI_3$ peaks from fresh and thermal controlled pristine and film with thiourea are shown in Fig. 2 (b). It can be seen that upon annealing at 60 °C for 1400 hrs, pristine $MAPbI_3$ remains of less than 20% of its fresh stage. On the other hand, upon the addition of thiourea, $MAPbI_3$ retained 60% of its initial stage. This suggests that the addition of thiourea into $MAPbI_3$ precursor helps to improve thermal controlled stability in thin film.

C. Device Performance

Further, the impact of thiourea addition onto the photovoltaic performance of $MAPbI_3$ solar cells was studied. Solar cells were fabricated in the following configuration: Glass/ITO/SnO_2/PCBA/$MAPbI_3$+thiourea/PTA/Polystyrene/MoO_3/Ag. Concentration of thiourea was varied as 0.5%, 1%, 2.5%, 5% and 7.5% by weight. Solar cell performance with different concentrations of thiourea is shown in Fig. 3. It was found that the addition of 0.5% thiourea (% by weight) resulted in the best device performance. Best devices with 0.5% thiourea exhibit highest open-circuit voltage of 1050 mV, short circuit current density Jsc of 20.42 mA/cm^2, fill factor of 82.19 and PCE of 17.43%. On the other hand, solar cells with pristine $MAPbI_3$ exhibit lower open-circuit voltage 1028.01 mV, similar J_{sc} 20.32 mA/cm^2, the lower fill factor of 79.9 and lower PCE of 15.96%. The best device performance associated with various concentrations of thiourea is presented in Table II.

As can be seen from Fig. 3 and Table II, 0.5% addition of thiourea is the optimum amount to achieve the best solar cell performance. If the concentration of thiourea is increased, V_{oc} started to decline. Though for 1% and 2.5% decent values of V_{oc} are obtained. However, if the concentration is increased by 5% and beyond, V_{oc} decreases drastically. In terms of J_{sc}, a similar pattern is observed. The fill factor exhibits hysteresis from 1% to 5% addition. It should be noted that fill-factor with optimum concentration (0.5%) of thiourea does not show hysteresis. Similarly, PCE decreases as the concentration of thiourea increases.

Reports suggest that the optimum amount of thiourea addition can be correlated with larger grain size and fewer surface defects. The increment in grain size allows to improve charge transport properties [5] and hence improved V_{oc} and power conversion efficiency could be obtained. On the other hand, when the concentration of thiourea goes beyond optimal, the excess of thiourea may block grain boundaries and excess passivation can block carrier transport, thus creating defects in perovskite absorber layer [9]. This can be seen in our case for the concentration of 2.5% and beyond. This is why excess thiourea, in turn, results in lowering of V_{oc}, J_{sc} and ultimately lower solar cell performance

TABLE II

Photovoltaic performance with various concentration of thiourea in $MAPbI_3$ precursor solution

Concentration	**V_{oc}, mV**	**J_{sc}, mA/cm^2**	**Fill Factor, FF**	**PCE, %**
Pristine	1028.	20.32	79.91	15.96
0.5%	1050	20.42	82.19	17.43
1%	1026	20.34	79.52	16.49
2.5%	1001	20.23	67.34	12.87
5%	745	10.97	42.97	2.32
7.5%	200	9.77	35.30	0.69

V. CONCLUSION

In summary, we demonstrated that additive engineering using thiourea in $MAPbI_3$ precursor solution can enhance intrinsic thermal controlled stability of thin film. UV-Vis and XRD measurements confirmed the stability of $MAPbI_3$ films with thiourea upon annealing in the inert environment for 1400 hrs at 60 °C. Also, FWHM and average crystallite size from XRD analysis suggested that thiourea increases the crystallinity of $MAPbI_3$ film, which helps to boost thermal controlled stability. Further, the optimum concentration of thiourea was obtained as 0.5% by weight which resulted in the highest device performance of open-circuit voltage 1050 mV, short circuit current density 20.42 mA/cm^2, fill factor of 82.19 and power conversion efficiency of 17.43%.

VI. REFERENCES

[1] Gao, L., Huang, S., Chen, L., Li, X., Ding, B., Huang, S., and Yang, G., "Excellent Stability of Perovskite Solar Cells by Passivation Engineering," Sol. RRL, vol. 2, no. 8, p. 1800088, Aug. 2018, doi: 10.1002/solr.201800088.

[2] Singh, R. K., Kumar, R., and Singh, J., "Effect of precursors ratio on crystallinity and thermal stability of $CH_3NH_3PbI_3$," AIP Conference Proceedings, May 2017, vol. 1832, doi: 10.1063/1.4980289.

[3] Peng, W., Miao, X., Adinolfi, V., Alarousu, E., El Tall, O., Emwas, A.-H., Zhao, C., Walters, G., Liu, J., Ouellette, O., Pan, J., Murali, B., Sargent, E. H., Mohammed, O. F., and Bakr, O. M., "Engineering of $CH_3NH_3PbI_3$ Perovskite Crystals by Alloying Large Organic Cations for Enhanced Thermal Stability and Transport Properties," Angew. Chemie Int. Ed., vol. 55, no. 36, pp. 10686–10690, Aug. 2016, doi: 10.1002/anie.201604880.

[4] Fei, C., Li, B., Zhang, R., Fu, H., Tian, J., and Cao, G., "Highly Efficient and Stable Perovskite Solar Cells Based on Monolithically Grained $CH_3NH_3PbI_3$ Film," Adv. Energy Mater., vol. 7, no. 9, May 2017, doi: 10.1002/aenm.201602017.

[5] Zhu, L., Xu, Y., Zhang, P., Shi, J., Zhao, Y., Zhang, H., Wu, J., Luo, Y., and Meng, Q., "Investigation on the role of Lewis bases in the ripening process of perovskite films for highly efficient perovskite solar cells," J. Mater. Chem. A Mater. Energy Sustain., vol. 5, pp. 20874-20881, Sep 2017, doi: 10.1039/C7TA05378A.

[6] "62-56-6(Thiourea)-Product-Description." https://www.chemicalbook.com/ChemicalProductProperty_US_CB9854008.aspx (accessed May 05, 2020).

[7] Ko, S., Ryu, G., Kim, B., Cha, G., Ri, J., Sonu, G., and Kim, U., "Effects of thiourea on the perovskite crystallization for fully printable solar cells," Sol. Energy Mater. Sol. Cells, vol. 196, pp. 105–110, July 2019, doi: 10.1016/j.solmat.2019.03.045.

[8] Gao, Y., Wu, Y., Liu, Y., Chen, C., Bai, X., Yang, L., Shi, Z., Yu, W. W., Dai, Q., and Zhang, Y., "Dual Functions of Crystallization Control and Defect Passivation Enabled by an Ionic Compensation Strategy for Stable and High-Efficient Perovskite Solar Cells," ACS Appl. Mater. Interfaces, vol. 12, no. 3, pp. 3631–3641, Jan. 2020, doi: 10.1021/acsami.9b19538.

[9] Hsieh, C. M., Liao, Y. S., Lin, Y. R., Chen, C. P., Tsai, C. M., Wei-Guang Diau, E., and Chuang, S. C., "Low-temperature, simple and efficient preparation of perovskite solar cells using Lewis bases urea and thiourea as additives: Stimulating large grain growth and providing a PCE up to 18.8%," RSC Adv., vol. 8, no. 35, pp. 19610–19615, May 2018, doi: 10.1039/c8ra03175d.

Virtual Power Plant Offering Strategy in a Day-Ahead Market: An ADMM-Based Approach

Arman Alahyari

Abstract

To manage the intermittent nature of distributed energy resources (DERs), and providing market participation capability, the concept of virtual power plant (VPP) has been developed in the smart grid context. VPPs aggregate many small-scale DERs in the distribution grid; some of them introduce uncertainty into the VPP optimization. Thus, in this paper, we propose a novel offering strategy method for a VPP consisting of wind power generation along with distributed storage capacity and demand. The introduced model enables us to formulate the offering strategy problem as an information gap decision theory-based optimization. However, the resulting optimization is computationally huge for a VPP waiting near the closing-gate time to submit a better offer. In this regard, we utilize alternating direct method of multipliers approach to decompose the overall proposed offering strategy. The incorporation of alternating direct method of multipliers and information gap decision theory for VPPs offering strategy is a novel approach resulting in reduction of computational time as well as better profit achievement. The theoretical strategy is thoroughly demonstrated and then validated through numerical studies. The result shows the effectiveness of the proposed approach and its viability for real-world applications.

Index Terms

Distributed Energy Resources; Virtual Power Plant; Uncertainty

Center for Energy Science and Technology, Skolkovo Institute of Science and Technology, Skolkovo Innovation Center, Building 3, Moscow, 121205, Russia. **arman.alahyari@skoltech.ru**

I. NOMENCLATURE

DER	Distributed Energy Resource
DR	Demand Response
VPP	Virtual Power Plant
EV	Electric Vehicle
CHP	Combined Heat and Power
DA	Day-ahead
IGDT	Information-Gap Decision Theory
PDF	Probability Density Function
ADMM	Alternating Direction Method of Multipliers
π^{DA}	DA electricity price
p^{DA}	Energy traded in electric market
t	An optimization period
D	Duration of each optimization period
Cost	Cost of VPP
p^{w}	Wind generation
p^{C}	Conventional generation
p^{dis}	Discharging power from EVs
η^{dis}	Efficiency in discharging process
p^{ch}	Charging power of EVs
p^{D}	Demand
p^{D}_{a}	Inflexible demand
p^{D}_{b}	Flexible demand
T	Total optimization period
E_{f}	Final energy of battery
E_{0}	Initial energy of a battery
e^{ch}	Energy needed to charge EV battery
e^{dis}	Energy from discharging EV battery
η_{ch}	Charging efficiency
$\overline{DR}$	Maximum discharging rate
u^{ch}	Binary that prevents simultaneous charging and discharging
$\overline{CR}$	Maximum charging rate
e^{B}	Remaining energy of the i^th battery at time t
E_{min}	Minimum battery energy
E_{max}	Maximum battery energy
e^{day}	Overall consumption of energy in the next day
ξ_{ω}	Robustness value
R^{R}_{ω}	Minimum expected revenue of the VPP
R^{D}_{0}	Revenue calculated from the deterministic model
$\hat{p}^{w}$	Nominal value for wind production
π^{LS}	Price of load shedding
p^{LS}	Load shedding
π^{WS}	Price of wind spillage
p^{WS}_{t}	Wind generation spillage
ω	A scenario

II. INTRODUCTION

As technologies grow fast nowadays, there appears a necessity to support the increased need for energy. More than that, such issues as geographical limitations and global warming prevent the conventional types of energy from being the first choice [1], [2]. In this regard, the new types of energy resources with individual specifications and characteristics are introduced in power system an important category of which includes the distributed energy resources (DERs) [3]-[5].

Even though these new energy resources give many possibilities, they also bring some challenges, primarily in the management facet of power systems [6], [7]. DERs may contain small scale conventional generations, renewable generations, or even demand response (DR) programs. DERs alone cannot participate in the wholesale electricity market because of their small scale, and the operator of the upstream network cannot get sight of many of them.

Thus, to make the dispersed DERs visible in the distribution systems and to allow them the opportunity of participation in the electricity markets, a new idea of Virtual Power Plant (VPP) is introduced [8]-[10].

The energy management capability of VPPs was explored by various researches [11]-[14]. For example, study [11] investigates the issue of renewables' management in power systems, which takes into account a VPP that aggregates these distributed sources. According to study [12], VPP integrates wind generation with electric vehicles (EVs) in a stochastic scope at the same time considering uncertainty. A real case study [13] was set up to investigate the energy balancing capability of VPP, in which the VPP technology is used as an instrument for load aggregation to manage the balancing services. In addition, the optimal dispatch of VPPs with several approaches is considered in [14].

Yet, VPP's most significant aspect is its capability to manage DERs, so that they are involved in electricity markets indirectly. In this regard, recent studies have applied different approaches [15]-[18].

Presented in [15] is a probabilistic price-based unit commitment method, which employs a point estimate approach to manage the uncertainties that VPP should deal with in its offering model. The bidding problem of VPP in energy and spinning reserve markets is discussed in [16]. The offering strategy is a price-based unit commitment configuration, in which the genetic algorithm is determining the resulting optimization in the solution methodology. Demand response programs can be utilized within VPP as proposed in [17]. As for small generation resources like combined heat and power (CHP), they are handled by intermittent renewable generations and coordinated together via the VPP concept to participate in the markets, as shown in [18]. This research considers stochastic optimization that assesses the optimal bidding strategy of the VPP.

In the studies presented above, there are only constructed single block hourly offers. What is remarkable is that the day-ahead (DA) electricity market gives the opportunity to submit offers in several stages with a pair of power and price variables each. That is why a VPP should have this capacity of putting its multi-step offers to the market and consequently manage different risk levels more productively.

Moreover, these studies employ a stochastic optimization model, which means the same scenarios for all the uncertainty resources. VPPs analyze DERs uncertainty together with the market price uncertainty, unlike conventional power plants. The nature of uncertainty sources is clearly different; that is why the same approach in modeling them does not accurately reflect their uncertain behavior. More than that, scenario-based approaches only lead to an enormous number of scenarios creating computational issues. VPP may require a faster optimization run, for instance, less than thirty minutes, in order to update its strategy with the latest data available. Multi-step offers for VPP and a three-stage stochastic bi-level optimization model are introduced [19]. Moreover, for the progression of the optimal bidding strategy, the multiple scenarios and computational overload are considered. A new model of separating wind and price uncertainty is suggested in reference [20], where a robust adaptive optimization is presented. But this model displays one battery only. In case the assets handled by VPP increase, their time consumption is a lot higher than desired when VPP wants a near closing-gate update of its strategy.

Indeed, it is difficult to predict the uncertainty of renewable resources, which is more severe than the price uncertainty. Thus, we were motivated to employ a well-known approach in addition to optimization under severe uncertainty known as information-gap decision theory (IGDT). This approach gives users the opportunity to define decision-making problems without a new assumption on the probability density function (PDF) of the uncertain factors and with low computational burden [22]. It is more natural to predict the behavior of the market price by a scenario-based model. On the other hand IGDT can be more suitable for a renewable source like wind generation.

In this study, a novel approach to the offering strategy of the VPP participating in the DA electricity market is proposed. The VPP consists of wind-power generation, several small-scale storage facilities, a conventional generation resource, and deferable load. We model two different uncertainties that VPP should manage. In our model, the scenario-based stochastic approach is applied to handle market price uncertainty, and IGDT is incorporated in the optimization model, accounting for wind-power production uncertainty. By doing so, we can formulate the strategic offering problem as a stochastic IGDT-based model optimization. We utilize a risk-aversion facet while dealing with the realization of the wind power generation, namely a robust strategy. In the robust strategy, instead of maximizing VPP profit by making assumptions on wind power fluctuations in each price scenario, the presented model calculates a maximum horizon of wind production that wind power can fluctuate within it. Therefore, a certain pre-determined amount of the objective function is guaranteed. After deriving the possible range of fluctuations, we present a solution methodology by incorporating ADMM to calculate the final offering strategy curve. The offering curve is constructed by applying the proposed method, so that each step of the curve would guarantee a certain amount of the objective function.

III. MATHEMATICAL FORMULATION

Deterministic Model

We consider a VPP that consists of wind generation along with a battery capacity that comes from several storages, a conventional power plant, and demand. Demand comprises inflexible and flexible parts. The first kind should be supplied on time; the second can be modified if necessary.

The overall formulation is presented as follows.

$$\max \sum_t \{\pi_t^{DA} p_t^{DA} D - Cost_t\} \tag{1}$$

$$p_t^{DA} = p_t^w + p_t^C + p_t^{dis}\,\eta^{dis} - p_t^{ch} - p_t^D \qquad \forall t \in T \tag{2}$$

$$p_t^{dis} = \sum_i p_{t,i}^{dis} \qquad \forall t \in T \tag{3}$$

$$p_t^{ch} = \sum_i p_{t,i}^{ch} \qquad \forall t \in T \tag{4}$$

$$E_{f,i} \geq E_{0,i} \qquad \forall i \in I \tag{5}$$

$$E_{f,i} = E_{0,i} + \sum_t \{e_{t,i}^{ch}\,\eta_{ch} - e_{t,i}^{dis}\} \quad \forall t \in T, \forall i \in I \tag{6}$$

$$e_{t,i}^{ch} = p_{t,i}^{ch} D \qquad \forall t \in T, \forall i \in I \tag{7}$$

$$e_{t,i}^{dis} = p_{t,i}^{ch} D \qquad \forall t \in T, \forall i \in I \tag{8}$$

$$p_{t,i}^{dis} \leq \overline{DR}(1 - u_{t,i}^{ch}) \qquad \forall t \in T, \forall i \in I \tag{9}$$

$$p_{t,i}^{ch} \leq \overline{CR}\; u_{t,i}^{ch} \qquad \forall t \in T, \forall i \in I \tag{10}$$

$$e = e^{B}_{t-1,i} + e^{ch}_{t,i}\eta_{ch} - e^{dis}_{t,i} \qquad \forall t \in T, \forall i \in I \tag{11}$$

$$e^{B}_{t,i} = E_0 + e^{ch}_{t,i}\ \eta_{ch} - e^{dis}_{t,i} \qquad t=1, \forall i \in I \tag{12}$$

$$e^{B}_{t,i} = E_f \qquad t=T, \forall i \in I \tag{13}$$

$$cost^{deg}_{t,i} = \pi^{B}\ e^{dis}_{t,i} \qquad \forall t \in T, \forall i \in I \tag{14}$$

$$e^{B}_{t,i} \geq E_{min} \qquad \forall t \in T, \forall i \in I \tag{15}$$

$$e^{B}_{t,i} \leq E_{max} \qquad \forall t \in T, \forall i \in I \tag{16}$$

$$p^{D}_{t} = p^{D}_{a,t} + p^{D}_{b,t} \qquad \forall t \in T \tag{17}$$

$$\underline{p^{D}_{t}} \leq p^{D}_{t} \leq \overline{p^{D}_{t}} \qquad \forall t \in T \tag{18}$$

$$\sum_{t} p^{D}_{t} D \geq e^{day} \qquad \forall t \in T \tag{19}$$

$$Cost_t = cost^{CP}_{t} + cost^{deg}_{t,i} \qquad \forall t \in T \tag{20}$$

$$cost^{CP}_{t} = u^{c}_{t} C_0 + p^{c}_{t} C_p + u^{su}_{t} C_{su} \qquad \forall t \in T \tag{21}$$

$$u^{c}_{t}\, \underline{P^{c}_{t}} \leq p^{c}_{t} \leq u^{c}_{t}\, \overline{P^{c}_{t}} \qquad \forall t \in T \tag{22}$$

$$u^{su}_{t} \geq (u^{c}_{t} - u^{c}_{t-1}) \qquad \forall t \in T \tag{23}$$

$$e^{dis}_{t},\ e^{ch}_{t},\ u^{su}_{t} \geq 0 \qquad \forall t \in T \tag{24}$$

VPP must meet its demand requirements while participating in the DA electricity market to optimize its defined objective. Here, like other power plants, VPP is seeking a maximized profit as presented in (1). This equation is a simple formula that maximizes accumulation of the amount of energy sold (or bought) in the DA electric market, p^{DA}, multiplied by price, π^{DA}, and duration of each optimization period, D, minus the operation cost of VPP at time t. The duration of the optimization is T, the total period, which in our case is equal to 24 hours. The power that VPP trades in the DA electricity market should equal to its available power coming from the assets it represents. This is shown in (2). Here, η^{dis} is the efficiency in discharging process.

The battery has its own set of constraints represented in (5)-(16). Note that VPP can enjoy several storage units with different types. This is considered in (3) and (4) accounting for the accumulative discharge and charge of these DERs, respectively.

We define the final energy of i^{th} battery, $E_{f,i}$, greater than its initial value, E_0 shown in (5). This prevents the VPP from depleting the battery and not charging it back. $E_{f,i}$ is the amount that battery gets charged and discharged plus its initial value as presented in (6). Since discharging the battery decreases its energy, it is declared with negative sign. Variables $e^{ch}_{t,i}$ and $e^{dis}_{t,i}$ are energy needed to charge and discharge the i^{th} battery, respectively. Parameter η_{ch} is the charging efficiency. These energies are cumulative power regarding charging and discharging the battery in the duration D also shown in the equations (7) and (8).

Charging and discharging have their own limiting rates. These limits come from specification of the battery and charging facility. These limitations are depicted in the constraints (9) and (10). Here, $\overline{CR}$, and, $\overline{DR}$, are the maximum charging and discharging rate, respectively. We utilize $u^{ch}_{t,i}$, which is a binary that prevents simultaneous charging and discharging at time t. Parameter $u^{ch}_{t,i}$ is 1 when battery is getting charged.

The remaining energy of the i^{th} battery at time t, $e^{B}_{t,i}$, is given in (11). This energy depends on its previous state at (t-1) and the charging/discharging action of the last interval. The battery energy should have two specific values at the beginning and the ending time of charging/discharging periods as depicted by (12) and (13) for t=1 and t=T, respectively.

When VPP utilizes the battery, it can eventually decrease its useful life, imposing extra cost also known as degradation cost. Many recent studies have addressed this issue by investigating the impact of charging and discharging of different batteries on their cycles [26]-[28]. To avoid further complexity and non-linearity in our model, we select the approach proposed in [28]. Similarly, we penalize VPP for every discharge of the battery by considering a price coefficient, π^{B}, for every kWh energy utilized in the process as shown in (14).

Finally, battery energy at each period is bounded to minimum, E_{min}, and maximum, E_{max} values which is represented by constraints (15) and (16).

The constraints (17)-(19) are demand related. Demand consists of two parts, inflexible, $p^{D}_{a,t}$, and flexible, $p^{D}_{b,t}$. Demand value is bounded between its minimum, $\underline{p}^{D}_{t}$, and maximum, $\overline{p}^{D}_{t}$, values at time t defined in (18). Besides, the overall consumption in the next day cannot be less than a certain amount, e^{day}, depicted in (19).

The remaining set of constraints describes cost function which is mentioned in the objective function. This cost includes degradation cost and cost of generating power with conventional power plant, $cost^{CP}_{t}$ presented in (20). The latter as described by (21), is consisting of three parts: fixed cost, $u^{c}_{t}C_{0}$, variable cost based on the generated power, $P^{C}_{t}C_{p}$, and start up cost, $u^{su}_{t}C_{su}$. According to the generator specification, its produced power is limited to the range depicted in (22). The relation between variables of conventional plant is given in the (23). At last, non-negative variables are addressed in equation (24).

B. Stochastic Risk-Averse Reformulation

The model described in the section II-A is a deterministic model with the assumption that all of the parameters are known at the time a decision is being made. What happens in reality is a different case as some data for the decision maker are ambiguous. Subsequently, the problem that VPP deals with is an optimization under uncertainty.

There are many methods in the literature that can produce reliable and accurate scenarios for market prices, but the situation is different for the wind power due to the weather dependence. This can happen in many other cases when uncertainty sources have different natures. This necessitates a new approach with the ability to address different kinds of uncertainty sources with proper modeling. In this regard, we propose the following formulation for the introduced optimization problem to be added to the previous formulation.

$$\max\ (p^{DA}_{t,\omega}) \quad \xi_{\omega} \tag{25}$$

s.t:

$$R^{R}_{\omega} \geq R^{R}_{0} \tag{26}$$

$$R^{R}_{0}=R^{R}_{0}\ (1-\gamma) \tag{27}$$

$$R^{R}_{\omega}=\min(p^{w}_{t,\omega}) \sum_{t}\{\pi^{DA}_{t,\omega}\ p^{DA}_{t,\omega}\ D\text{-}Cost_{t,\omega}\} \tag{28}$$

$$|p^{w}_{t,\omega}-\hat{p}^{w}_{t}|/\hat{p}^{w}_{t} \leq \xi_{\omega} \tag{29}$$

$$Cost_{t,\omega}=cost^{deg}_{t,\omega}+cost^{CP}_{t,\omega}+cost^{LS}_{t,\omega}+cost^{WS}_{t,\omega} \tag{30}$$

$$cost^{LS}_{t,\omega}=\pi^{LS}\ p^{LS}_{t,\omega} \tag{31}$$

$$cost^{WS}_{t,\omega}=\pi^{WS}\ p^{WS}_{t,\omega} \tag{32}$$

As it can be perceived from the above optimization declared in the (25)-(29), there are two different levels of optimization. The upper level which is a maximization problem is the overall optimization provided that the minimum amount of revenue is already calculated from the lower level. In this level, the range of wind production is maximized. The profit that VPP makes in this scenario, R^{R}_{ω}, as a risk-averse, and the predetermined revenue value, $R^{D}_{0}(1-\gamma)$, are defined in (26) and (27), respectively. Here, R^{D}_{0} is the revenue calculated from the deterministic model with expected values for the price and wind generation. This value can be tuned by parameter γ. The bigger values for γ result in smaller amounts of the minimum expected revenues. The outcomes are more robust for smaller minimum expected revenues.

In the lower level, the minimum revenue of the VPP is found, stated by R^{R}_{ω}, in the constraint (28). This minimum is found inside a range that wind power can fluctuate within, represented in (29). Here, $\hat{p}^{w}_{t}$ is the nominal value for wind production at time t.

Note that other constraints in the deterministic optimization are applicable provided that an extra index of scenario is added for variable sets and uncertain parameters. However, since we do not know the exact future values of uncertain parameters, their realizations are presented in each scenario. Despite having a conventional power plant, we consider options of shedding loads (inflexible load), $cost^{LS}_{t,\omega}$, and wind spillage, $cost^{WS}_{t,\omega}$, as it is represented in (30). These costs are calculated according to (31) and (32), where π^{LS} is cost of shedding demand power, $p^{LS}_{t,\omega}$, and π^{WS} is for wind spillage power, $p^{WS}_{t,\omega}$, at time t and scenario ω.

So far we have simulations for every scenario. However, we are solving the optimization for 24 hours and we want to build a non-decreasing offer curve. This will add the following extra constraint on the whole optimization:

$$p^{DA}_{t,\omega'} \geq p^{DA}_{t,\omega''} \text{ if } \pi^{DA}_{t,\omega'} \geq \pi^{DA}_{t,\omega''}, \quad \forall t,\omega',\omega'' \tag{33}$$

This new constraint is added to previous optimization to build offer curves properly. This new optimization can be solved utilizing available commercial solvers. However, when VPP has many dispersed sources like EVs utilized as storage, the computation time can be huge considering several scenarios of electric prices. In this regard, we apply decomposition method of ADMM [29] to decompose this equation which binds all of scenarios and solve each scenario separately to increase calculation speed.

IV. RESULTS

In this section, the effectiveness of the proposed methodology would be investigated using a BARON solver via GAMS software [30]. The purpose is to obtain the best strategy for the day-ahead market. The test system is with a 3 MW conventional generation system, four wind units with a rated capacity of 1 MW, and two different energy storage devices. Also, 50 different scenarios are generated for modeling the price of electricity at different hours. Fig. 1 demonstrates an example of 10 different scenarios for the electrical energy price. Furthermore, the data for conventional unit is given in Table I.

TABLE I

Conventional Unit Characteristics

Start up cost ($)	Cost of operation ($/MW)	Fixed cost ($)	Generation capacity (MW)
100	70	10	3

In order to implement the proposed algorithm, first, the deterministic model has been solved to obtain the minimum expected revenue, which equals to $ 1130. The average output power for different entities is depicted in Fig. 2. We consider this value as the minimum revenue in the IGDT based model. Now the model is solved for different values of γ which is varying from 0 to 1. The variation of the robustness (degree of reaching the minimum expected performance) ξ versus the variation of γ is shown in Fig. 3. It can be seen from this figure that the robustness is at least 0.40922 and reaches 0.78238 in its maximum value. By increasing γ, the minimum expected value for the revenue decreases. It shows that the system operator is taking less risk for bidding in the day-ahead market due to the uncertainties of the wind turbines generation. The value of ξ gives the

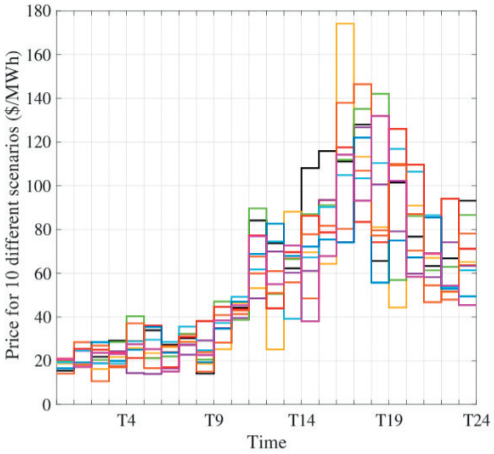

Fig. 1. Electricity price in 10 different scenarios

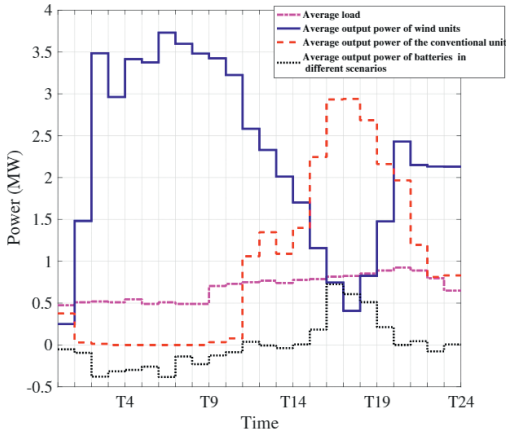

Fig. 2. The average output power for different entities

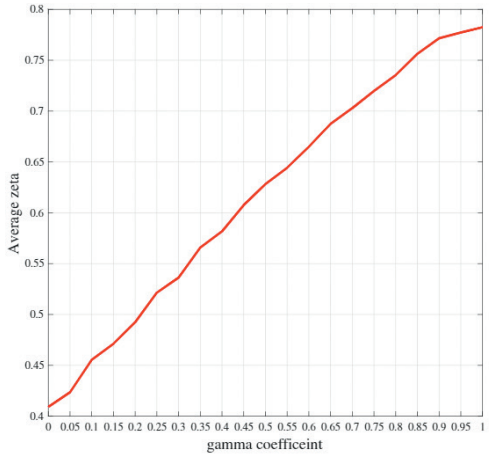

Fig. 3. Robustness versus γ

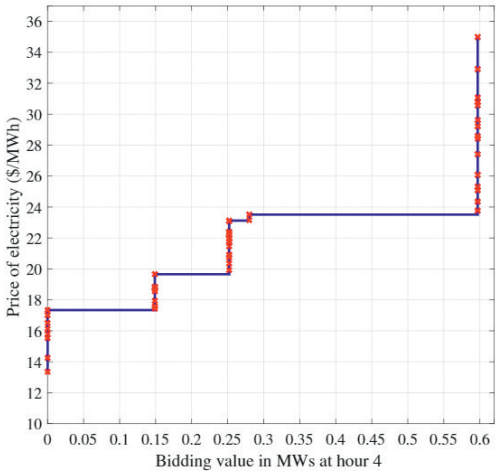

Fig. 4. Day-ahead bidding curve for hour 4 in $\gamma = 0.3$

system operator a perspective about the maximum acceptable deviation of wind generation units with the predicted values. In other words, the wind generation should be limited in the $1-\xi_{\omega}\hat{p}^{w}_{t}$, to guarantee to the operator of the VPP, that its revenue would be at least $R^{D}_{0}(1-\gamma)$ which is predicted by means of the deterministic model. However, robustness comes with a cost in a case where it may reduce the possible achievable outcome. For instance, where in the next day wind generation is noticeably more than the prediction.

Also, the bidding curves for some selected hours for γ equal to 0.3, are depicted in Fig. 4 and 5. In each hour, according to the scenarios of the electricity price, different offering values are obtained. In this case, the revenue of the VPP owner in case of limiting the output generation of the wind unit in the $1-\xi_{\omega}\hat{p}^{w}_{t}$ is guaranteed to be at least $ 791. Similar parameters for the selected hours for γ equal to 0.6 are shown in Fig. 7 and 8. It is noteworthy that in this case the revenue of the VPP owner in condition of limiting the output generation of the wind unit in the $1-\xi_{\omega}\hat{p}^{w}_{t}$ is guaranteed to be at least $ 452. Comparing the results of these two case studies indicates that by increasing the value of γ, and consequently the robustness of the model, the offering values are decreased.

Also, it should be mentioned that using the ADMM method, and relaxing the complicating constraint, helps the problem to be solved with higher speed. The original problem is solved within 736 seconds considering 50 scenarios for the prices while utilizing the ADMM approach; the solution time is reduced to 93 seconds using GAMS software with Intel Core i7 CPU under Windows 10 operating system.

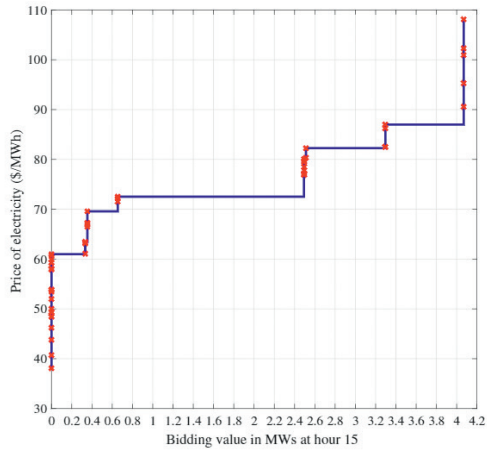

Fig. 5. Day-ahead bidding curve for hour 15 in $\gamma = 0.3$

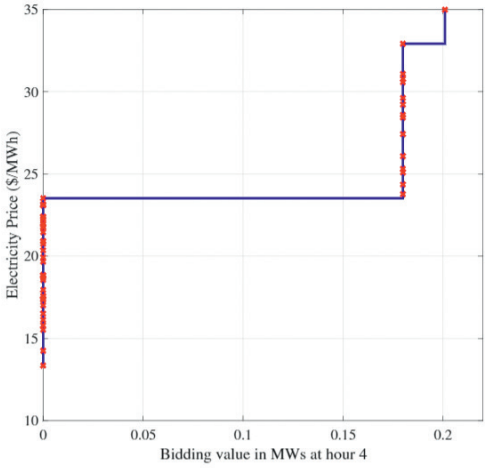

Fig. 6. Day-ahead bidding curve for hour 4 in $\gamma = 0.6$

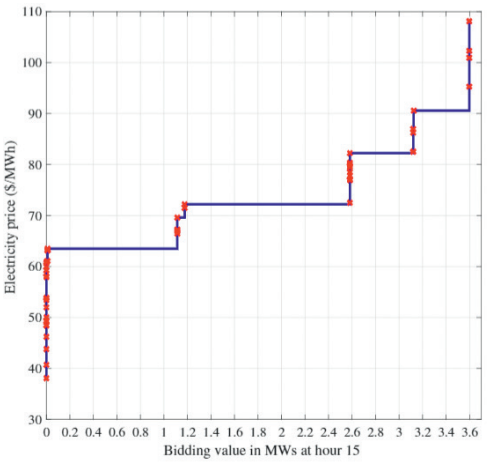

Fig. 7. Day-ahead bidding curve for hour 15 in $\gamma = 0.6$

Furthermore, to illustrate the effectiveness of the proposed fast ADMM based approach, the number of scenarios for the electricity price is increased. A comparison of the execution times with conventional method and fast ADMM based approach is illustrated in Table II. As the number of scenarios is increasing, both times are increased; however, the increment in the ADMM based approach is much less than the conventional method. For instance, in case of solving the problem with 250 scenarios, the execution time by applying the ADMM approach is reduced from three hours to approximately nine minutes.

TABLE II

Execution Time of the Proposed Method vs a Conventional Approach

Number of scenarios	**Execution time (s)**	
	Conventional method	**Proposed algorithm**
50	736	93
100	2568	178
150	5498	295
200	10304	385
250	13468	489

V. CONCLUSION

VPPs generally have multiple sources of energy generation with intermittent power productions. In this regard, a VPP could deal with different sources of uncertainty. Hence, to participate in the electricity market, VPP needs to govern these energy sources with the related uncertainties to achieve its desired goal. In this paper, an offering strategy for a VPP is proposed taking price and wind production uncertainties into account. VPP can develop its strategy with robust (risk-averse) actions. Robust actions in the proposed offering strategy promise a minimum profit if the wind production falls within a maximized variation range. The numerical simulations verify the applicability of the proposed approach. The obtained results from case studies show that in different price scenarios the proposed method leads to a more profitable result in comparison with the conventional case and ADMM leads to lower computational time.

VI. REFERENCES

[1] C. Jung, L. Grau, "Achieving Germanys wind energy expansion target with an improved wind turbine siting approach," Energy Conversion and Management, vol. 173, pp. 383–398, 2018.

[2] S. Bolwig, G. Bazbauers, D. Lund, D. Blumberga, "Review of modeling energy transitions pathways with application to energy system flexibility," Renewable and Sustainable Energy Reviews, vol. 101, pp. 440–452, 2019.

[3] M. Karmellos, G. Mavrotas, "Multi-objective optimization and comparison framework for the design of Distributed Energy Systems," Energy Conversion and Management, vol. 180, pp. 473–495, 2019.

[4] X. Wang, M. Jin, W. Feng, G. Shu, Y. Liang, "Cascade energy optimization for waste heat recovery in distributed energy systems," Applied Energy, vol. 230, pp. 679–695, 2018.

[5] T. Liu, D. Zhang, T. Wu, "Standardized modeling and economic optimization of multi-carrier energy systems considering energy storage and demand response," Energy Conversion and Management, vol. 182, pp. 126–142, 2019.

[6] J. Baak, Bringing DER Into the Mainstream: Regulations, Innovation, and Disruption on the Edge, Innovation and Disruption at the Grid's Edge, ch. 9, pp. 167–186, 2017.

[7] T. Wilberforce, A. Baroutaji, J. Thompson, A. G. Olabi, "Prospects and challenges of concentrated solar photovoltaics and enhanced geothermal energy technologies," Science of The Total Environment, vol. 659, pp. 851–861, 2019.

[8] M. Othman, Y. G. Hegazy, A. Y. Abdelaziz, "Electrical energy management in unbalanced distribution networks using virtual power plant concept," Electric Power Systems Research, vol. 145, pp. 157–165, 2017.

[9] O. Adu-Kankamab, L. M. Camarinha-Matosa, "Towards collaborative Virtual Power Plants: Trends and convergence," Sustainable Energy, Grids and Networks, vol. 16, pp. 217–230, 2018.

[10] H. Abbasi, M. Taki, A. Rajabi, L. Li, J. Zhang, "Coordinated operation of electric vehicle charging and wind power generation as a virtual power plant: A multi-stage risk constrained approach," Applied Energy, vol. 239, pp. 1294–1307, 2019.

[11] M. Javad, M. Gandomkar, and J. Nikoukar, "Optimal management of renewable energy sources by virtual power plant," Renewable Energy, pp. 1180–1188, 2017.

[12] L. Wei, J. Huanhuan, L. Junwei, Z. Kangting, C. Qingkun, T. Zhongfu Tan, "Multi-objective stochastic scheduling optimization model for connecting a virtual power plant to wind-photovoltaic-electric vehicles considering uncertainties and demand response," Energy Conversion and Management, vol. 128, pp. 160–177, 2016.

[13] V. Ferrando, "Energy balancing across cities: Virtual Power Plant prototype and iURBAN case studies," Entrepreneurship and Sustainability, pp. 351–363, 2017.

[14] Y. Liu, M. Li, H. Lian, X. Tang, C. Liu, C. Jiang, "Optimal dispatch of virtual power plant using interval and deterministic combined optimization," International Journal of Electrical Power Energy Systems, vol. 102, pp. 235–244, 2018.

[15] M. Peik-Herfeh, H. Seifi, and M. K. Sheikh-El-Eslami, "Decision making of a virtual power plant under uncertainties for bidding in a day-ahead market using point estimate method," Int. J. Elect. Power Energy Syst., vol. 44, pp. 88–98, 2013.

[16] E. Mashhour, S. M. Moghaddas-Tafreshi, "Bidding strategy of the virtual power plant for participating in energy and spinning reserve markets - part i: Problem formulation," IEEE Trans.Power Syst., vol. 26, no. 2, pp. 949–956, 2012.

[17] N. Pourghaderi, M. Fotuhi-Firuzabad, M. Moeini-Aghtaie, M. Kabirifar, "Commercial Demand Response Programs in Bidding of a Technical Virtual Power Plant," IEEE Transactions on Industrial Informatics, 2018.

[18] J. Zapata Riveros, K. Bruninx, K. Poncelet, "Bidding strategies for virtual power plants considering CHPs and intermittent renewables," Energy Conversion and Management, vol. 103, pp. 408–418, 2015.

[19] G. Kardakos, K. Simoglu, "Optimal Offering Strategy of a Virtual Power Plant: A Stochastic Bi-Level Approach," IEEE Trans. Smart Grid, vol. 7, no. 2, pp. 794–806, 2016.

[20] A. Baringo, L. Baringo, J. M. Arroyo, "Day-Ahead Self Scheduling of a Virtual Power Plant in Energy and Reserve Electricity Markets under Uncertainty," IEEE Transactions on Power Systems, vol. 34, pp. 1881-1894, 2018.

[21] M. Kazemi, B. Mohammadi-Ivatloo, M. Ehsan, "Risk-constrained strategic bidding of GenCos considering demand response," IEEE Trans.Power Syst., vol. 26, no. 3, pp. 1367–1378, 2014.

[22] B. Mohammadi-Ivatloo, H. Zareipour, N. Amjady, M. Ehsan, "Application of information-gap decision theory to risk-constrained self-scheduling of GenCos," IEEE Trans. Power Syst., vol. 28, no. 2, pp. 1093–1102, 2013.

[23] Y. Ben-Haim, Information gap decision theory, designs under severe uncertainty, 2nd ed. San Diego, CA: Academic, Feb. 2006.

[24] K. W. Hipel, Y. Ben-Haim, "Decision making in an uncertain world: Information-gap modeling in water resources management," IEEE Trans. Syst., vol. 29, no. 4, pp. 501–517, 1999.

[25] Y. Ben-Haim, "Uncertainty, probability and information-gaps," Reliability Engineering System Safety, vol. 85, no. 13, pp. 249–266, 2004.

[26] F. Wankmjller, G. Gallagher, A. Botterud, "Impact of battery degradation on energy arbitrage revenue of grid-level energy storage," Journal of Energy Storage, vol. 10, pp. 56–66, 2017.

[27] E. Elbouchikhi, M. Benbouzid, "Optimal operational planning of scalable DC microgrid with demand response, islanding, and battery degradation cost considerations," Applied Energy, vol. 237, pp. 695–707, 2019.

[28] C. Bordin, H. Oghenetejiri, A. Crossland, I. Gutierrez, "A linear programming approach for battery degradation analysis and optimization in off grid power systems with solar energy integration," Renewable Energy, vol. 101, pp. 417–430, 2017.

[29] S. Minaee, Y. Wang, "An ADMM approach to masked signal decomposition using subspace representation," IEEE Transactions on Image Processing, vol. 28, pp. 3192–3204, 2019.

[30] A. Soroudi, Power system optimization modeling in GAMS, vol. 78. Switzerland: Springer, 2017.

A Double-Input Bidirectional High-Gain Converter for Hybrid Energy Storage System

Rahim Samanbakhsh, Parham Mohammadi, Fernando Davalos Hernandez, Peyman Koohi, Federico Ibanez

Abstract

In this research, a novel bidirectional high-gain converter is proposed for integrating hybrid energy storage systems to DC micro-grids. The proposed converter does not have voltage spikes or circulating currents since it does not apply the traditional methods such as Mutual-inductor or multi-winding transformer to reach high-gain. It also can charge and discharge battery and super-capacitors independently. Additionally, it only utilizes six switches, which is less than its counter-parts use. Besides, unlike other high voltage gain converters, it uses only three switches in every mode, so conduction losses are reduced by a steep rate. The steady-state analysis of the suggested converter was presented to validate the study, and detailed simulations was carried out for calculating the precise gain of converter. Finally, a lab prototype of the converter is constructed, and experimental results were presented.

Index Terms

Hybrid Energy Storage Systems; Supercapacitor; Battery; Multiport Converter; DC-DC Converter

R. Samanbakhsh is with the Center for Energy Science and Technology, Skolkovo Institute of Science and Technology, Skolkovo Innovation Center, Building 3, Moscow 121205, Russia. **Rahim.Samanbakhsh@skoltech.ru**

P. Mohammadi is with Department of Electrical Engineering, Amir Kabir University of Technology Tehran, Iran. **parhammh.e@gmail.com**

F. D. Hernandez is with the Center for Energy Science and Technology, Skolkovo Institute of Science and Technology, Skolkovo Innovation Center, Building 3, Moscow 121205, Russia. **F.Davalos@skoltech.ru**

P. Koohi is with the Center for Energy Science and Technology, Skolkovo Institute of Science and Technology, Skolkovo Innovation Center, Building 3, Moscow 121205, Russia. **Peyman.Koohi@skoltech.ru**

F. M. Ibanez is with the Center for Energy Science and Technology, Skolkovo Institute of Science and Technology, Skolkovo Innovation Center, Building 3, Moscow 121205, Russia. **FM.Ibanez@skoltech.ru**

I. INTRODUCTION

RENEWABLE Energy Sources (RESs) are considered the main generation source in the future grids [1],[2]. Because of intermittent nature of RESs the presence of energy storage systems in the grid is of the utmost importance. Hybrid energy storage systems (HESSs) have been used in micro-grids [2]-[11] and electric vehicles [8]-[14] because of their flexibility and excellent dynamic response.

Power electronics converters that have been used for integrating hybrid energy storage into the DC micro grid can be classified into two types, one with low voltage gain [5]-[9], [7], [15], [16] and another with high voltage gain [17-22]. Due to the problems with putting batteries and supercapacitors in series, such as stress on batteries and supercapacitor modules [23]-[24], converters with low voltage gain are not a convenient alternative for the integration of hybrid energy storage into the micro grid.

There are three main characteristics that a double input converter, which is used for the integration of hybrid energy storage to the DC micro grid, should have:

1. It should be high voltage gain.
2. It should be capable of operating in four modes. Both supercapacitor and the battery should be capable of charging and discharging independently.
3. It should have continuous input current for the battery, since switched current in the battery can reduce its lifespan.

In [25], a multi-input converter with single inductor is introduced for the integration of multiple DC sources to the DC micro grid. Although the proposed converter has the ability of bidirectional operation, it has none of the main characteristics that are mentioned above. A new converter is introduced in [26], that is capable of reconfiguration, so the problem of putting supercapacitor and batteries in series are solved.

Unfortunately, the proposed converter has switched input current for batteries and it also uses many switches, hence it is not cost-effective. One of the means that was used multiple times in the past for the integration of hybrid DC sources to the grid is multi-winding transformer [17]-[22]. These converters have advantages such as the capability of independent charging/discharging of batteries/supercapacitors, high voltage gain and ease of soft switching. The main disadvantage of these converters is the circulating current that is present in certain loads, which decreases the efficiency of the converter drastically.

In this paper, a novel non-coupled non-isolated double-input bidirectional high-gain converter is proposed that not only mitigates the problems associated with traditional high-gain converters based on multi-winding transformers, but also has the capability of independent charging/discharging process for batteries and supercapacitors.

The rest of this paper is structured as follows: in the second section, the steady state analysis of the converter is presented in both boost and buck modes. The third section reviews the control methodology of the converter. In the fourth section the performance of the converter is validated through detailed closed loop and open loop simulations by PSPICE and MATLAB/Simulink and experimental results are presented. Finally, in fifth section, the conclusion is deducted and the scope for future work is presented.

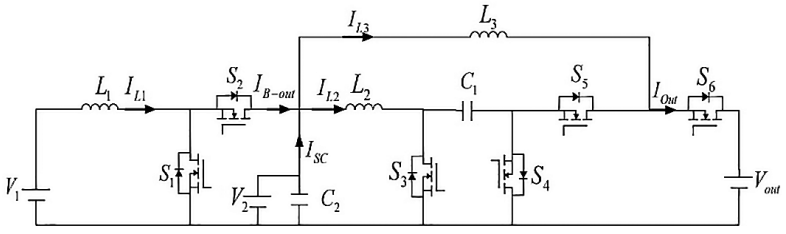

Fig. 1. Proposed topology

II. PROPOSED CONVERTER STEADY STATE ANALYSIS

The proposed DC/DC topology is shown in Fig. 1, where V_1 is the battery voltage, V_2 is the supercapacitor voltage and C_2 is the input capacitor for the supercapacitor, which composes a RC filter with supercapacitor inner resistance, so the input current of supercapacitor will be constant. The converter works in two operation modes: boost and buck modes.

A. Boost Mode

During the boost mode switches S_2, S_4 and S_6 are always turned off and their body diodes are conducting in some of the intervals. In addition, switch S_1 is switching with the duty cycle D_1, and switches S_3 and S_5 are switching with duty cycle D_2. All the gate pulses have rising edge synchronization. By applying volt-second law for three inductors, several voltage relations are found which show that D_1 and D_2 control the output voltage.

$$L_1 \rightarrow 1/T_s\int_0^{T_s} v_{L1}(t)dt$$

$$=1/T_s\left(\int_0^{D_1T_s} V_1 dt + \int_{D_1T_s}^{T_s} (V_1 - V_2)\right)dt$$

$$=0 \rightarrow V_1D_1T_s+(V_1 - V_2)(T_s - D_1T_s) \quad (1)$$

$$=0 \rightarrow V_2 = 1/(1 - D_1)V_1$$

$$L_2 \rightarrow 1/T_s\int_0^{T_s} v_{L2}(t)dt$$

$$=1/T_s\left(\int_0^{D_2T_s} V_2 dt + \int_{D_2T_s}^{T_s} (V_2 - V_{c1})\right)dt$$

$$=0 \rightarrow V_2D_2T_s+(V_2 - V_{c1})(T_s - D_2T_s) \quad (2)$$

$$=0 \rightarrow V_{c1} = 1/(1 - D_2)V_2$$

$$L_3 \rightarrow 1/T_s\int_0^{T_s} v_{L3}(t)dt$$

$$=1/T_s\left(\int_0^{D_2T_s} (V_{c1}+V_2)dt + \int_{D_2T_s}^{T_s} (V_2 - V_{out})\right)dt$$

$$=0 \rightarrow V_2D_2T_s+(V_2 - V_{out})(T_s - D_2T_s) \quad (3)$$

$$=0 \rightarrow V_{out} = (V_2 + D_2V_{c1})/(1 - D_2)$$

$$\rightarrow V_{out} = (1/(1 - D_2)^2)V_2$$

The switch S_1 is used for controlling the current of L_1 and thus controlling the battery current. Furthermore, the inductors (L_2 and L_3) current ratio can be controlled by D_2. This is demonstrated by applying the charge balance principle on C_1. Moreover, $I_{B\text{-}Out}$ is a function of D_1

$$1/T_s\int_0^{T_s} i_{C1}(t)dt = 1/T_s\left(\int_0^{D_2T_s} - I_{L3}dt + \int_{D_2T_s}^{T_s} I_{L2}\,dt\right)$$

$$=0 \rightarrow - I_{L3}D_2T_s+I_{L2}(T_s - D_2T_s) \quad (4)$$

$$=0 \rightarrow I_{L2} = I_{L3}/(1 - D_2)$$

$$1/T_s \int_0^{T_s} i_{C1}(t)dt = 1/T_s \left(\int_0^{D_2 T_s} - I_{L3} dt + \int_{D_2 T_s}^{T_s} I_{L2}\, dt \right)$$

$$=0 \rightarrow - I_{L3} D_2 T_s + I_{L2}(T_s - D_2 T_s) \tag{5}$$

$$=0 \rightarrow I_{L2} = I_{L3}/(1 - D_2)$$

and the supercapacitor average current is

$$I_{SC} = I_{B-Out} - (I_{L2} + I_{L3}) = (1 - D_1) I_{L1} - I_{L2} - (1 - D_2) I_{L2} \tag{6}$$

Notice that, from (6), the supercapacitor current can be controlled by D_1 and D_2 during the boost mode.

B. Buck Mode

During the buck mode, the switches S_1, S_3 and S_5 are always turned off and their body diodes are conducting in some of the intervals. S_2 is switching with D_1, and switches S_4 and S_6 are switching with D_2. By repeating the same procedure as in the boost mode, voltage relations for the different ports (V_1, V_2, V_{out}) can be found.

$$L_1 \rightarrow 1/T_s \int_0^{T_s} v_{L1}(t)dt$$

$$= 1/T_s \left(\int_0^{D_1 T_s} V_2 - V_1 dt + \int_{D_1 T_s}^{T_s} - V_1 dt \right)$$

$$= 0 \rightarrow (V_2 - V_1) D_1 T_s + -V_1 (T_s - D_1 T_s) \tag{7}$$

$$=0 \rightarrow V_1 = D_1 V_1$$

(a)

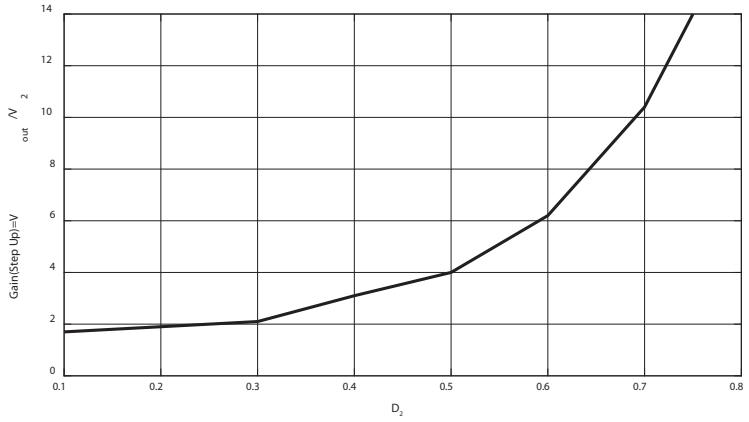

(b)

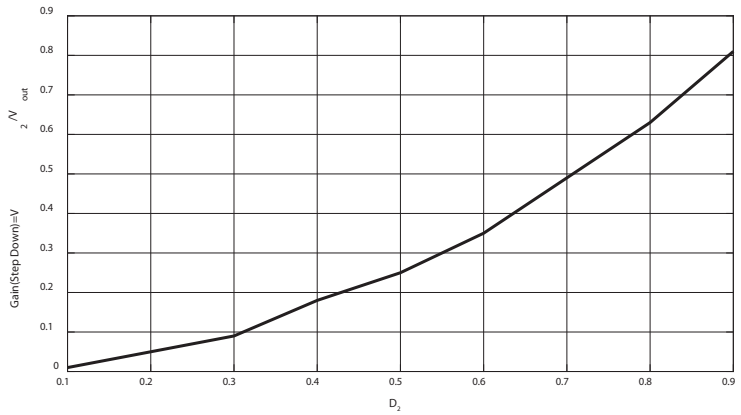

Fig. 2. Voltage gain between V_2 and V_{out} in (a) the boost mode and (b) the buck mode

$$L_2 \rightarrow 1/T_s \int_0^{T_s} v_{L2}(t)dt$$

$$= 1/T_s \left(\int_0^{D_2T_s} V_{C1} - V_2)dt + \int_{D_2T_s}^{T_s} - V_2 dt\right)$$

$$= 0 \rightarrow V_2 D_2 T_s + (V_2 - V_{C1})(T_s - D_2 T_s) \quad (8)$$

$$= 0 \rightarrow V_2 = D_2 V_{C1}$$

In this case, S_2 is used to control the L_1 current and thus controlling the battery current. This can be found by applying charge balance on C_1

$$1/T_s \int_0^{T_s} i_{C1}(t)dt = 1/T_s \left(\int_0^{D_2T_s} - I_{L2}dt + \int_{D_2T_s}^{T_s} I_{L3}\, dt\right)$$

$$= 0 \rightarrow - I_{L2} D_2 T_s + I_{L3}(T_s - D_2 T_s) \quad (9)$$

$$= 0 \rightarrow I_{L3} = I_{L2}/(1 - D_2),$$

the average $I_{B\text{-}Out}$ is proportional to D_1 and I_{L1}

$$I_{B-Out} = 1/T_s \left(\int_0^{T_s} i_{B-Out}(t)dt\right.$$

$$= 1/T_s \left(\int_0^{D_1T_s} I_{L1}\, dt + \int_{D_1T_s}^{T_s} 0 dt\right) \quad (10)$$

$$= D_1 I_{L1}$$

and the supercapacitor average current is

$$I_{SC} = I_{B-Out} - (I_{L2} + I_{L3})$$

$$= (D_1) I_{L1} - I_{L2} - (1 - D_2) I_{L2} \quad (11)$$

In the buck mode, from (11), the supercapacitor can be charged or discharged by controlling D_1 and D_2. The voltage conversion ratio between V_2 and V_{out} in buck and boost mode is depicted in Fig. 2 that were obtained by PSPICE softwere simulations, which uses the real model of switches at 300W of output power.

III. CONTROL METHODOLOGY

The control strategy of the converter is shown in Fig. 3. A low pass filter has been used to extract the high frequency component of the reference current; hence, the battery maintains slow transients, whereas the supercapacitor maintains fast transients [16], [27]. Unlike the traditional buck/boost converters, the battery current to output voltage transfer function is different from the supercapacitor current to output voltage.

Hence, a coefficient is added, so the supercapacitor injected power will be equal to the high frequency component of the power that the battery should have provided based on the reference current.

A. Open Loop Simulations Results

The voltage stress on the switches S_1, S_3 and S_5 in the boost mode is illustrated in Fig. 4a. Moreover, Fig. 4b depicts the voltage stress on the switches S_2, S_4 and S_6.

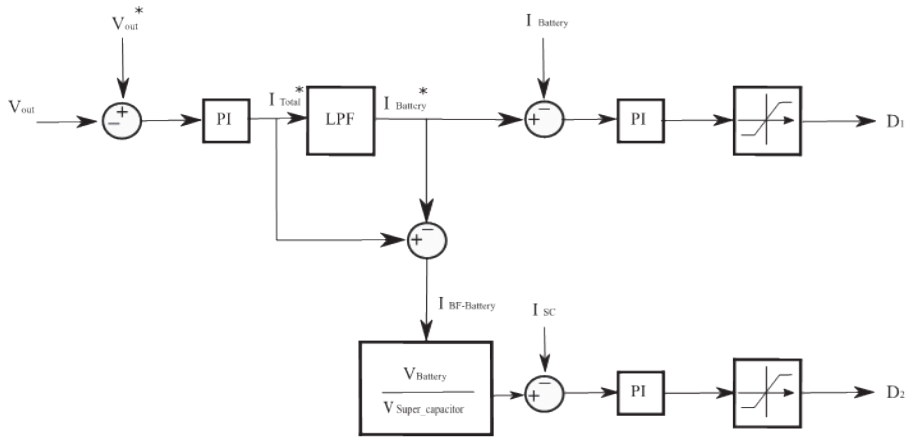

Fig. 3. Control methodology for the proposed converter

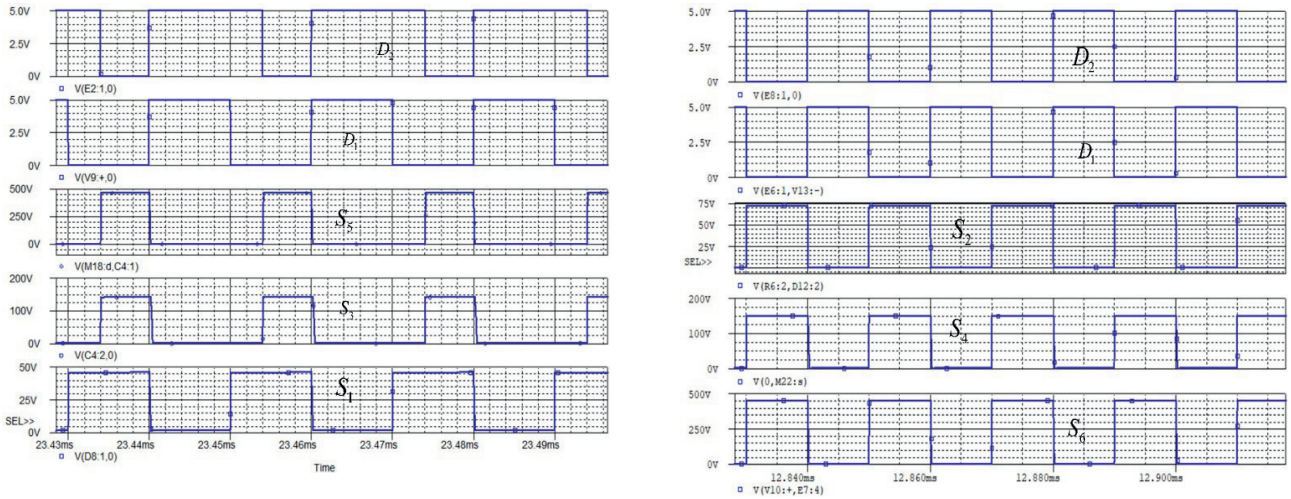

(a) (b)

Fig. 4. Voltage stress on switches (a) the boost mode and (b) the buck mode

In the boost mode the converter power is 300 W. Moreover, the input voltages and the output voltage are V_1=24 V , V_2=48 V and V_{out}=492 V. Also, the duty cycles are D_1=0.5 and D_2=0.7. The converter power is the same as in the buck mode. Also, the input voltage is V_{in}=300 V and the output voltages are V_1=37.5, V_2=75 V. The duty cycles are D_1=D_2=0.5.

The converter parameters in all the simulations are L_1=L_2=250 μH, L_3=1 mH, C_{out}=220 μ and f_s=50 kHz. As it can be seen in Fig. 5, the voltage stress on the switches is consistent with theoretical values that where calculated in section III.

B. Close Loop Simulations Results

The close loop simulation results are shown in Fig. 5. The parameters of the converter are equal to those in the open loop simulations.

One can observe that the proposed converter has the capability of independently charging and discharging the battery and the supercapacitor.

C. Experimental Results

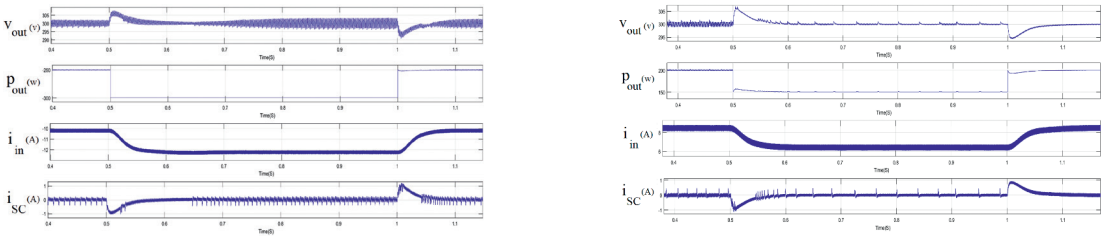

Fig. 5. Voltage stress on switches (a) the boost mode and (b) the buck mode

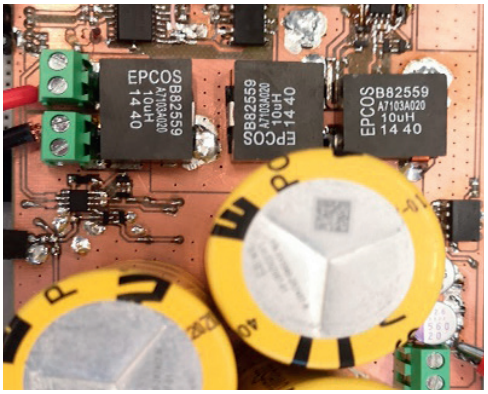

Fig. 6. Constructed prototype of the converter

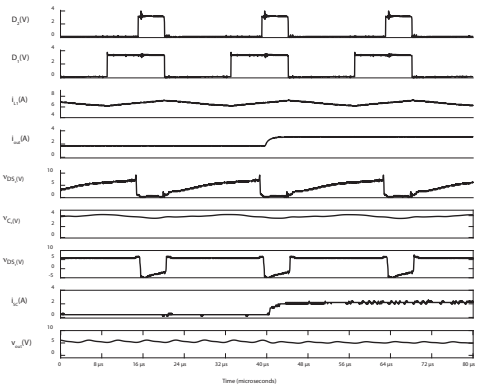

Fig. 7. Experimental waveforms of the constructed prototype

The constructed prototype of the converter is illustrated in Fig. 6. The prototype was fabricated based on a scaled version of the PSPICE model. Fig. 7 depicts the experimental waveforms of the voltage stress on some of the switches, inductor L_1 current, output voltage, output current and supercapacitor current. As it can be seen in the Fig. 7, the experimental waveforms are completely consistent with theoretical analysis.

IV. CONCLUSION

In this paper, a novel bidirectional high-gain converter was presented. The proposed converter does not use coupled inductor or transformers for achieving high gain, hence the setbacks such as voltage spikes and circulating currents do not emerge. Moreover, the introduced converter utilizes only three switches in every mode, which is a low number compared to the previous works. Hence, the conduction and switching losses are decreased by a steep rate. The steady state and efficiency were carried out and the simulations results were completely consistent with the theoretical analysis and the assembled prototype. In the future work, studies will be conducted to add soft-switching capability to the converter.

V. REFERENCES

[1] P. Mohammadi, B. Azimian, and A. Shahirinia, "A Novel Double-Loop Control Structure Based on Fuzzy-PI and Fuzzy-PR Strategies for Single-Phase Inverter in Photovoltaic Application," in 2018 North American Power Symposium (NAPS), IEEE, pp. 1–6, 2018.

[2] P. Mohammadi and J. Moghani, "Double-input high-gain bidirectional DC-DC converter for hybrid energy storage systems in DC-micro grid," in 2018 9th Annual Power Electronics, Drives Systems and Technologies Conference (PEDSTC), IEEE, pp. 312–317, 2018.

[3] C. Dong et al., "Time-delay Stability Analysis for Hybrid Energy Storage System with Hierarchical Control in DC Microgrids," IEEE Transactions on Smart Grid, 2017.

[4] S. Kotra and M. K. Mishra, "A Supervisory Power Management System for a Hybrid Microgrid With HESS," IEEE Transactions on Industrial Electronics, vol. 64, no. 5, pp. 3640–3649, 2017.

[5] B. Liu, F. Zhuo, Y. Zhu, and H. Yi, "System operation and energy management of a renewable energy-based DC micro-grid for high penetration depth application," IEEE Transactions on Smart Grid, vol. 6, no. 3, pp. 1147–1155, 2015.

[6] Q. Xu et al., "A decentralized dynamic power sharing strategy for hybrid energy storage system in autonomous DC microgrid," IEEE Transactions on Industrial Electronics, vol. 64, no. 7, pp. 5930–5941, 2017.

[7] S. K. Kollimalla, M. K. Mishra, A. Ukil, and H. Gooi, "DC Grid Voltage Regulation Using New HESS Control Strategy," IEEE Transactions on Sustainable Energy, vol. 8, no. 2, pp. 772–781, 2017.

[8] F. Akar, Y. Tavlasoglu, E. Ugur, B. Vural, and I. Aksoy, "A Bidirectional Nonisolated Multi-Input DC–DC Converter for Hybrid Energy Storage Systems in Electric Vehicles," IEEE Transactions on Vehicular Technology, vol. 65, no. 10, pp. 7944–7955, 2016.

[9] Z. Amjadi and S. S. Williamson, "Power-electronics-based solutions for plug-in hybrid electric vehicle energy storage and management systems," IEEE Transactions on Industrial Electronics, vol. 57, no. 2, pp. 608–616, 2010.

[10] M. Anun, M. Ordonez, I. Galiano, and G. Oggier, "Bidirectional power flow with constant power load in electric vehicles: A non-linear strategy for Buck+Boost cascade converters," in Applied Power Electronics Conference and Exposition (APEC-2014), pp. 1697–1703, 2014.

[11] K. Gummi and M. Ferdowsi, "Double-input dc–dc power electronic converters for electric-drive vehicles—Topology exploration and synthesis using a single-pole triple-throw switch," IEEE Transactions on Industrial Electronics, vol. 57, no. 2, pp. 617–623, 2010.

[12] L. Solero, A. Lidozzi, and J. A. Pomilio, "Design of multiple-input power converter for hybrid vehicles," IEEE Transactions on Power Electronics, vol. 20, no. 5, pp. 1007–1016, 2005.

[13] Z. Song, J. Hou, H. Hofmann, J. Li, and M. Ouyang, "Sliding-mode and Lyapunov function-based control for battery/supercapacitor hybrid energy storage system used in electric vehicles," Energy, vol. 122, pp. 601–612, 2017.

[14] F. M. Ibanez, A. M. Beizama Florez, S. Gutierrez, and J. M. Echeverria, "Extending the autonomy of a battery for electric motorcycles," IEEE Transactions on Vehicular Technology, vol. 68, no. 4, pp. 3294-3305, 2019.

[15] B. Hredzak, V. G. Agelidis, and M. Jang, "A model predictive control system for a hybrid battery-ultracapacitor power source," IEEE Transactions on Power Electronics, vol. 29, no. 3, pp. 1469–1479, 2014.

[16] N. R. Tummuru, M. K. Mishra, and S. Srinivas, "Dynamic Energy Management of Hybrid Energy Storage System with High-Gain PV Converter," IEEE Transactions on Energy Conversion, vol. 30, no. 1, pp. 150–160, 2015.

[17] H. Bai and C. Mi, "Eliminate reactive power and increase system efficiency of isolated bidirectional dual-active-bridge DC–DC converters using novel dual-phase-shift control," IEEE Transactions on Power Electronics, vol. 23, no. 6, pp. 2905–2914, 2008.

[18] C. Zhao, S. D. Round, and J. W. Kolar, "An isolated three-port bidirectional DC-DC converter with decoupled power flow management," IEEE Transactions on Power Electronics, vol. 23, no. 5, pp. 2443–2453, 2008.

[19] D. Liu, H. Li, and L. D. Marlino, "Design of a 6-kW multiple-input bi-directional DC-DC converter with decoupled current sharing control for hybrid energy storage elements," in Applied Power Electronics Conference and Exposition (APEC- 2007), pp. 509–513, 2007.

[20] H. Krishnaswami and N. Mohan, "Three-port series-resonant DC–DC converter to interface renewable energy sources with bidirectional load and energy storage ports," IEEE Transactions on Power Electronics, vol. 24, no. 10, pp. 2289–2297, 2009.

[21] H. Tao, J. L. Duarte, and M. A. Hendrix, "Three-port triple-half-bridge bidirectional converter with zero-voltage switching," IEEE transactions on Power Electronics, vol. 23, no. 2, pp. 782–792, 2008.

[22] Z. Ding, C. Yang, Z. Zhang, C. Wang, and S. Xie, "A novel soft-switching multiport bidirectional DC–DC converter for hybrid energy storage system," IEEE Transactions on Power Electronics, vol. 29, no. 4, pp. 1595–1609, 2014.

[23] H. Wu, K. Sun, L. Chen, L. Zhu, and Y. Xing, "High step-up/step-down soft-switching bidirectional DC–DC converter with coupled-inductor and voltage matching control for energy storage systems," IEEE Transactions on Industrial Electronics, vol. 63, no. 5, pp. 2892–2903, 2016.

[24] B. Narasimharaju, S. Dubey, and S. Singh, "Design and analysis of coupled inductor bidirectional DC–DC convertor for high-voltage diversity applications," IET Power Electronics, vol. 5, no. 7, pp. 998–1007, 2012.

[25] L. Kumar and S. Jain, "A multiple source DC/DC converter topology," International Journal of Electrical Power & Energy Systems, vol. 51, pp. 278–291, 2013.

[26] M. Momayyezan, D. B. W. Abeywardana, B. Hredzak, and V. G. Agelidis, "Integrated reconfigurable configuration for battery/ultracapacitor hybrid energy storage systems," IEEE Transactions on Energy Conversion, vol. 31, no. 4, pp. 1583–1590, 2016.

[27] A. Lahyani, P. Venet, A. Guermazi, and A. Troudi, "Battery/supercapacitors combination in uninterruptible power supply (UPS)," IEEE Transactions on Power Electronics, vol. 28, no. 4, pp. 1509–1522, 2013.

Distribution of Day-Ahead Forecasting Errors in the Pan-European Power System

A. Hinneck

Abstract **In this paper day-ahead forecasting errors of uncontrollable renewable sources (solar, on- and off-shore wind) in the Pan-European power system are examined. Time series published on ENTSO-E's transparency platform, by the different transmission system operators in Europe, are analyzed. The data are sourced for different regions within a 5-month period. It is shown that hardly any regional distribution of day-ahead forecasting errors follows a normal distribution, even though it is regularly assumed in literature. The analysis conducted in this paper provides a foundation for more accurate assumptions to treat uncertainty in power system models.**

Index Terms **Forecasting Errors; Forecasting Error Distributions; ENTSO-E; Day-Ahead Forecast Accuracy**

Center for Energy Science and Technology, Skolkovo Institute of Science and Technology, Skolkovo Innovation Center, Building 3, Moscow, 121205, Russia. **Anton.Hinneck@skoltech.ru**

I. NOMENCLATURE

Random variables:

$\omega_{d,s}$	Forecasting error

Empirical distributional parameters:

μ	Mean
σ	Standard deviation
γ	Skewness
κ	Kurtosis

Set elements:

d	Domain
s	Type of power source (psrType)
t	Time (resolution dependent on d and s)

Empirical data:

$C_{d,s}$	Aggregated generation capacity of a specific type s in a specific domain d
$x_{d,s}$	Vector of recorded power outputs
$\hat{x}_{d,s}$	Vector of day-ahead forecasts
$E_{d,s,t}$	Vector of recorded forecasting errors

II. INTRODUCTION

REAL-WORLD power systems are subject to uncertainty. This particularly concerns demand and generation, with an increasing penetration of uncontrollable renewable energy sources (uRES), wind and solar power plants. The share of renewable energy sources reached approximately 18% in Europe in 2018 [1] and over 50% in Germany in Q1 2020 [2]. Energy produced by uRES is non-dispatchable, which means that a generator's output cannot be increased or decreased arbitrarily in order to meet fluctuations in demand. This poses a challenge for transmission system operators (TSOs). Thus, forecasting is a vital process in the energy industry due to security (instabilities may occur [3]) and economic concerns. It facilitates obtaining an improved economic dispatch and taking full advantage of available resources [4]. Incorporating uRES into a power system requires increased flexibility of the particular system. To maintain operational security short-term balancing (by spinning reserves) is essential, to compensate for fluctuations. This requires an appropriate dimensioning of available capacity (accounting for maintenance and low utilization), and a grid that is designed under consideration of uRESs' geographical positions [5]. Integrating energy storage into a grid can additionally lessen undesirable effects of uRES [6]. Techniques summarized under the term stochastic optimization are used to treat uncertainty, not only induced by uRES, in power system models more accurately [7]. Uncertainties are incorporated into power (market) models, using two-stage or multi-stage models, chance-constraints or robust programming [8]. When accounting for uncertainties in optimal power flow [9] or unit commitment models (given sufficient wind power penetration) [10], [11], [12], accurate forecasts or information about the distributions of stochastic variables is required. The uncertain generation of uRES can be described as a mean output plus a stochastic forecasting error, which is largely assumed to follow a normal distribution [13] with zero mean [9], [14]. The Weibull [15], beta [13] and hyperbolic distribution [16] have been examined for wind power forecasting errors specifically. Moreover, studies in which statistical properties of real-world forecasting errors are derived empirically have been

conducted [17], [18], [19]. These largely show that assuming a normal distribution is barely sufficient. Regional features, forecasting methods and model parameters can cause different distributions [19]. Today's power systems are highly interconnected, crossing national borders. The organization ENTSO-E is an assembly of 42 transmission system operators from 35 countries in Europe. It ensures cooperation in operating and developing the Pan-European transmission system, as well as developing a common electricity market. Regulation 714/2009 of the European Union outlined general obligations to be implemented by ENTSO-E. These were extended by regulation 543/2013 (EU) that specifies transparency requirements. More specifically, it is outlined which data has to be made publicly available and how. These requirements are realized in the scope of the ENTSO-E transparency platform (EETP) [20]. The platform is operational since 2015 [21]. Data to be published include information on total loads, the availability of demand units and infrastructure, generation capacities and forecasts. Furthermore, an application programming interface (API) was implemented to facilitate automated data exchange between the EETP service and other applications. This feature motivates and facilitates the topic and design of this study.

Goal of this study is to empirically derive stochastic properties of industry-standard forecasting error distributions of solar power plants as well as on- and offshore wind farms. The EETP can be used to automatically obtain time series (actual data, day-ahead and incremental daily forecasts) published by European TSOs in a resolution of 15 or 60 minutes, dependent on the respective TSO. In the scope of our study, day-ahead forecasts will be considered. Compared to previous studies, data are analyzed on a higher level of detail, including a multitude of regions and power sources. It provides a broad overview of forecasting errors in industry. The methodology used below can be summarized as follows:

1. The data structure of the EETP is outlined
2. Descriptive parameters are introduced
3. Forecasting error distributions are analyzed.

III. DATA STRUCTURE

In this section the data structure, imposed by the EETP's architecture [22], [23], is described. This structure poses the foundation for accessing data in a structured manner (using the platform's API) as well as analyzing it. It is an aid to better interpret the results obtained. Several parameters are required during data access – only the most crucial will be presented, however. Of particular importance are the **domain d**, **psrType s**, **processType** and a time interval.

A. Domain

Data are structured according to domains, uniquely identified using a string ("10YDE-RWENET—I" for example). Domains refer to geographic regions. These regions are formed based on different properties, not only by national borders. A domain can reference:

1. A country;
2. A control area (CA), indicating that a single TSO is responsible;
3. A bidding zone (BZ), indicating uniform electricity prices on a wholesale level;
4. A market balancing area (MBA), indicating a uniform balancing energy price.

Taking Germany as an example, information published by each TSO, operating a specific part of the transmission grid, is available by selecting the respective CA. Therefore, even for a single country several domains might be available. This depends on how the power system in that specific country is managed. For the following analyses, it is important to note that each individual domain aggregates a different set of solar and wind power plants. Information on single generational units is not available. Additionally, all parameters in this section are interdependent. If a domain does not have a coast line for example, no data for offshore wind farms will be available. Hence, different data are available for different domains.

B. Power source type

The **psrType s** denotes the type of power source for which data are requested. Solar power plants are referenced by B16, offshore wind power plants by B18 and onshore wind power plants by B19. In the following, these internal identifiers are not used and power sources are referenced by their name exclusively. Data for different power sources like nuclear can be obtained in a similar manner.

C. Process type

The parameter **processType** specifies the information that is requested. Besides requesting realized generation data (A16), different types of forecasts are available. TSOs, distribution system operators (DSOs) and owners of generational units must provide day-ahead forecasts (A01). A day-ahead forecast must be published daily until 18:00 for the following day. Additionally, intra-day forecasts (A02) can be published. These, however, underlie no timely restrictions.

D. Time intervals

Time intervals must be defined using two points, a start called **periodStart** and an end called **periodEnd**. Dependent on the data of interest, the resolution might differ. The total installed capacity information per power source is updated on a yearly basis. Forecasts and actual generation values, on the other hand, are published in 15- or 60-minute intervals. A single observation has a time t associated with it, at which it was recorded.

IV. DESCRIPTIVE PARAMETERS

Based on the data structure, every set of observed forecasting errors is uniquely defined by a domain d and psrType (power source) s. An individual observation is referred to by the time t, at which it was recorded. Let normalized forecasting errors be defined based on a uRESs' normalized stochastic power output $x_{d,s,t}\ C_{d,s}^{-1}$. A forecast of that stochastic output is defined as follows

$$\hat{x}_{d,s,t}/C_{d,s} = 1/C_{d,s}\ (x_{d,s,t}+\omega_{d,s}), \tag{1}$$

with $x_{d,s,t}$ denoting the ground truth and forecasting error $\omega_{d,s}$ ~D (the deviation from that prediction) a random variable. Note that in what follows the forecasting errors are assumed to be independent of time. For solar power this assumption could be omitted, because predictions during night are very accurate. It allows us, at least in this study, to give a unified definition independent of the power source. Let D be some unknown distribution, which is analyzed empirically using obtained samples. Parameter $C_{d,s}$ denotes the total installed capacity by which generation and forecast values are normalized. Now, let an observed normalized forecasting error at time t be defined as

$$E_{d,s,t} = 1/C_{d,s}\ (\hat{x}_{d,s,t} - x_{d,s,t}). \tag{2}$$

Equation (2) directly follows from (1), with $E_{d,s,t}$ denoting a realization of $\omega_{d,s}$. Value $x_{d,s,t}$ denotes the actual generation, which is equivalent to the ground truth denoted in (1), at time t. The actual day-ahead forecast $\hat{x}_{d,s,t}$ is biased. The normalized deviation of $x_{d,s,t}$ and $\hat{x}_{d,s,t}$ is recorded as a realization of forecasting error $\omega_{d,s}$. A set of forecasting error observations in a predefined time frame is denoted by a vector $E_{d,s}$. The same applies for observations of actual generation $x_{d,s}$ and day-ahead forecasts $\hat{x}_{d,s}$. To analyze forecasting errors, similar sample parameters as in [19] are utilized. These are the mean $\mu_{d,s}$ of a time series, its variance $\sigma^2_{d,s}$, its skew $\gamma_{d,s}$ and its kurtosis $\kappa_{d,s}$. The values $\sigma^2_{d,s}$, $\gamma_{d,s}$ and $\kappa_{d,s}$ are the 2nd, 3rd and 4th moment about a distribution's mean [25] and alongside $\mu_{d,s}$ computed as follows:

$$\mu_{d,s} = 1/n \sum_t 1/C_{d,s}\ (x_{d,s,t} + \hat{x}_{d,s,t}) = 1/n \sum_t E_{d,s,t} \tag{3}$$

Parameter $\mu_{d,s}$ states the average forecasting error per domain and generation type,

$$\sigma^2_{d,s} = 1/n \sum_t (E_{d,s,t} - \mu_{d,s})^2 \quad (4)$$

The sample variance is denoted by $\sigma^2_{d,s}$. It provides a measure of variability. The next two parameters provide information regarding the shape of unknown distribution D. The skewness $\gamma_{d,s}$ can, like $\mu_{d,s}$, be either positive or negative,

$$\gamma_{d,s} = 1/n \sum_t (E_{d,s,t} - \mu_{d,s})^3 \quad (5)$$

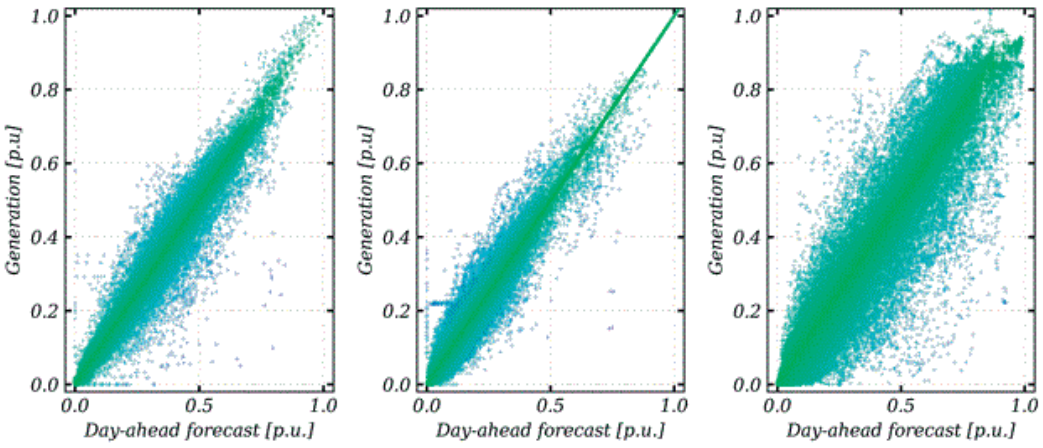

(a) Solar power **(b)** Onshore wind **(c)** Offshore wind

Fig. 1. Forecasted and actual generation by power source type

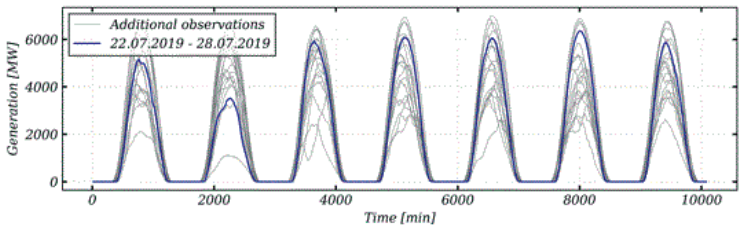

(a) Solar

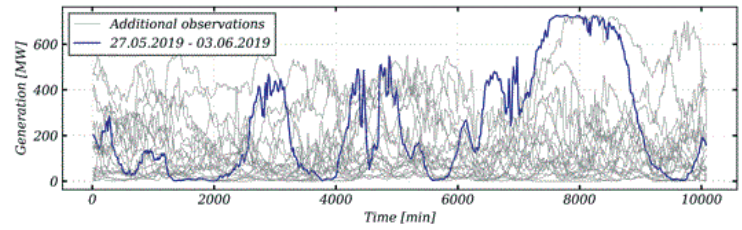

(b) Onshore wind

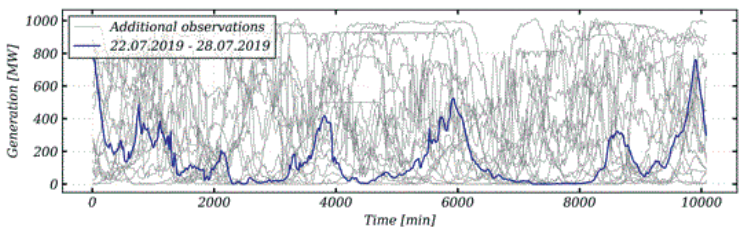

(c) Offshore wind

Fig. 2. Visualization of selected obtained time series

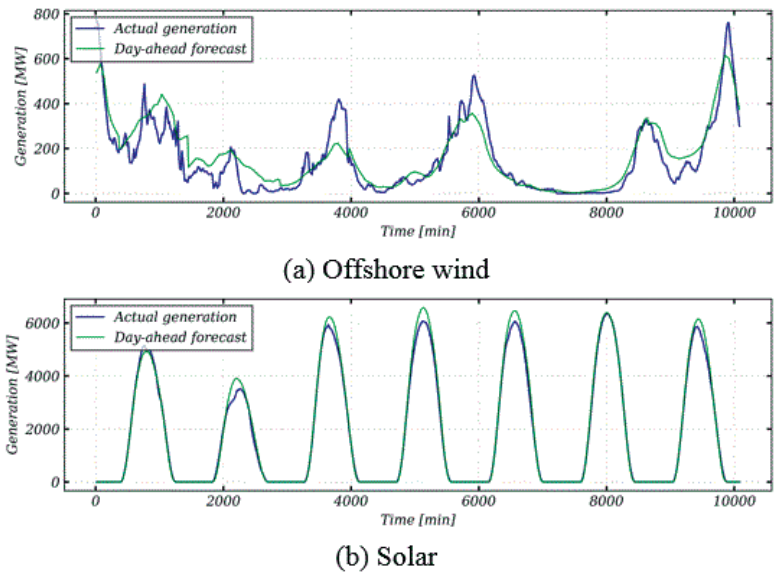

Fig. 3. Visualization of power output and day-ahead forecast

If $\gamma_{d,s} > 0$ the distribution is skew to the right and skew to the left if $\gamma_{d,s} < 0$. If $\gamma_{d,s} = 0$ it is not skew and symmetric around its average $\mu_{d,s}$. In absolute terms, if $0 \leq |\gamma_{d,s}| < 0.5$ it is fairly symmetrical. Absolute values like $0.5 \leq |\gamma_{d,s}| < 1$ and $|\gamma_{d,s}| > 1$ indicate that the underlying distribution is moderately or highly skew. Any distribution with $\gamma_{d,s} \neq 0$ is called asymmetric [25]. For a distribution's kurtosis

$$\kappa_{d,s} = 1/n \sum_t (E_{d,s,t} - \mu_{d,s})^4, \tag{6}$$

holds that $\kappa_{d,s} \geq 1$. The normal distribution has a kurtosis of 3. Distributions with higher values have higher peaks and are called leptokurtic. Smaller values result in flat distributions that are called platykurtic [25]. These parameters are fundamental for the analysis conducted below.

V. DATA ANALYSIS

The data set used in the scope of the following experiments is queried using the EETP's API. The actual power output of solar power plants, on- and offshore wind farms, as well as their respective day-ahead forecasts, were obtained. The data set consists of observations from April 1st, 2019 until August 1st, 2019. Several time series were excluded from analysis because of inconsistencies. In cases where forecasts and actual generation reports had a different number of observations (in the same time frame), the data set was discarded entirely. The same applies whenever a domain had no installed capacity associated with it, for the respective **psrType s**. In total 33 time series remained for further analysis, with 14496 or 3624 observations dependent on the resolution of data (15- or 60-minute intervals). This yields 217440 observations overall. Before discussing properties of forecasting errors, it is worthwhile to present the raw data.

A. Actual Generation and day-ahead forecasts

First the data is visualized. Fig. 1 shows the forecasted and actual normalized power output per unit (p.u.) of installed capacity. If a prediction is accurate, the observation is located on the diagonal dividing the quadrant. The more an observation deviates from that diagonal, the bigger the observed forecasting error $|E_{d,s,t}|$.

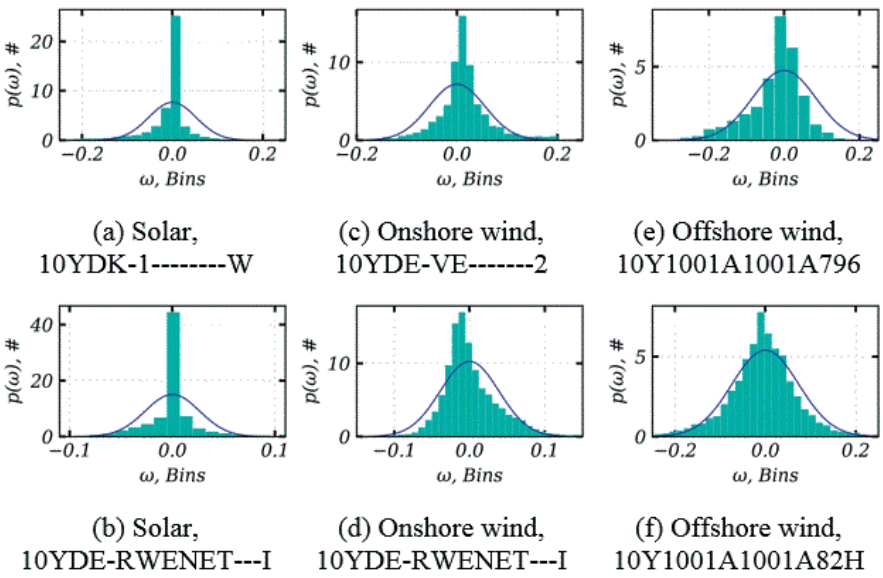

Fig. 4. Visualization of power output and day-ahead forecast

A few conclusions can be made right away. First, forecasting offshore wind, is by far the most inaccurate. This is indicated by a larger spread of observations around the diagonal. Regarding onshore wind, it can be concluded that the highest forecasting errors are recorded for medium capacity utilization. The same holds for solar, even though more observations with a high capacity utilization are recorded. Onshore wind capacity is rarely utilized beyond 80%. Generation close to the maximal power output is more frequent for offshore power plants. Fig. 1c shows a fairly even distribution of capacity utilization.

Onshore wind farms are indeed known to have a lower capacity factor than offshore [26]. Why several predictions for onshore wind farms on the top end are so accurate was not finally determined. This might be caused by inconsistencies in the data set. Even though the provision of forecasts is standardized formally, forecasting methods are not. These initial findings are confirmed by the plots in Fig. 2. It depicts energy production of solar power plants (2a), on- (2b) and offshore (2c) wind farms for a single domain. The time series are displayed on a weekly basis, with one week being highlighted. The remaining data are plotted in gray for clarity. Note that one day has 1440 minutes. This facilitates further validity checks. Solar power plants are expected to exclusively produce power during day, which is confirmed in Fig. 2a. These plots also suggest that forecasts of solar generation are generally more accurate during nights, because their power output is 0 - or at least very small. This can be observed in Fig. 2b. Generation by on- and offshore wind farms shows no obvious patterns.

On close inspection, Fig. 2c reveals fairly constant outputs in several weeks. This is likely caused by high wind speeds for several hours and find farms producing at maximum capacity. Fig. 3 depicts a day-ahead forecast and actual generation data for offshore wind production (a) and solar (b), for one week. The same generation pattern shown in Figure 3a is highlighted in Fig. 2c. The highlighted time series in Fig. 3b is also depicted in Fig. 2a. The forecast captures general trends. Deviations between forecast and actual generation are clearly visible, however. It is evident that day-ahead forecasts provide a fairly accurate approximation, but raw data does not suffice to make conclusions regarding the forecasting errors' underlying distributions.

B. Empirical distributional parameters

In this section parameters of forecasting error distributions, as presented in section III, are summarized. Figure 4 shows histograms and probability density functions (PDF) of fitted normal distributions for selected data sets. Assuming that the distribution of forecasting errors follows a normal distribution $\omega_{d,s} \sim N(0,\sigma_{d,s})$, centered at 0, the following values would be expected;

$$\mu_{\omega_{d,s}} = 0, \qquad \gamma_{d,s} = 0, \qquad \kappa_{d,s} = 3. \tag{7}$$

These are the parameters of PDFs plotted alongside the histograms. Hence, the further values deviate in the following tables from those presented in (7), the less likely $\omega_{d,s}$ follows a normal distribution. To compare between Fig. 4 and Tables I – III, the domain-specific strings are used.

Table I summarizes results for solar power plants. Compared to offshore wind farms (Table II) the sample wwmeans and variances are relatively small. This was already pointed out in Fig. 1. Several time series show skew and are leptokurtic, which is visible in Fig. 4a and 4b. Compared to the density function of the fitted normal distributions, the histograms accurately depict these properties. This is confirmed numerically by the values displayed in Table I.

TABLE I

Solar power plants

Domain d	**Country**	**C_d [MW]**	**μ_d**	**σ_d^2**	**γ_d**	**κ_d**
10YDE-VE 2	Germany	11443	0.0009	0.0297	-0.115	6.3011
10YDE-RWENET I	Germany	10874	-0.0012	0.0265	0.49	7.3464
10YBE 2	Belgium	3369	-0.0012	0.0398	-0.2174	6.2966
10YCZ-CEPS N	Czech Republic	2049	-0.0014	0.0292	-0.4348	8.5062
10Y1001A1001A65H	Denmark	1014	-0.0096	0.0451	-1.3987	8.2807
10YDK-1 W	Denmark	672	-0.0106	0.052	-1.51	8.3061
10YDK-2 M	Denmark	342	-0.0076	0.0519	-0.7976	10.6617
10Y1001A1001A796	Denmark	1014	-0.0096	0.0451	-1.3987	8.2807
10YSI-ELES 0	Slovenia	275	-0.0076	0.076	-1.9305	12.1633
10YES-REE 0	Spain	6751	-0.0008	0.0392	-1.1244	4.006
10YDE-EON 1	Germany	16838	0.0023	0.0244	0.3565	5.3639

Interestingly, most μ_d are negative. This implies that the power output of these generators is forecasted conservatively – systematically assuming less power output than actually is available. Whereas the mean of forecasting errors in Spain is closest to zero, in the first data set for Denmark, it deviates the most. The skew is also mostly negative, indicating that the underlying distributions are skew to the left.

The parameters of offshore wind farms' forecasting errors (Table II) generally show higher means and variances. Also, regional installed capacities are well behind solar and onshore wind farms. Offshore wind farms are more expensive in general

TABLE II

Offshore wind farms

Domain d	**Country**	**C_d [MW]**	**μ_d**	**σ_d^2**	**γ_d**	**κ_d**
10YDE-VE 2	Germany	1068	-0.0297	0.1252	-0.4793	3.072
10Y1001A1001A82H	Germany, Luxemburg	6393	-0.0074	0.0739	-0.25	1.3762
10Y1001A1001A65H	Denmark	1700	-0.0244	0.084	1.3026	37.2553
10YDK-1 W	Denmark	1277	-0.0326	0.1067	1.5166	44.1786
10YDK-2 M	Denmark	423	0.0	0.0937	-0.2591	5.0396
10Y1001A1001A796	Denmark	1700	-0.0244	0.084	1.3026	37.2553
10Y1001A1001A83F	Germany	6393	-0.0074	0.0739	-0.25	1.3762
10YDE-EON 1	Germany	5325	-0.0029	0.084	-0.2122	1.6357

[26]. This is due to higher installation costs, as well as higher expenses for operation and maintenance. Levelized costs of electricity are twice as high than that for onshore wind farms. Therefore, potentials for onshore generation are utilized to a higher degree. The same applies for solar. Histogram 4f, displaying forecasting errors for domain 10Y1001A1001A82H, indicates a comparatively little γ and κ. It looks fairly centered and symmetrical. This is confirmed by the empirical parameters computed for this domain. Parameters of domain 10Y1001A1001A796 (Fig. 4e) show a large positive value for γ. It is clearly observable that the empirical distribution of forecasting errors shown in histogram 4e is skew to the right.

TABLE III

Onshore wind farms

Domain d	Country	C_d [MW]	μ_d	σ_d^2	γ_d	κ_d
10YDE-VE 2	Germany	18425	-0.0036	0.0343	0.5793	3.3347
10YDE-RWENET I	Germany	10686	0.0012	0.0389	0.7052	3.6101
10YBE 2	Belgium	2248	-0.0141	0.0381	-0.2284	2.8274
10Y1001A1001A65H	Denmark	4426	0.0002	0.0405	-1.6774	16.4841
10YDK-1 W	Denmark	3669	-0.0023	0.0438	-1.8971	21.3461
10YDK-2 M	Denmark	757	0.0122	0.0555	-0.1038	4.7748
10Y1001A1001A796	Denmark	4426	0.0002	0.0405	-1.6774	16.4841
10Y1001A1001A39I	Estonia	462	0.0163	0.0452	0.8646	5.2464
10YNO-2 T	Norway	572	-0.0	0.0007	-42.126	1962.6937
10YNO-3 J	Norway	357	-0.0003	0.0065	-24.0791	615.7231
10YNO-4 9	Norway	301	-0.0021	0.0128	-8.2824	95.3976
10YNO-0 C	Norway	1230	-0.0006	0.0037	-8.3624	90.8098
10YPL-AREA S	Poland	5808	0.0109	0.0443	-0.1493	1.4479
10YES-REE 0	Spain	22961	-0.0029	0.0258	0.4343	2.7664

The analysis of day-ahead onshore wind farm forecasting errors is summarized in Table III. Two histograms of onshore wind farms' forecasting error distributions are also shown in Figure 4. Based on the histogram alone, the forecasting errors in domain 10YDE-RWENET I (Fig. 4d) are more skew than in domain 10YDE-VE 2 (Fig. 4c). Furthermore, the kurtosis seems to be slightly higher. This, again, is confirmed numerically. Especially the empirical means and variances of forecasting error distributions lie within a moderate range. Regarding skew and kurtosis, significant differences were found. A few general properties can be derived. Table IV summarizes the frequency of parameters $\mu_{d,s}$, $\gamma_{d,s}$, $\kappa_{d,s}$ that lie within a certain range. It can be seen that the majority of sample means is not equal to 0. More importantly, for the majority of averages holds that $\mu_{d,s} < 0$. Similarly, the empirical skewness $\gamma_{d,s} \neq 0$ ($\forall$ d,s), though about half of the empirical distributions show to be fairly symmetrical. Lastly, the majority of distributions are leptokurtic. Dependent on the time series, assuming a normal distribution seems justifiable in several cases. Figure 4f depicts such a case. Fig. 4 also shows that differences between an empirical distribution and a fitted normal distribution can be severe. Based on the results presented in Table IV, assuming a normal distribution is hardly justifiable as a general approach.

TABLE IV

Summary of sample parameters

μ_d	$\gamma_{d,s}$	$\kappa_{d,s}$
$\mu_d=0$	$0\leq\lvert\gamma_{d,s}\rvert<0.5$	$\kappa_{d,s}\leq 3$
$\mu_{d,s}\neq 0$	$0.5\leq\lvert\gamma_{d,s}\rvert<1$	$3\leq\kappa_{d,s}$
$\mu_{d,s}\leq 0$	$1\leq\lvert\gamma_{d,s}\rvert$	-

VI. CONCLUSION

In this paper, forecasting errors obtained from the EETP were analyzed. Results clearly show that forecasting errors cannot in general be sufficiently well represented by normal distributions. Developing stochastic optimization approaches that account for this, could help to model power systems more reliably. After all, the penetration of renewable energy sources is expected to increase further. More insights could be gained, increasing the amount of data analyzed. Mentioning that many time series were discarded, finding the reason of inconsistencies might facilitate to further extend experimental results. Besides fitting a normal distribution, Weibull, beta and hyperbolic distributions could be employed for comparison. Even truncated or skewed normal distributions might be more suited to better represent the distributions' skew. How such distributions can be accounted for in power system models is a subject of future research.

VII. REFERENCES

[1] Share of renewable energy in gross final energy consumption in Europe. European Energy Agency. Available at: https://www.eea.europa.eu/ data-and-maps/indicators/renewable-gross-final-energy-consumption-4/ assessment-4 (accessed: 19.05.2020).

[2] Renewables make up over half of Germany's power mix. Deutsche Welle. Available at: https://www.dw.com/en/renewables-make-up-over-half-of-germanys-power-mix/a-52986924 (accessed: 19.05.2020).

[3] J. O. G. Tande, "Exploitation of wind-energy resources in proximity to weak electric grids," Appl. Energy, vol. 65, pp. 395-401, 2000.

[4] L. Landberg, G. Giebel and H. A. Aalborg, T. Nielsen, and H. Madsen, "Shortterm Prediction - An Overview," Wind Energy, pp. 273–280, John Wiley & Sons, 2003.

[5] B. Parsons, E. Ela, H. Holttinen, P. Meibom, A. Orths, M. O'Malley, B. C. Ummels, J. O. Tande, A. Estanqueiro, E. Gomez, and J. C. Smith, "Impacts of Large Amounts of Wind Power on Design and Operation of Power Systems; Results of IEA Collaboration," Wind Power, 2008, Available at: https://www.nrel.gov/docs/fy08osti/43540.pdf (accessed: 07.08.2020).

[6] P. D. Lund and J. V. Paatero, "Energy storage options for improving wind power quality," Nordic Wind Power Conference.

[7] A. Zakaria, F. B. Ismail, M. S. H. Lipu, and M. A. Hannan, "Uncertainty models for stochastic optimization in renewable energy applications," Renewable Energy, vol. 145, pp.1543–1571, 2020.

[8] S. Talari, M. Shafie-khah, G. J. Osorio, J. Aghaei, and J. P. S. Catalao, "Stochastic modelling of renewable energy sources from operators' point of view: A survey," Renewable and Sustainable Energy Reviews, vol. 81, pp.1953–1965, 2018.

[9] D. Bienstock, M. Chertkov, and S. Harnett, "Chance Constrained Optimal Power Flow: Risk-Aware Network Control under Uncertainty," SIAM Rev., vol. 56(3), pp. 461–495, 2014.

[10] A. Tuohy, P. Meibom, E. Denny, and M. O'Malley, "Unit Commitment for Systems with Significant Wind Penetration," IEEE Transactions on Power Systems, vol. 24, pp. 592–601, 2009.

[11] S. Y. Abujarad, M. W. Mustafa, and J. J. Jamian, "Recent approaches of unit commitment in the presence of intermittent renewable energy resources: A review," Renewable and Sustainable Energy Reviews, vol. 70, pp. 217–223, 2017.

[12] P. Ruiz, C. R. Philbrick, and P. Sauer, "Wind Power Day-Ahead Uncertainty Management through Stochastic Unit Commitment," in IEEE PES Power Systems Conference and Exposition, Seattle, WA, 2009.

[13] H. Bludzuweit, J. A. Dominguez-Navarro, and A. Llombart, "Statistical Analysis of Wind Power Forecast Error," IEEE Transactions on Power Systems, vol. 23, pp. 983–991, 2008.

[14] M. A. Ortega-Vazquez and D. S. Kirschen, "Economic Impact Assessment of Load Forecast Errors Considering the Cost of Interruptions," IEEE Power Engineering Society General Meeting, 2006.

[15] K. Dietrich, J. Latorre, L. Olmos, A. Ramos, and I. Perez-Arriaga, "Stochastic unit commitment considering uncertain wind production in an isolated system," in 4th Conference on Energy Economics and Technology, Dresden, Germany, 2009.

[16] A. Florita, B.-M. Hodge, and M. Milligan, "Wind Power Forecasting Error Frequency Analyses for Operational Power System Studies," 11th Annual International Workshop on Large-Scale Integration of Wind Power into Power Systems as well as on Transmission Networks for Offshore Wind Power Plants Conference, Lisbon, Portugal, 2012.

[17] B.-M. Hodge, E. Ela, and M. Milligan, "The Distribution of Wind Power Forecast Errors from Operational Systems," in 10th International Workshop on Large-scale Integration of Wind Power, Aarhus, Denmark, 2011.

[18] D. P. Larson, L. Nonnenmacher, and C. F. M. Coimbra, "Day-ahead forecasting of solar power output from photovoltaic plants in the American Southwest," Renewable Energy, vol. 91, pp. 11–20, 2016.

[19] B.-M Hodge, D. Lew, M. Milligan, H. Holttinen, S. Sillanpaa, E. Gomez-Lazaro, R. Scharff, L. Soder, X. G. Larsen, G. Giebel, and D. Flynn, J. Dobschinski. "Wind Power Forecasting Error Distributions: An International Comparison," 11th Annual International Workshop on Large-Scale Integration of Wind Power into Power Systems as well as on Transmission Networks for Offshore Wind Power Plants Conference, Lisbon, Portugal, 2012.

[20] EETP, ENTSO-E. Available at: https://transparency.entsoe.eu/ (accessed: 19.05.2020).

[21] Official Mandates, ENTSO-E. Available at: https://www.entsoe.eu/about/ inside-entsoe/official-mandates/ (accessed: 19.05.2020).

[22] Commission Regulation 543/2013, European Union. Available at: https://eurlex.europa.eu/LexUriServ/LexUriServ.do?uri=OJ:L:2013:115:0039:0075:en:PDF (accessed: 19.05.2020).

[23] API Guide, ENTSO-E. Available at: https://transparency.entsoe.eu/content/ static content/Static\%20content/web\%20api/Guide.html (accessed: 19.05.2020).

[24] A review of the ENTSO-E Transparency Platform, VVA, Copenhagen Economics, Neon, Deloitte, Commissioned by the European Commission, 2017.

[25] M. G. Bulmer, Principles of Statistics, Second Edition, The MIT Press, 1965.

[26] Renewable Energy Technologies: Cost Analysis Series 2012. IRENA. Available at: https://www.irena.org/ documentdownloads/publications/re_technologiescost_analysis-wind_ power.pdf (accessed: 19.05.2020).

Small reviews

Approaches to Chemical Pre-Lithiation of $LiNi_{0.5}Mn_{1.5}O_4$

Roman R. Kapaev

Abstract **Designing lithium-ion batteries with higher energy density is one of the big problems in modern materials science. To address this issue, specific capacity of cathode materials needs to be enhanced. In other words, the content of lithium ions that can be reversibly extracted from the cathode has to be increased. One of the ways to add extra lithium ions to the cathode is to perform its pre-lithiation prior to the battery assembling. In contrast to electrochemical pre-lithiation techniques, chemical methods are easier to implement on a large scale and are therefore more promising for practical applications. Spinel lithium-nickel-manganese oxide $LiNi_{0.5}Mn_{1.5}O_4$ (LNMO) is an attractive candidate for lithium-ion batteries with high energy density. By applying the pre-lithiation strategy, the capacity of this material can be theoretically increased to 347 mA h g^{-1}, making it much higher compared to modern commercially available analogs. In this paper, approaches to chemical pre-lithiation of LNMO are reviewed.**

Index Terms **Lithium-ion Batteries; Cathode Materials; Pre-lithiation; Lithium Nickel-manganese Oxide**

I. INTRODUCTION

LITHIUM-ION batteries (LIBs) have become a prevalent type of energy storage devices, owing to their relatively high energy density, stability and affordable cost [1]. These batteries are now used in a multitude of applications, including various sorts of portable devices, hybrid and electric vehicles [2]-[4]. However, the energy density of the batteries still needs to be improved to make the tools and machines lighter and more autonomous. For example, a battery pack of Tesla Model S weighs >500 kg, which is about a quarter of the total mass of the car [5]-[7]; it is desirable to reduce the battery mass without sacrificing the vehicle driving range.

The energy density of a battery can be expressed as a product of its capacity, i.e., the number of lithium ions that go from the anode to the cathode during discharge, and average voltage, i.e., the difference of electric potentials between the electrodes. For a larger capacity, the battery cathode material must contain an increased content of extractable lithium in the discharged state. To add more lithium, the cathode materials might be pre-lithiated prior to cell assembling. One of the materials that can benefit from the pre-lithiation approach is lithium-nickel-manganese oxide $LiNi_{0.5}Mn_{1.5}O_4$ (LNMO) with a spinel structure. Engaging Ni^{+2}/Ni^{+4} transition, this material has a theoretical capacity of 147 mA h g^{-1} and possesses a high average redox potential of ~4.7 V vs. Li^+/Li [8], [9]. As a result, high practical specific and volumetric energies of ≥ 630 W h kg^{-1} and ≥ 2500 W h L^{-1} are achievable. However, LNMO might also be over-lithiated at lower potentials where Mn^{+4}/Mn^{+3}

Center for Energy Science and Technology, Skolkovo Institute of Science and Technology, Skolkovo Innovation Center, Building 3, Moscow, 121205, Russia. **roman.kapaev@skoltech.ru**

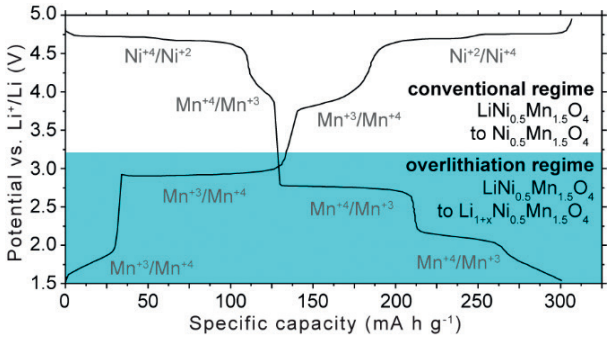

Fig. 1. Charge-discharge profiles of LNMO in 1.5-4.95 V vs. Li^+/Li potential range. Adapted from [10]

transition in engaged (Fig. 1). If all Mn^{+4} are reduced, it results in a compound with a formula $Li_{2.5}Ni_{0.5}Mn_{1.5}O_4$, which has a theoretical capacity of up to 347 mA h g^{-1} [10]. Practical capacities of ~300 mA h g^{-1} were demonstrated in 1.5-4.95 V vs. Li^+/Li range [10]. The additional capacity in the low-voltage region might be used to enhance the energy density significantly or to compensate irreversible capacity losses caused by parasitic reactions at the anode.

An electrochemical approach is the most common for electrode pre-lithiation. It involves the construction of a cell with lithium metal anode; during discharge of the cell, the cathode gets lithiated, after which the cell is disassembled, and the electrode is used in subsequent battery assembling. The main drawbacks of this method are complexity and high costs, which are caused by complicated equipment/processing techniques, as well as by the waste of resources during the pre-lithiation. As a result, this approach is applicable only on a lab-scale because of the severe problems with up-scaling. In contrast, chemical methods are potentially scalable, which makes them promising for the battery industry. This mini-review covers the existing chemical pre-lithiation processes for LNMO.

II. SOLID-STATE HIGH-TEMPERATURE PRE-LITHIATION

Asimple and scalable approach to LNMO chemical pre-lithiation was proposed by Mancini et al. [11], [12]. It requires mixing LNMO with lithium iodide, which is followed by annealing at 180-300 °C. During the annealing process, lithium is inserted into the LNMO structure, and gaseous molecular iodine is released; after cooling, the unreacted LiI is washed away with water. It was reported that the over-lithiation degree of 0.88 could be achieved, i.e., a compound with a formula $Li_{1.88}Ni_{0.5}Mn_{1.5}O_4$ is obtained [11]. For this composition, the initial charge capacity reached 262 mA h g^{-1} in the potential range of 2.4-4.9 V vs. Li^+/Li (Fig. 2a).

For the material with composition $Li_{1.5}Ni_{0.5}Mn_{1.5}O_4$, the authors assembled full cells with a standard graphite-based anode. During the first charge, the capacity of graphite shows partial irreversibility. It is due to the reaction between lithiated graphite and the electrolyte, which results in the formation of a passivation film at the graphite surface [13]. As a result, part of the cathode capacity is consumed by the anode at the first cycle. Nevertheless, a high and stable specific capacity of 160 mA h g^{-1} (based on the cathode mass) was obtained for the full cell, because of the extra lithium carried by $Li_{1.5}Ni_{0.5}Mn_{1.5}O_4$ (Fig. 2b, c).

The main advantage of this method is that it requires no sophisticated synthetic or electrochemical equipment since only a furnace is needed. However, lithium iodide is a relatively expensive reagent. Molecular iodine, which is a by-product of the pre-lithiation reaction, might theoretically be captured and recovered; however, I_2 capture requires specialized equipment, which might lead to additional expenses.

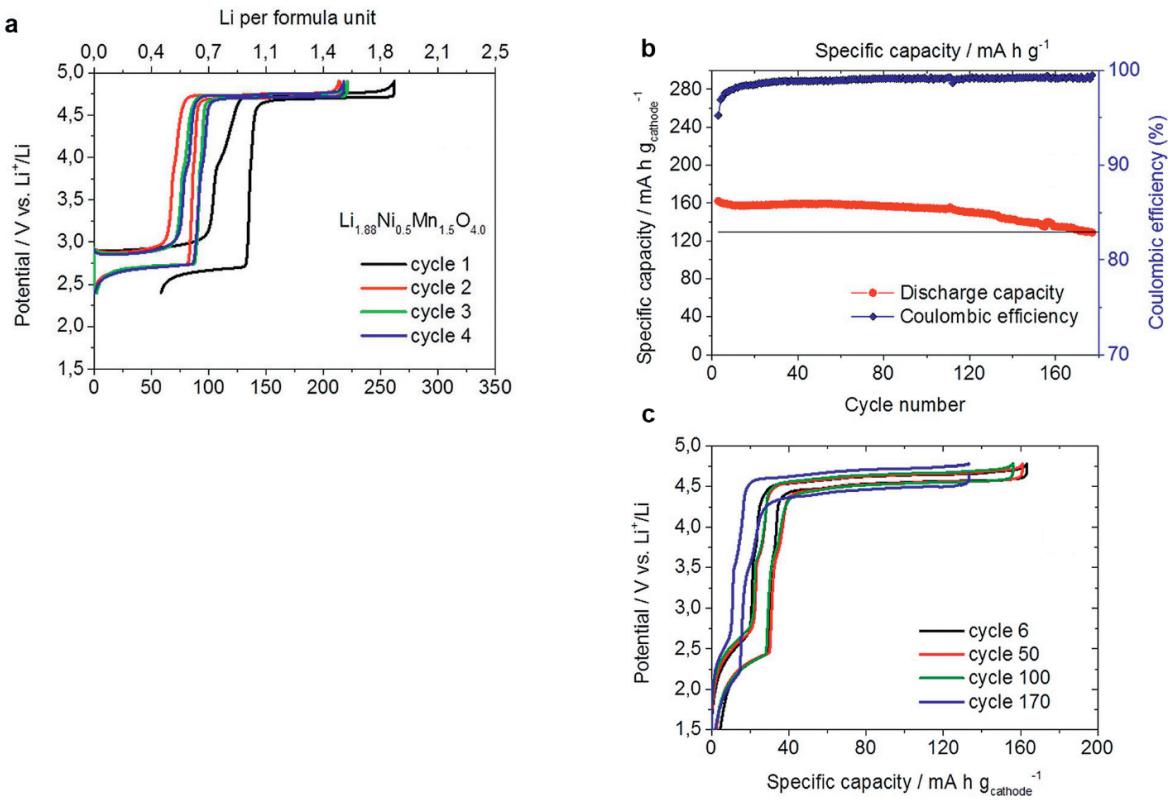

Fig. 2. (a) Charge-discharge profiles of $Li_{1.88}Ni_{0.5}Mn_{1.5}O_4$ at 30 mA g^{-1} current density; (b) cycling stability and charge-discharge profiles (c) of full cells with $Li_{1.5}Ni_{0.5}Mn_{1.5}O_4$ and graphite anode. Reproduced from [11]

III. MICROWAVE-ASSISTED PRE-LITHIATION

Another high-temperature pre-lithiation method was proposed by Manthiram and co-authors [14]. It uses tetraethylene glycol as a reducing agent and LiOH as a lithium source. The reaction is carried out at 200-300 °C in a microwave reactor (Fig. 3a). The over-lithiation degree might be controlled by adjusting the reaction time. The product with the highest lithium content, which was obtained for the longest reaction time of 45 minutes, had a composition $Li_{1.8}Ni_{0.5}Mn_{1.5}O_4$. The first cycle charge capacity for this material reached ~260 mA h g^{-1} (Fig. 3b). It might be supposed that the over-lithiation degree might be further increased by longer reaction times (one hour or more), although these studies were not reported.

The proposed pre-lithiation method is potentially scalable, although large-scale microwave synthesis might require special equipment, which will affect the production cost. Compared to the LiI-assisted solid-state approach, the over-lithiation degree should be easier to control for the glycol-assisted method by regulating the reaction time. Additionally, tetraethylene glycol and lithium hydroxide are cheaper reagents than lithium iodide.

IV. PRE-LITHIATION BY LITHIUM METAL IN LIQUID AMMONIA

Alow-temperature chemical lithiation method has recently been proposed by Johnson et al. [15]. The cathode material is placed in liquid ammonia under an inert atmosphere, followed by addition of small pieces of lithium metal. The metal dissolves in NH_3, forming a deep-blue solution of electride $[Li(NH_3)_x]^+e^-$, which acts as the reducing/lithiating agent. After 6 hours, the ammonia is allowed to evaporate by slowly increasing the temperature, and the product is washed by methanol. The over-lithiation degree is controlled by the amount of lithium metal added to the reaction mixture. If Li is added in excess, a compound with composition $Li_{1.96}Ni_{0.5}Mn_{1.5}O_4$ is formed. In general, the measured over-lithiation degree was always lower than predicted from the reaction stoichiometry. It might be explained by the presence of the side reaction of Li with NH_3,

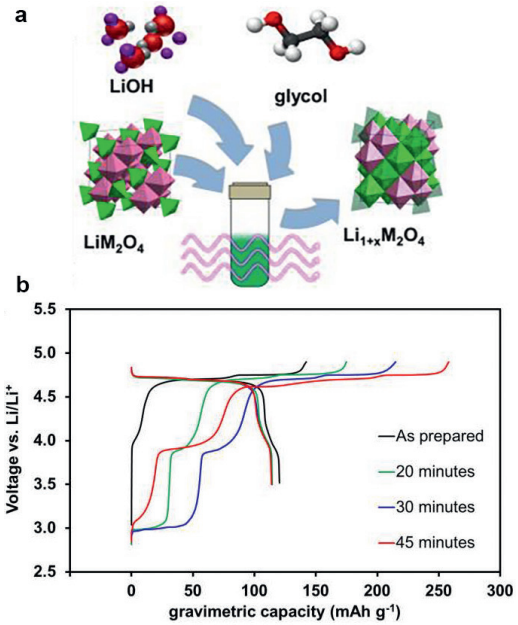

Fig. 3. (a) Schematic representation of the glycol-assisted microwave pre-lithiation approach; (b) first cycle charge-discharge profiles of pristine LNMO and pre-lithiated materials, which were obtained with different reaction time. Reproduced from [14]

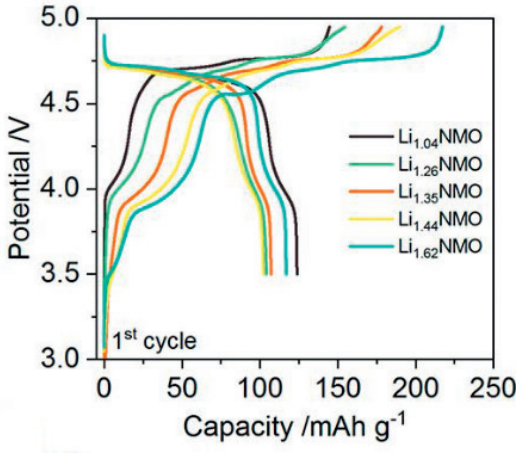

Fig. 4. First cycle charge-discharge curves for LNMO pre-lithiated with the ammonia-assisted method. Reproduced from [15]

which results in the formation of lithium amide and molecular hydrogen. For the material with the over-lithiation degree of 0.62 ($Li_{1.62}Ni_{0.5}Mn_{1.5}O_4$), the first charge capacity reached ~225 mA h g^{-1} (Fig. 4). The authors demonstrated that pre-lithiated materials increased the capacity of full cells with graphite and silicon-graphite anodes.

The ammonia-assisted approach has several disadvantages, which hinder its applicability on a large scale. Firstly, liquid ammonia has a low boiling point of -33 °C, so the temperature needs to be carefully controlled, which makes the method complicated and energy-intensive. Secondly, lithium metal is expensive, hazardous and difficult to handle, mainly because of its high reactivity with air and moisture. Thirdly, side reaction of Li and NH_3 makes the process less efficient, since an excess of lithium needs to be used.

V. PRE-LITHIATION BY LITHIUM METAL IN PENTANOL

A similar solution-based pre-lithiation approach has been recently proposed by Betz and co-authors [10]. To carry out the lithiation, LNMO is stirred at 139 °C with metallic lithium in refluxing pentanol for 13 hours (Fig. 5a). Pentanol reacts with Li, forming lithium alkoxide and hydrogen, which acts as a reducing agent. As in the case with the ammonia-mediated

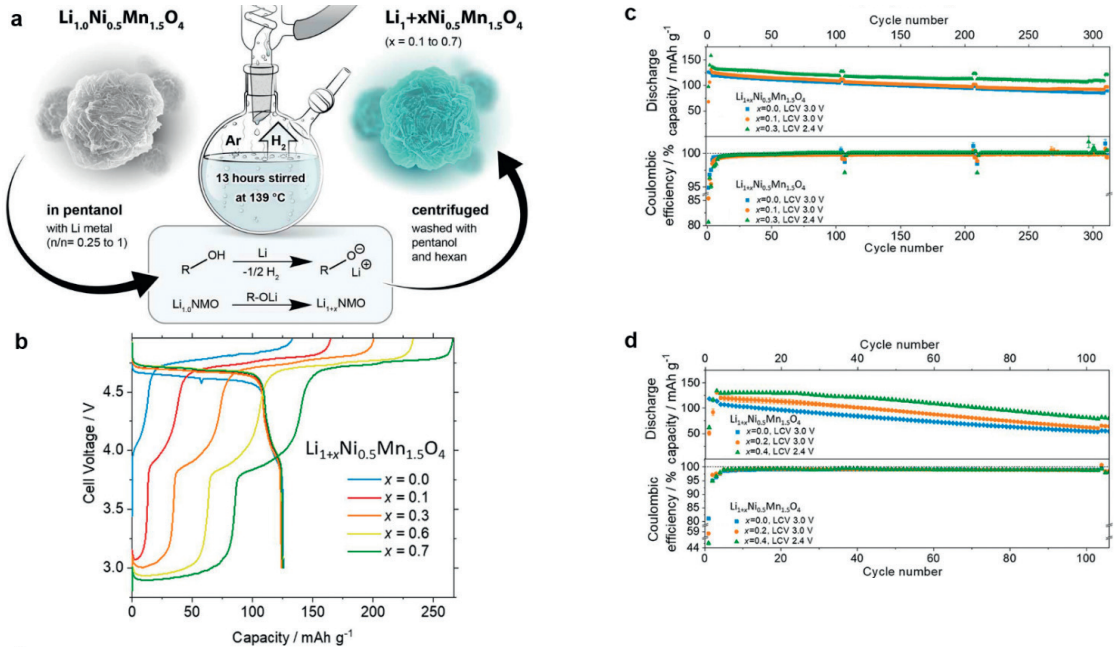

Fig. 5. (a) Schematic representation of the pentanol-assisted lithiation process; (b) first cycle charge-discharge curves for LNMO and its pre-lithiated derivatives; cycling stability of full cells with LNMO and its pre-lithiated derivatives as the cathodes and (c) graphite or (d) silicon-graphite as the anodes. Reproduced from [10]

approach, the over-lithiation degree is controlled by the amount of lithium added to the reaction mixture. Actual over-lithiation degrees are also lower than the ones predicted from the reaction stoichiometry, suggesting that side processes, like molecular hydrogen leaving the reaction mixture, take place. When the molar ratio between lithium and LNMO was 1:1, the over-lithiation degree was 0.7 ($Li_{1.7}Ni_{0.5}Mn_{1.5}O_4$). The first cycle charge capacity for this compound approached ~260 mA h g^{-1} (Fig. 5b). Over-lithiated materials were evaluated in full cells with graphite or silicon-graphite anodes. They demonstrated higher specific capacities, energy densities and better cycling stability compared to pristine LNMO (Fig. 5c, d).

This chemical lithiation approach also has limited practical applicability and is more suitable on the lab scale. As mentioned above, lithium is an expensive and dangerous reagent, which is especially pronounced at elevated temperatures. Hydrogen, which is one of the reaction by-products, is also hazardous, since it may form explosive mixtures with air. The efficiency of the process is far below 100%, so excessive lithium needs to be added. In addition, the reaction takes a long time (>10 h), which makes it time and energy-consuming.

VI. CONCLUSION

To summarize, several chemical pre-lithiation approaches have been proposed for $LiNi_{0.5}Mn_{1.5}O_4$, each of which has its drawbacks. The most straightforward protocol involves heating LNMO with lithium iodide. However, the approach will likely be costly without the possibility of recovering iodine, which is a rare element. On the other hand, iodine recovery will increase the complexity of the equipment needed for the pre-lithiation. Even if iodine is recovered, extra cost will appear from the repeated LiI synthesis. The cheapest pre-lithiation reagents are used in the glycol-assisted method, which, however, requires a microwave reactor to function; it is currently unclear whether the microwaves might be replaced by conventional heating, which should be much cheaper. Ammonia-assisted and pentanol-assisted approaches are suitable only on the lab-scale since they require hazardous reducing agents, prolonged reaction time or/and complicated temperature control. For all reported chemical pre-lithiation methods, the over-lithiation degree was limited to <1, typically approaching 0.6-0.8. It might be supposed that using stronger reducing agents will result in higher over-lithiation degrees. Developing the protocols, which allow higher first charge capacities, should be a subject of further studies.

VII. REFERENCES

[1] M. Li, J. Lu, Z. Chen, and K. Amine, "30 years of lithium-ion batteries," Adv. Mater. [Online], vol. 30(33), pp. 1800561, 2018. Available: https://doi.org/10.1002/adma.201800561.

[2] R. Schmuch, R. Wagner, G. Hörpel, T. Placke, and M. Winter, "Performance and cost of materials for lithium-based rechargeable automotive batteries," Nat. Energy [Online], vol. 3(4), pp. 267–278, 2018. Available: https://doi.org/10.1038/s41560-018-0107-2.

[3] X. Zeng, M. Li, D. Abd El-Hady, W. Alshitari, A.S. Al-Bogami, J. Lu, and K. Amine, "Commercialization of lithium battery technologies for electric vehicles," Adv. Energy Mater. [Online], vol. 9(27), pp. 1900161, 2019. Available: https://doi.org/10.1002/aenm.201900161.

[4] G.E. Blomgren, "The development and future of lithium ion batteries," J. Electrochem. Soc. [Online], vol. 164(1), pp. A5019, 2016. Available: https://doi.org/10.1149/2.0251701jes.

[5] Battery Expert: Tesla Model 3 has 'most advanced large scale lithium battery ever produced' [Video]. 2018; Available: https://evannex.com/blogs/news/tesla-s-battery-pack-is-both-mysterious-and-alluring-work-in-progress.

[6] Tesla Model S. 2019; Available: http://www.roperld.com/science/TeslaModelS.htm.

[7] Tesla Battery Weight Overview – All Models. 2020; Available: https://enrg.io/tesla-battery-weight-overview-all-models/.

[8] R. Santhanam and B. Rambabu, "Research progress in high voltage spinel $LiNi_{0.5}Mn_{1.5}O_4$ material," J. Power Sources [Online], vol. 195(17), pp. 5442–5451, 2010. Available: https://doi.org/10.1016/j.jpowsour.2010.03.067.

[9] T.-F. Yi, J. Mei, and Y.-R. Zhu, "Key strategies for enhancing the cycling stability and rate capacity of $LiNi_{0.5}Mn_{1.5}O_4$ as high-voltage cathode materials for high power lithium-ion batteries," J. Power Sources [Online], vol. 316, pp. 85–105, 2016. Available: https://doi.org/10.1016/j.jpowsour.2016.03.070.

[10] J. Betz, L. Nowak, M. Winter, T. Placke, and R. Schmuch, "An Approach for Pre-Lithiation of $Li_{1+x}Ni_{0.5}Mn_{1.5}O_4$ Cathodes Mitigating Active Lithium Loss," J. Electrochem. Soc. [Online], vol. 166(15), pp. A3531–A3538, 2019. Available: https://doi.org/10.1149/2.1221914jes.

[11] M. Mancini, P. Axmann, G. Gabrielli, M. Kinyanjui, U. Kaiser, and M. Wohlfahrt-Mehrens, "A High-Voltage and High-Capacity $Li_{1+x}Ni_{0.5}Mn_{1.5}O_4$ Cathode Material: From Synthesis to Full Lithium-Ion Cells," ChemSusChem. [Online], vol. 9(14), pp. 1843–1849, 2016. Available: https://onlinelibrary.wiley.com/doi/abs/10.1002/cssc.201600365.

[12] M. Wohlfahrt-Mehrens, P. Axmann, G. Gabrielli, and M. Mancini, "Lithium-nickel-manganese-based transition metal oxide particles, production thereof and use thereof as electrode material," US20180294481A1, Oct. 11, 2018

[13] K. Edström, M. Herstedt, and D.P. Abraham, "A new look at the solid electrolyte interphase on graphite anodes in Li-ion batteries," J. Power Sources [Online], vol. 153(2), pp. 380–384, 2006. Available: http://www.sciencedirect.com/science/article/pii/S037877530500738X.

[14] Z. Moorhead-Rosenberg, E. Allcorn, and A. Manthiram, "In Situ Mitigation of First-Cycle Anode Irreversibility in a New Spinel/FeSb Lithium-Ion Cell Enabled via a Microwave-Assisted Chemical Lithiation Process," Chem. Mater. [Online], vol. 26(20), pp. 5905–5913, 2014. Available: https://doi.org/10.1021/cm5024426.

[15] W.M. Dose, J. Blauwkamp, M.J. Piernas-Muñoz, I. Bloom, X. Rui, R.F. Klie, P. Senguttuvan, and C.S. Johnson, "Liquid Ammonia Chemical Lithiation: An Approach for High-Energy and High-Voltage Si–Graphite|$Li_{1+x}Ni_{0.5}Mn_{1.5}O_4$ Li-Ion Batteries," ACS Applied Energy Mater. [Online], vol. 2(7), pp. 5019–5028, 2019. Available: https://doi.org/10.1021/acsaem.9b00695.

Microstructured Optical Fibers for Chemical and Biochemical Analysis

This work was supported by the Russian Foundation for Basic Research (RFBR grant 19-32-90249).

Timur Ermatov, Julia Skibina, Dmitry Gorin

Abstract

The current level of development of the fiber drawing technique enables the creation of custom-made structures for any particular application in biophotonics and biochemistry. Furthermore, the separate class of microstructured optical fibers (MOFs) with the structure consisting of air-channels running along the whole fiber length provides a robust platform for the in-fiber sensing devices. Here, we review the application of MOF-based sensors in chemical and biochemical analysis of different liquid and solid materials with a particular focus on refractometric measurements. The refractive index and its variation possess important information about the composition and concentration of the whole mixture as well as its separate components. In this review, we highlight the recent achievements in the field of MOF-based refractometry sensors and summarize their performance characteristics such as the limit of detection, sensitivity to the refractive index change and figure of merit.

Index Terms

Holey Fibers; Microstructured Optical Fibers; Refractive Index; Refractometry; Sensing

I. NOMENCLATURE

n	refractive index (-)
λ	wavelength (nm)
j	integer describing mode order (-)
d	thickness of capillary wall (nm)

Timur Ermatov is with the Center of Photonics and Quantum Materials, Skolkovo Institute of Science and Technology, Skolkovo Innovation Center, Building 3, Moscow, 121205, Russia. **timur.ermatov@skoltech.ru**

Julia Skibina is with the SPE LLC Nanostructured Glass Technology. **skibinajs@yandex.ru**

Dmitry Gorin is with the Center of Photonics and Quantum Materials, Skolkovo Institute of Science and Technology, Skolkovo Innovation Center, Building 3, Moscow, 121205, Russia. **d.gorin@skoltech.ru**

II. INTRODUCTION

SINCE the discovery in the late 1990s [1] and over the last twenty years, the fabrication process of the microstructured optical fibers (MOFs) have been extensively developed. This progress allows for the fiber drawing various complex structures with different geometries in a highly controllable and reproducible way. The high overlap between a light mode guided inside the fiber core and the surrounding air capillaries makes the precise analysis of the media inside the fiber possible through the measurement of the resonance position of MOFs [2]. Furthermore, the presence of air channels gives the possibility for the light-guiding and additionally renders the ability to insert liquids under test into these the air-holes. The feasibility of optical fiber-based sensors for the refractometric measurements was reported a long time ago and was demonstrated for the different fiber structures and investigated substances in both the liquid and solid forms [3]. Furthermore, all the bio-related samples such as biochemical and biomedical ones necessarily consist of the aqueous-based medium. Nowadays, the sensing of chemical and biochemical species or certain molecules usually relies on several optical phenomena including absorption, luminescence, the Raman effect, and surface plasmon resonance [4].

However, in the last couple of years, optical fiber-based refractometric sensors are realized on different principles, utilizing the combination of different fibers in a single sensor. Additionally, the application of exposed-core MOFs ensures the stronger interaction of the light mode and the sensing media [5].

Another distinctive reason for the increasing usage of MOF-based sensors that contributed to their fast development is the unique characteristics of MOF-based devices. These distinctive properties differentiate them from the traditional bulk laboratory instruments and electronic sensors, limited by big size and heavyweight, and greatly contributed to the expansion of the refractometric research area. Usually, the MOF-based biosensor consists of a light source, a set of focusing and collimating objectives and an optical spectrum analyzer or a spectrometer (Fig. 1) [6].

Among the others, one can highlight the significant properties of MOF-based sensors such as miniaturization, robust structure, flexibility, and mechanical stability, low cost, and immunity to electromagnetic and radio frequency interferences. The small capacity of air capillaries of MOFs allows the work with low volume and concentration of investigated analyte that is in the high importance in all the biological applications.

The four groups of MOFs can be defined based on their structures and light-guiding principle [7], [8]. The first two groups represent the variation of the design of the solid-core fibers which are conventional solid-core and suspended-core MOFs (Fig. 2a,b). And the other groups include the conventional hollow-core MOFs and Kagome fibers (Fig. 2c,d).

In comparison with the conventional optical fibers made of silica and its doped counterparts, MOFs are single material fibers which can be fabricated by different techniques of direct fiber drawing as well as the modern 3D printing approach [9].

This work highlights the recent progress of MOF-based sensors realized for the refractive index sensing of internal and external media. A general overview of the most relevant refractometric MOF-based sensors is reported focusing on the potential of the produced structures for future applications. The various kinds of MOFs are considered, including the suspended-core MOFs, air-cladding MOFs, and the complex interferometric-based and resonance-based MOF configurations. The key characteristics, sensitivity, resolution and the detection limit, are summarized followed by a brief discussion of the obtained results.

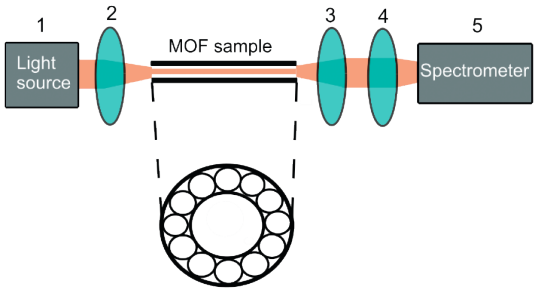

Fig. 1. Schematic overview of optical characterization setup. 1 – light source, 2,3,4 – the set of focusing and collimation objectives, 5 – spectrometer. Insert is the enface of hollow-core MOF

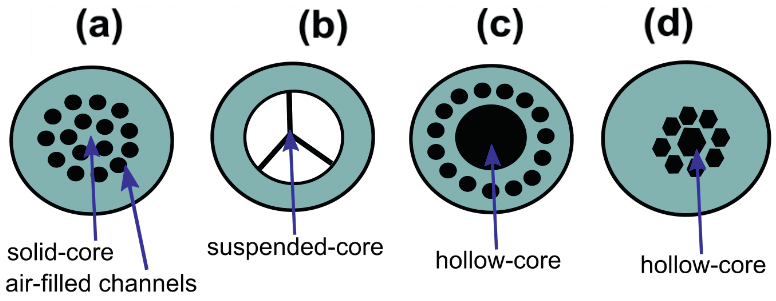

Fig. 2. Types of microstructured optical fibers. (a) solid-core MOF, (b) suspended-core MOF, (c) hollow-core MOF, and (d) Kagome fiber

The bulk refractive index sensitivity (RIS) shows the ratio of the values of the sensor output (the shift of measured optical resonances) to the variations of the bulk refractive index of the investigated substances. To calculate the bulk refractive index sensitivity of optical sensors [10], the slope of the linear fit curve is used in the form of:

$$RIS = \Delta\lambda/\Delta n, \quad (1)$$

where $\Delta\lambda$ is the shift of optical resonances and Δn is the refractive index variation.

The figure of merit (FOM) is used to normalized the bulk refractive index sensitivity to the width of the resonance peak measured at the full width at half maximum (FWHM) that defined the precision of the measurements:

$$FOM = RIS/FWHM. \quad (2)$$

III. AN OVERVIEW OF MOF-BASED BIOSENSORS

MOFs are the frequently used devices for the environmental, refractometric and liquid sensing due to the presence of the air-reservoirs inside their structure which form the perfect landscape for the interaction of the guided light mode and the medium under test [4]. A part of the MOF-based biosensors exploits the exponentially decaying (evanescent) waves, localized in the cladding of the fiber. On one hand, MOFs can be used as the sensors by themselves with a benefit of the long interaction lengths between the evanescent field and the fluid in the cavities. On the other hand, MOFs can be a part of the complex MOF-based interferometric and resonance configurations. In both cases, the produced sensors combined all the features of MOFs enabling the high sensitivities to the change of the refractive index for a wide range of substances.

A. Solid-core microstructured optical fibers

Similarly to the conventional all-solid silica optical fibers, the light guidance in the solid-core MOF is achieved due to the total internal reflection from the interface of the higher refractive index solid core and the surrounding air-cladding channels of lower refractive index (Fig. 2a). Solid-core MOFs can be tailored for a variety of optical properties such as the size of the mode area, single-mode guidance, and tunable dispersion, which are realized by the proper choice of the fiber material and its final structure [11].

The separate class of solid-core MOFs is suspended-core fibers whose core is suspended in the central hollow-channel by thin glass walls connected to a robust solid jacket (Fig. 2b). The first realization of such fibers revolutionalized the field of optical sensors due to their special design of the mutual orientation of the inflatable holes located in the direct neighborhood to the central suspended core [12]. A part of the light guided in the central solid-core is going outside to the air-channels of the surrounding cladding that ensures the strong light-matter interactions over the whole fiber length. Typically such a design enables the fabrication of the small core fibers with a diameter of tens of microns. The central core is surrounded by high capacity air-channels that enhanced an overlap between the evanescent field of the light mode propagating in the core with investigated substances of gases or liquids in surrounding air-cavities.

The further experimental realizations of suspended-core MOFs at different geometries were shown for the example of Ag-nanoparticles functionalized fibers [13].

Suspended-core MOF-based sensors for bio-sensing and refractometric analysis of different liquids have been reported in [14], [15] for the fibers utilizing the surface plasmon resonance phenomena.

The significant benefit of using MOFs with their array of air-capillaries lies in the potential for combining the long interaction lengths with strong overlapping between the light mode and the injected analyte. Based on that fact, MOF-based sensors are usually chosen instead of the other optical fiber-based sensors relying on geometry-modified all-solid optical fibers, cuvettes, and bulk optics. The recent example of the MOF-based optofluidic platform has demonstrated that suspended-core MOFs modified with gold nanoparticles, can be used for real-time bio-analyte measurements through efficient refractive index sensing [4], [14].

The group of a geometry-modified suspended-core MOFs consists of exposed-core MOFs (Fig. 3a). The removal of the cladding from the part of the fiber allows for easier access of the sensing media to the suspended core region along with the whole length of the fiber comparing to the conventional suspended-core MOFs with the enclosed core. This feature enables the study of the evanescent field intensity at various values of the analyte refractive index (Fig. 3b) [5].

The further increase of the sensitivity to the change of the refractive index can be obtained through the fiber surface modification with the special coatings or functionalized particles which ensure the specific binding of the target molecules. There are special techniques applied for the deposition of the metal coatings on the inner surfaces of both the hollow-channels and the exposed regions that allows the employment of the surface plasmon resonance phenomena to detect any variations of the refractive index of the external media possessing the great potential in chemical, biomedical, and industrial sensing.

B. Hollow-core microstructured optical fibers

The discovery and experimental realization of hollow-core MOFs was a great step forward in fiber-optic technology, leading to unique possibilities for the complex experiments realizations that overcome many existing limitations.

In contrast to the all-solid silica fibers and the solid-core MOFs, the light guidance inside in hollow-core MOFs is guaranteed by the total internal reflection principle. This group of MOFs represents the special class of waveguides operating by the principle of coherent Bragg scattering. The boundary between the air-filled hollow-core and the capillary walls forming the cladding layers is responsible that only specific wavelength bands are confined in the fiber hollow-core and allowed to propagate. The optical signal with resonance frequencies lying within this range does not guide through the structured cladding consisted of an array of air-channels but propagates along the hollow-core region.

The condition for the Bragg reflection is defined as follows:

$$2dn_1 \sin\theta = m\lambda, \tag{3}$$

where d is the thickness of the capillary wall, n_1 is the refractive index of the medium, filling the hollow-core of MOF, λ is the wavelength of the incident light, m is an integer describing mode order.

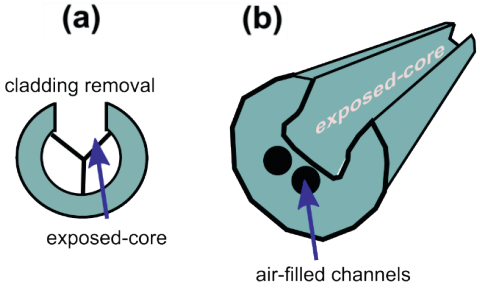

Fig. 3. Schematic of exposed-core microstructured optical fiber. (a) Fiber end-face and (b) side view

It can be seen that the change in the refractive index of the medium (n_1) causes the change in the values of λ, according to the condition (1).

Following this model, the maxima in the fiber transmission appear at [2]:

$$\lambda_j = 4n_1/(2j+1)\,(n_2^2/n_1^2 - 1)^{1/2}, \tag{4}$$

where j is an integer describing mode order (j=1,2,3,...), n_1 is the refractive index of an analyte filling the air-channels, n_2 is the refractive index of the fiber-glass and d indicates the wall thickness for the first capillary layer.

The photonic bandgap regions and the optical dispersion for different wavelengths may be controlled through the proper choice of the structure geometry only. The positions of the transmission regions of an optical signal and the photonic bandgaps are defined by the refractive index of the medium, filling the air-channel space in the hollow-core and the air-channels of the cladding.

Such filtering properties are widely used for sensing applications through the measurements of the resonance positions and their shifts as a result of the media change. Any variations of the media composition or the change of its separate components lead to the change of the refractive index that can be directly seen through the transmission spectrum measurements. Consequently, all these factors allow direct sensing, which can be performed using in-fiber configuration instead of the creation of the sensing region on the exterior of an optical fiber. The presence of central air-hole provides the possibility for an analyte injection with its simultaneous analysis through the transmission spectra measurements leading to real-time performance. The surface plasmon resonance-based sensors can be also achieved using the hollow-core MOFs through the deposition of the selective or complete coating with the metal layers and the further filling with analytes.

The position of the optical resonances and their change concerning the liquid filling can be described as follows [7]:

$$\lambda_{fill}=\lambda[(n_{glass}^2 - n_{fill}^2)/(n_{glass}^2 - 1)]^{1/2}, \tag{5}$$

where λ is the wavelength of the unfilled MOF, $n_{\_glass\wedge}$ is the refractive index of the fiber-glass and n_{fill} is the refractive index of the filling.

The change in the transmission spectra of MOFs due to the variation of the refraction index of the medium filling the air-channels makes it possible to use the MOF-based sensors for the analysis of the refractive indices of liquids and gas substances. Based on this phenomena, the numerous sensors were realized with the hollow-core MOFs. Different liquid materials were investigated. The review of the MOF-based biosensors can be found in the following references [6], [16].

The functionalization of the inner glass surfaces of the hollow-capillaries leads to the creation of the MOF-based biosensors for the selective detection of specific molecules and DNA [4]. Recently the sensors for the detection of the cancer proteins operating on the principle of surface-enhanced Raman scattering were demonstrated [17], [18]. Several groups have also successfully realized the concept of MOF-based DNA biosensor combining the layer-by-layer assembly technique for deposition of the special coating and the transmission spectra measurements that guarantee the detection of DNA in nanoliter-scale sample volumes [19], [20].

C. Interferometric-based optical sensors

The other trend in the development of the optical fiber-based sensors is the fabrication of complex structures consisted of multiple pieces of different fibers. Hollow-core MOFs with their filtering properties coming from the photonic-band gap guidance or coherent Bragg scattering became the ideal candidates to be inserted into the produced structures. Nowadays, the most popular structures consisted of either two or three parts of different fibers which a spliced in a single sensor. Based on that approach the various temperature and humidity sensors were built [21], [22].

An overview of the other existing functionalization techniques which can potentially increase the characteristics of MOF-based sensors performance as well as the prospective application areas of the produced structures can be found in References [23]–[25]. Currently, the MOF-based biosensors have already reached such high-performance characteristics as the sensitivity to the change of the refractive index in the range of ~6500 nm per refractive index units and the figure of merit at ~90 [10].

IV. CONCLUSION

Nowadays the main fields for the usage of MOF-based sensors are chemistry and biochemistry which, in turn, are the major stimulus for their development. In this work, the main trends and prospects of MOF applications in sensing are considered. Along with the historical overview of this filed and the detailed analysis of the different groups of MOFs, we described the novel functionalization methods directed to the creation of custom made structures for the particular application in biophotonics. We have highlighted the application of modified MOF-based sensors for the selective detection of specific molecules and DNA. This is expected to promote the discovery of the new methods for diagnostics that is in the high importance for the biomedical field.

Furthermore, we described the influence of the optical properties of liquid media (biological analytes), filling the air-capillaries of MOFs, on the spectral characteristics of the waveguides. We showed that the change in the refractive index of the filling medium induces the shift of the transmission bands of MOF samples.

V. REFERENCES

[1] J. C. Knight, T. A. Birks, P. S. J. Russell, and D. M. Atkin, "All-silica single-mode optical fiber with photonic crystal cladding," Optics Letters, vol. 21, no. 19, pp. 1547–1549, 1996.

[2] A. M. Zheltikov, "Colors of thin films, antiresonant phenomena in optical systems, and the limiting loss of modes in hollow optical waveguides," Physics-Uspekhi, vol. 51, no. 6, pp. 591–600, 2008.

[3] A. M. Zheltikov, "Microstructure Fibers in Biophotonics," in Handbook of Biophotonics, J. Popp, V. V. Tuchin, A. Chiou, and S. H. Heinemann Eds. Weinheim, Germany: WILEY-VCH Verlag GmbH & Co. KGaA, 2013, pp. 77–103.

[4] T. Ermatov, S. J. Skibina, V. V. Tuchin, and A. D. Gorin, "Functionalized Microstructured Optical Fibers: Materials, Methods, Applications," Materials, vol. 13, no. 4. p. 921, 2020.

[5] L. Ding et al., "Nitric oxide optical fiber sensor based on exposed core fibers and CdTe/CdS quantum dots," Sensors and Actuators, B: Chemical, vol. 273, pp. 9–17, 2018.

[6] A. V Malinin et al., "The use of hollow-core photonic crystal fibres as biological sensors," Quantum Electronics, vol. 41, no. 4, pp. 302–307, 2011.

[7] A. M. Cubillas et al., "Photonic crystal fibres for chemical sensing and photochemistry," Chemical Society Reviews, vol. 42, no. 22, pp. 8629–8648, 2013.

[8] M. Calcerrada, C. García-Ruiz, and M. González-Herráez, "Chemical and biochemical sensing applications of microstructured optical fiber-based systems," Laser and Photonics Reviews, vol. 9, no. 6, pp. 604–627, 2015.

[9] W. Talataisong et al., "Mid-IR Hollow-core microstructured fiber drawn from a 3D printed PETG preform," Scientific Reports, vol. 8, no. 1, p. 8113, 2018.

[10] C. Caucheteur, T. Guo, and J. Albert, "Review of plasmonic fiber optic biochemical sensors: improving the limit of detection," Analytical and Bioanalytical Chemistry, vol. 407, no. 14, pp. 3883–3897, 2015.

[11] Y. Huang, Y. Xu, and A. Yariv, "Fabrication of functional microstructured optical fibers through a selective-filling technique," Applied Physics Letters, vol. 85, no. 22, pp. 5182–5184, 2004.

[12] V. S. Afshar, S. C. Warren-Smith, and T. M. Monro, "Enhancement of fluorescence-based sensing using microstructured optical fibres," Optics Express, vol. 15, no. 26, pp. 17891–17901, 2007.

[13] M. K. K. Oo, Y. Han, R. Martini, S. Sukhishvili, and H. Du, "Forward-propagating surface-enhanced Raman scattering and intensity distribution in photonic crystal fiber with immobilized Ag nanoparticles," Optics Letters, vol. 34, no. 7, pp.968-970, 2009.

[14] B. Doherty et al., "Nanoparticle functionalised small-core suspended-core fibre – a novel platform for efficient sensing," Biomedical Optics Express, vol. 8, no. 2, pp.790-799, 2017.

[15] A. Csaki et al., "Nanoparticle layer deposition for plasmonic tuning of microstructured optical fibers," Small, vol. 6, no. 22, pp. 2584–2589, 2010.

[16] J. S. Skibina, A. V. Malinin, A. A. Zanishevskaya, and V. V. Tuchin, "Photonic crystal waveguide sensing," in Portable Biosensing of Food Toxicants and Environmental Pollutants, CRC Press, 2013, pp. 1–32.

[17] U. S. Dinish, C. Y. Fu, K. S. Soh, B. Ramaswamy, A. Kumar, and M. Olivo, "Highly sensitive SERS detection of cancer proteins in low sample volume using hollow core photonic crystal fiber," Biosensors and Bioelectronics, vol. 33, no. 1, pp. 293–298, 2012.

[18] U. S. Dinish, G. Balasundaram, Y. T. Chang, and M. Olivo, "Sensitive multiplex detection of serological liver cancer biomarkers using SERS-active photonic crystal fiber probe," Journal of Biophotonics, vol. 7, no. 11–12, pp. 956–965, 2014.

[19] L. V. Nguyen, S. C. Warren-Smith, A. Cooper, and T. M. Monro, "Molecular beacons immobilized within suspended core optical fiber for specific DNA detection," Optics Express, vol. 20, no. 28, pp.29378-29385, 2012.

[20] S. A. Pidenko et al., "Controlled chemical modification of the internal surface of photonic crystal fibers for application as biosensitive elements," Optical Materials, vol. 60, pp. 283–289, Oct. 2016.

[21] Y. Cui, P. P. Shum, D. J. J. Hu, G. Wang, G. Humbert, and X. Q. Dinh, "Temperature sensor by using selectively filled photonic crystal fiber sagnac interferometer," IEEE Photonics Journal, vol. 4, no. 5, pp. 1801–1808, 2012.

[22] H. Y. Choi, K. S. Park, S. J. Park, U.-C. Paek, B. H. Lee, and E. S. Choi, "Miniature fiber-optic high temperature sensor based on a hybrid structured Fabry–Perot interferometer," Optics Letters, vol. 33, no. 21, pp. 2455–2457, 2008.

[23] S. Pissadakis and S. Selleri, Optofluidics, Sensors and Actuators in Microstructured Optical Fibers. Amsterdam, The Netherlands: Woodhead Publishing, 2015.

[24] E. P. Schartner et al., "Taming the Light in Microstructured Optical Fibers for Sensing," International Journal of Applied Glass Science, vol. 6, no. 3, pp. 229–239, 2015.

[25] E. Klantsataya, P. Jia, H. Ebendorff-Heidepriem, T. M. Monro, and A. François, "Plasmonic fiber optic refractometric sensors: From conventional architectures to recent design trends," Sensors (Switzerland), vol. 17, no. 1, p.12, 2017.

The Use of Drilling Fluids in the Well Drilling through Frozen and Hydrate Saturated Sediments in the Arctic

Valentina Ekimova, Evgeny Chuvilin

Abstract

Arctic region is one of the most prospective areas for hydrocarbon production. However, the drilling of exploration and production wells in this area is connected with a number of problems. Mainly they are related to the existence of frozen and hydrate saturated rocks, which are very sensitive to change of external conditions. Particularly, drilling mud can cause destabilization of intrapermafrost, underpermafrost, and especially relic (metastable) hydrates due to the change in thermobaric conditions and influence of chemical components. As a result, powerful methane emissions and rocks subsidence around boreholes can happen. This overview focuses on the analysis of literature dedicated to drilling mud influence on hydrate saturated sediments during well construction in permafrost regions and parameters of hydrate dissociation process as a result of mud invasion in hydrate-bearing sediments. In addition, recommendations on the mode of well drilling in permafrost conditions are analyzed. Such information can help to prevent dangerous consequences connected with unpredictable destabilization of hydrate formation. Although there is a sufficient number of publications dedicated to these questions, analysis reveals gaps in experimental data on the investigation of the most widespread drilling fluid influence (polymer non-dispersive) on the hydrate stability in frozen sediments. That is undoubtedly a complex process requiring further detailed research.

Index Terms

Arctic; Drilling Fluid; Gas Hydrates Dissociation; Methane Emission; Permafrost; Well Drilling

V. Ekimova is with the Center for Hydrocarbon Recovery Center, Skolkovo Institute of Science and Technology, Renova Lab, Building 3, Moscow, 121205, Russia. **valentina.ekimova@skoltech.ru**

E. Chuvilin is with the Center for Hydrocarbon Recovery Center, Skolkovo Institute of Science and Technology, Renova Lab, Building 3, Moscow, 121205, Russia. **e.chuvilin@skoltech.ru**

I. NOMENCLATURE

HSZ	hydrate stability zone;
HMZ	hydrate metastability zone

II. INTRODUCTION

THE Arctic region is a promising area for hydrocarbon production. However, the development of oil and gas fields there is often accompanied by a number of complications, primarily related to permafrost [1]-[4]. Frozen rocks are complex multicomponent and multiphase systems containing underground ice, natural salt solutions (cryopegs), and gas hydrates. Hence, they are especially sensitive to various local technogenic influences (thermal, mechanical, chemical, etc.) [1], [2]. The experience of drilling wells in the Arctic region shows that several hazardous events could happen during the exploratory and production wells drilling, such as technogenic thawing of the enclosing rocks, the opening of cryopegs, and gas-saturated lenses, as well as the decomposition of intrapermafrost and underpermafrost gas hydrate formations. As a result, powerful methane emissions and rocks subsidence around boreholes are observed. These negative phenomena increase risks of emergencies and the development of predicaments and lead to the increased financial costs in the operation of deposits in the Arctic [5]-[8].

It is known that special drilling fluids (or mud) are used for well cleanout during drilling of exploration and production wells [9], [10]. Drilling mud is a complex multicomponent dispersed system of suspension, emulsion, and aerated liquids. Choice of its composition depends on drilling conditions [2], [9], [11]. Thus, the composition for drilling mud in permafrost conditions must be studied and chosen with particular care to prevent the above adverse phenomena. Here, we review existing works on the interaction of drilling mud with frozen sediments containing gas hydrates, as one of the important factors in thawing frozen rocks and destabilizing gas hydrate formations during the construction of exploratory and production wells.

III. CONDITIONS OF NATURAL GAS HYDRATE EXISTENCE

Gas hydrates are crystalline non-stoichiometric compounds of ice and a hydrate-forming gas with a small molecular size, for example, such as CO_2, methane, butane, propane, nitric oxide and other gases [12]. In nature, methane is the most common hydrate forming gas. A specific feature of gas hydrates is their ability to accumulate huge volumes of gas in the clathrate structure, up to 160 volumes of gas in one volume of gas hydrate.

Natural gas hydrates remain in a stable state at high pressure and low temperatures (Fig. 1). These conditions determine the hydrate stability zone (HSZ) [12].

HSZ is part of the lithosphere and hydrosphere, with thermobaric and geochemical conditions pertaining to natural hydrate stability [13], [14]. Such conditions exist for methane hydrate inside and under frozen horizons, where the permafrost thickness is about 250-300 m [14], [15] (Fig. 2).

However, methane hydrate can exist for a long time in a metastable state at temperatures below 0 °C and pressures below equilibrium due to the effect of self-preservation [15]. The essence of the effect of self-preservation is that when the pressure drops below equilibrium, the hydrate begins to decompose into gas and water. Water, formed as a result of hydrate dissociation, at negative temperatures turns into ice shells around crystals or accumulations of gas hydrates, thereby preventing further hydrate dissociation. This ice cover provides long-term preservation even at atmospheric pressure without significant changes in hydrate gas content [17], [18].

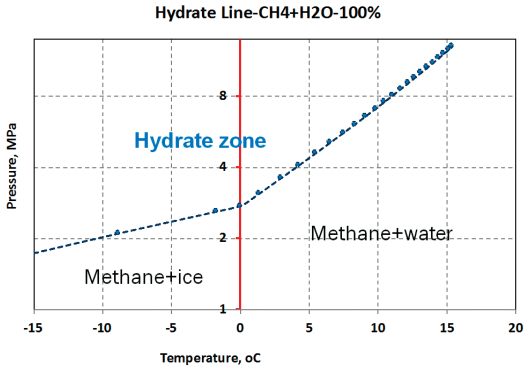

Fig. 1. Stability of methane hydrate curve (build in HydraFlash) [16]

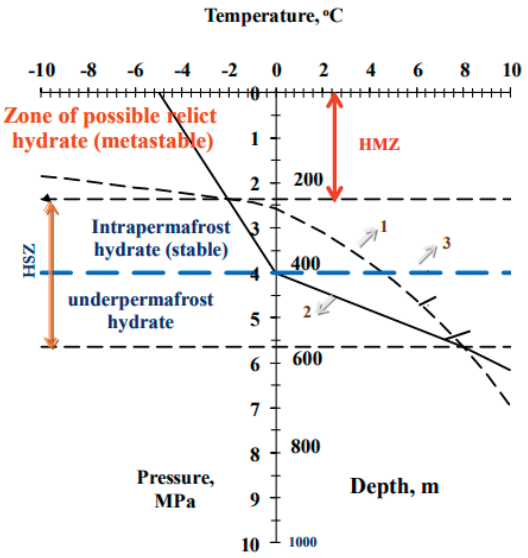

Fig. 2. Existence of methane hydrate in permafrost conditions [15]: 1- equilibrium curve of methane hydrate existence in water-gas medium; 2- curve of sediments temperature; 3- permafrost boundary; HSZ – hydrate stability zone; HMZ – hydrate metastability zone

Obviously, gas hydrates cannot be formed in the metastability zone, but they can exist there in a relict state for a long geological time provided that ice is preserved in the section, and there is no external influence [15]. Drilling of exploratory or production well in the gas hydrate distribution area can primarily destabilize gas hydrates in the metastability zone. The destabilization of gas hydrate formations during well drilling can occur as a result of mechanical stress (heating during the drilling bit rotation), as well as directly during the penetration of the drilling fluid (the impact of the chemical components of the drilling fluid, the change in the permeability of the surrounding rocks, the thermal effect, the pressure change as a result of injection).

IV. DRILLING FLUIDS AND THEIR INTERACTION WITH FROZEN AND HYDRATE SATURATED SEDIMENTS

Drilling mud is a fluid circulating throughout a well with the main purpose of carrying drill cuttings to the surface during drilling. Usually, this is a multicomponent dispersed system, consisting mainly of a mixture of water, clay, a weighting agent (for example, barite, siderite, etc.) and various chemicals. The following types of drilling fluids are distinguished [9], [19]:

- water-based;
- hydrocarbon-based;
- gaseous.

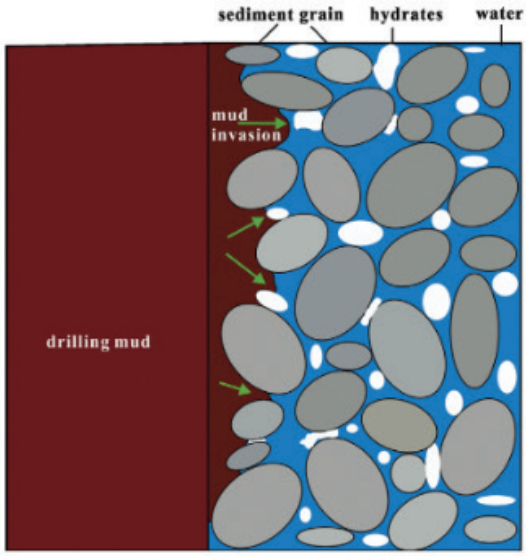

Fig. 3. The scheme of penetration of the water-based drilling fluid into the reservoir and the decomposition of gas hydrates [24], [27]

Water-based drilling fluids are most commonly used in well construction. Among them, there are drilling fluids on fresh or sea water, polymer non-dispersive, inhibitory and physiological fluids. Under permafrost conditions, polymer non-dispersive solutions with the addition of clay powder are currently used. Usually, they contain a solution of high molecular weight polymers such as polysaccharides and acrylates, as well as a weighting agent [11].

However, some time ago, sodium chloride inhibiting drilling fluids were also widely used in the zone of permafrost distribution. In this case, the salt concentration in the drilling fluid was calculated based on the freezing temperature of the solution so that the solution remained in a liquid state [19]. It has been demonstrated that such drilling fluids cause destabilization of gas hydrate formations [20].

Many authors describe the processes of gas emission as a result of the drilling mud penetration into the hydrate-containing formation. In [21]-[23] an active methane emission was observed in volumes exceeding the potential volumes of deep gas. Excessive emission was registered when warm drilling fluid was used for drilling in the permafrost zone. As a result, caverns were formed in the frozen rocks. However, with cold drilling fluid this phenomenon was practically not observed.

Ning with co-authors [23] explain the interaction of the drilling fluid with underpermafrost hydrate saturated sediments as follows (Fig. 3). Drilling fluid penetrating into the sediment changes the characteristics of the reservoir (permeability, mechanical properties, water content, chemical composition), and increases the temperature of the deposits causing active decomposition of gas hydrate formations. At the same time, the dissociation of gas hydrate is an endothermic process, i.e. it proceeds with the absorption of heat. Moreover, circulation of the drilling fluid causes an increase in pressure. Both a decrease in temperature and an increase in pressure lead to the secondary formation of hydrates in the near-well zone. The authors argue that the secondary hydrate saturation will be even higher than the initial saturation, and therefore there will be an even greater danger of hydrate destabilization [24]-[26].

At the moment, the question remains open on a direct assessment of the effect of the currently used non-dispersible polymer drilling fluid on the stability of gas hydrates, and even more on the impact of drilling fluids on intrapermafrost hydrates, where there is also an ice component. There are no experimental studies devoted to this problem; there are a few works based on mathematical modeling and they only mention the possible influence of the drilling fluid on the stability of gas hydrate saturated sediment based on indirect signs (gas emission, ejection of drilling mud, sand, etc.) [28], [29]. Also, a large number of works is devoted to the inhibition of gas hydrates by using drilling fluids of a certain composition (while most of these publications consider such inhibition in wells, not in the reservoirs) [30], [31].

V. RECOMMENDATIONS FOR WELL DRILLING THROUGH HYDRATE SATURATED FROZEN SEDIMENTS

Warm drilling fluid penetrating into hydrate-saturated rocks causes thawing of frozen sediments and decomposition of gas hydrates. This results in methane emission, accompanied by changes in sediment mechanical properties, which may lead to instability of the wellhead, its displacement or even collapse [23], [24], [32]-[34].

In this regard, there is a need to develop an algorithm of actions to prevent negative consequences.

Based on field data and experimental studies, two types of methods were proposed [7], [35]:
1. prevention of possible hydrate decomposition;
2. in situ hydrate decomposition before drilling.

The choice of method is determined by the actual geocryological and engineering-geological situation in the area, hydrate saturation of the formation, and the purpose of the well under construction. At the same time, each stage of work on the well should be accompanied by a certain set of measures against complications [35]-[37].

To prevent hydrate decomposition, it is necessary to use water-based drilling fluids cooled to +1...+4 °C, or hydrocarbon-based drilling fluids with a temperature below 0°C. Drilling should be carried out at the highest possible speed, with constant monitoring of the gas content in the drilling fluid. From a depth of approximately 200 m in the interval of the permafrost zone, appropriate adjustment of the density and temperature of the drilling fluid can be applied to prevent gas hydrate decomposition in the bottom hole zone [24], [35], [38].

Yakushev and Istomin [35] proposed to operate wells in two modes to maintain the stability of gas hydrate formations in frozen rocks: 1) cyclically (with periods of well preservation to control the thawing halo and critical changes in thermobaric conditions) and 2) with artificial cooling of casing [35]. However, to date, the most widely used method is drilling fluid pre-cooling using special installations located on the surface near the well [39], [40].

Srungavarapu with co-authors [29] conducted experimental studies of drilling fluids of various compositions in order to develop the most suitable ratio of drilling mud components to prevent decomposition of gas hydrates in order to reduce risks during field development. However, as a result, a drilling fluid inhibiting gas hydrate, rather than preventing hydrate decomposition was developed [29].

In the case of preliminary decomposition of hydrates, well drilling is carried out in accordance with the typically used technology in the northern fields. Wells constructed in this way can be operated continuously, but it is necessary to control the occurrence of gas emissions near the mouth and to regulate the flow rate of the drilling fluid [26], [35]. Any composition of drilling fluid can be used when applying this mode, preferably with mud preliminary heating and inhibitory components to enhance the decomposition of hydrate formation [35], [41]. However, in this case, the authors do not take into account the formation of a thawing halo in the near-wellbore area of frozen sediments and an approximate assessment of possible consequences.

Most of the works on inhibitory components are devoted to the prevention of hydrate formation inside the well, in the drilling fluid, rather than to a preliminary decomposition of gas hydrate formations in the reservoir. In the well activation of the hydrate formation process can occur as a result of the following three factors: increased pressure during drilling, the presence of low-temperature rocks, and high gas saturation of the rocks. To prevent this process, special chemical additives (hydrate inhibitors) have been developed [42]-[44]. However, inhibitors can also be used to dissociate hydrates before the well construction process to prevent possible hazards.

The advantages of the method of preliminary dissociation of gas hydrate formation are the simplicity of the technology and the possibility of continuous well drilling. In addition, it is possible to extract methane from hydrate saturated rocks for local energy supply. However, there are some disadvantages. These include the impossibility of using this technology in formations with a high degree of hydrate saturation, the formation of caverns, difficulties with subsequent cementation, and, most importantly, the danger of wellhead gas emission as a result of thawing of the surrounding rocks while drilling. Considering that hydrate saturation within one formation can vary dramatically, the thawing of rocks can contribute to the formation of griffins around the wellhead and associated complications. The disadvantages of this method also include environmental problems arising from its application. This is the subsidence of the surface around the mouth, the possibility of developing rapid processes of thermokarst and thermoerosion in areas adjacent to the well [26], [35], [42], [43].

Thus, the most acceptable method of well drilling in permafrost areas should be related to maintaining frozen and hydrate-saturated rocks in an undisturbed state, and in the case of high hydrate saturation of sediments this should be the only possible option. It is also necessary to mention the relative environmental safety of this method of well construction since its application has practically no effect on the surrounding geological environment.

VI. CONCLUSION

Drilling of exploration and production wells in the Arctic region is connected with a number of difficulties, primarily associated with the presence of frozen and hydrate saturated rocks. As a result of the drilling fluid contact with frozen hydrate saturated rocks, gas hydrate destabilization can occur. Large volumes of methane could be released as a consequence of changes in thermobaric conditions and/or under the influence of the chemical components of the drilling mud. In this regard, the issues of choosing the drilling fluid composition and the drilling mode are of particular importance.

The composition of the drilling fluid, as well as the drilling mode, should be selected in accordance with the stability conditions for gas hydrate formations for each particular area and their location in the reservoir, i.e., metastable (relic) hydrates, intra- and underpermafrost hydrate. In the area of permafrost distribution, two drilling methods can be chosen for exploratory and production wells: with the preservation of hydrates in the sediment or with their preliminary dissociation, before the construction of the well begins. Based on the analysis of the literature, it can be concluded that the method of drilling a well while preserving gas hydrate formations both in intrapermafrost and underpermafrost conditions is a more environmentally friendly and cost-effective way. This method implies the use of a low-temperature hydrocarbon-based drilling fluid. In this case, the effect on both gas hydrate formations and permafrost is minimized.

VII. REFERENCES

[1] N. G. Timofeev, R. M. Skryabin, and R. A. Atlasov, "Wells Drilling Temperature Regime under the Cryolithozone Conditions" (published in Russian), Sci. Educ., no. 3, pp. 51–56, 2017.

[2] B. Kudryashov and A. Yakovlev, Well Drilling in Permafrost (published in Russian). Nedra: Moscow, Russia, 1983.

[3] R. I. Medevedevsky, Gas and Oil Well Building and Exploitation in Permafrost (published in Russian). Nedra: Moscow, Russia, 1987.

[4] S. M. Lu, "A global survey of gas hydrate development and reserves: Specifically in the marine field," Renew. Sustain. Energy Rev., vol. 41, pp. 884–900, 2015.

[5] J. N. Nimblett, R. C. Shipp, and F. Strijbos, "Gas hydrate as a drilling hazard: Examples from global deepwater settings," in Proceedings of the Annual Offshore Technology Conference, 2005, vol. 2005-May, pp. 1429–1435.

[6] V. S. Yakushev and V. A. Istomin, "Causes of gas emissions in frozen rocks of the Yamburg gas condensate field (published in Russian)," in Features of Gas Well Development in Difficult Geocryological Conditions, VNII-Gas: Moscow, Russia, 1987, pp. 119–127.

[7] V. S. Yakushev and T. S. Collett, "Gas hydrates in arctic regions: risk to drilling and production," in Proceedings of the Second International Offshore and Polar Engineering Conference, 1992, vol. 1, pp. 669–673.

[8] Y. Ma, J. Yang, P. Feng, and C. Zhang, "The challenges and key technology of drilling safety in the area of the arctic," in Proceedings of the International Field Exploration and Development Conference 2018, Springer Series in Geomechanics and Geoengineering, Springer: Berlin, 2020, pp. 522–532.

[9] P. L. Moore, Drilling Practices Manual. Second edition, Pennwell Books, Tulsa, USA, 1986.

[10] A. A. Iakovlev, M. V. Turitsyna, and E. V. Mogil'nikov, "Analysis and justification of selecting cleaning agents and technology of their application in permafrost well drilling" (published in Russian), Bull. PNIPU. Geol. Oil gas Min., vol. 12, pp. 22–32, 2014.

[11] V. K. Chistyakov, D. V. Leonova, and N. A. Vishnevsky, "Justification of the composition and properties of drilling fluid for exploratory drilling for gas hydrates" (published in Russian), Miner. Explor. Prot., no. 1, pp. 60–63, 2012.

[12] E. D. Sloan, Clathrate Hydrates of Natural Gases. Second Edition, Revised and Expanded, New York, USA: CRC Press, 1998.

[13] V. A. Istomin and V. S. Yakushev, Gas Hydrates in Nature (Published in Russian). Nedra: Moscow, Russia, 1992.

[14] T. S. Collett, S. R. Dallimore, and M. D. Max, "Permafrost-associated gas hydrate," in Natural gas hydrate in oceanic and permafrost environments, Springer Series in Coastal Systems and Continental Margins, Springer: Berlin: 2003, pp. 43–60.

[15] E. Chuvilin, B. Bukhanov, D. Davletshina, S. Grebenkin, and V. Istomin, "Dissociation and Self-Preservation of Gas Hydrates in Permafrost," Geosciences, vol. 8, no. 12, pp. 431:1-431:12, 2018.

[16] Hydrafact, "HydraFlash." Edinburg, UK.

[17] E. D. Ershov, Y. P. Lebedenko, E. M. Chuvilin, V. A. Istomin, and V. S. Yakushev, "Features of the existence of gas hydrates in the cryolithozone" (published in Russian), Rep. Acad. Sci. USSR, vol. 321, pp. 788–791, 1991.

[18] V. Istomin, V. Yakushev, and N. Makhonina, "Self-preservation phenomenon of gas hydrate" (published in Russian), Gas Ind., pp. 36–46, 2006.

[19] A. I. Bulatov and A. I. Penkov, Well Flushing Handbook (Published in Russian), Nedra: Moscow, Russia, 1984.

[20] E. Chuvilin, V. Ekimova, B. Bukhanov, S. Grebenkin, N. Shakhova, and I. Semiletov, "Role of Salt Migration in Destabilization of Intra Permafrost Hydrates in the Arctic shelf: Experimental Modeling," Geosciences, vol. 9, no. 4, p. 188, 2019.

[21] V. P. Yakutseni, "Gas hydrates - unconventional gas raw materials, their formation, properties, distribution and geological resources (published in Russian)," Oil gas Geol. Theory Pract., vol. 8, no. 4, 2013.

[22] Ş. Merey, "Drilling of gas hydrate reservoirs," J. Nat. Gas Sci. Eng., vol. 35, no. Part A. pp. 1167–1179, 2016.

[23] F. Ning et al., "Invasion of drilling mud into gas-hydrate-bearing sediments. part i: Effect of drilling mud properties," Geophys. J. Int., vol. 193, no. 3, pp. 1370–1384, 2013.

[24] L. Chen, S. Wang, and C. Ye, "Effect of gas hydrate drilling fluids using low solid phase mud system in plateau permafrost," Procedia Engineering, vol. 73, pp. 318–325, 2014.

[25] T. Huang, Y. Zhang, G. Li, X. Li, and Z. Chen, "Numerical modeling for drilling fluid invasion into hydrate-bearing sediments and effects of permeability," J. Nat. Gas Sci. Eng., vol. 77, 103239, 2020.

[26] M. Zheng, T. Liu, G. Jiang, M. Wei, Y. Huo, and L. Liu, "Large-scale and high-similarity experimental study of the effect of drilling fluid penetration on physical properties of gas hydrate-bearing sediments in the Gulf of Mexico," J. Pet. Sci. Eng., vol. 187, 106832, 2020.

[27] J. Sun et al., "The effect of drilling mud properties on shallow lateral resistivity logging of gas hydrate bearing sediments," J. Pet. Sci. Eng., vol. 127, pp.259-269, 2015.

[28] A. Fereidounpour and A. Vatani, "An investigation of interaction of drilling fluids with gas hydrates indrilling hydrate bearing sediments," J. Nat. Gas Sci. Eng., vol. 20, pp. 422–427, 2014.

[29] M. Srungavarapu, K. K. Patidar, A. K. Pathak, and A. Mandal, "Performance studies of water-based drilling fluid for drilling through hydrate bearing sediments," Appl. Clay Sci., vol.152, pp.211-220, 2018.

[30] J. W. Barker and R. K. Gomez, «Formation of hydrates during deepwater drilling operations,» J. Petrol. Technol., vol. 41, no. 3. 1989.

[31] M. A. Kelland, K. Mønig, J. E. Iversen, and K. Lekvam, "Feasibility study for the use of kinetic hydrate inhibitors in deep-water drilling fluids," Energy and Fuels, vol. 22, no. 4, pp. 2405–2410, 2008.

[32] G. Jiang et al., "Polyethylene glycol drilling fluid for drilling in marine gas hydrates-bearing sediments: An experimental study," Energies, vol. 4, no. 1, pp. 140–150, 2011.

[33] A. Fereidounpour and A. Vatani, "Designing a Polyacrylate drilling fluid system to improve wellbore stability in hydrate bearing sediments," J. Nat. Gas Sci. Eng., vol. 26, pp.921–926, 2015.

[34] G. Moridis et al., "Challenges, Uncertainties, and Issues Facing Gas Production From Gas-Hydrate Deposits," SPE Reserv. Eval. Eng., vol. 14, no. 1, pp. 76–112, 2011.

[35] V. S. Yakushev, V. A. Istomin, and N. R. Kolushev, Guidelines on the Features of the Construction and Operation of Eells in Frozen and Thawed Rocks Containing Gas Hydrates. (Published in Russian). Ministry of the Gas Industry, VNIIGAZ, NPO SOYUZGAZTEKHNOLOGIYA: Moscow, Russia, 1989.

[36] R. D. Roadifer, S. P. Godbole, and V. A. Kamath, "Thermal model for establishing guidelines for drilling in the arctic in the presence of hydrates," in Society of Petroleum Engineers - SPE California Regional Meeting, CRM 1987, 1987, pp. 367–378.

[37] D. R. McConnell, Z. Zhang, and R. Boswell, "Review of progress in evaluating gas hydrate drilling hazards," Mar. Pet. Geol., vol. 34, no. 1, pp. 209–223, 2012.

[38] V. S. Yakushev and V. A. Istomin, "Features of the construction and operation of wells in hydrated rocks (published in Russian)," in Development of Gas Condensate Fields, Section 2: Opening and Fixing of Gas Condensate Wells, May 29-June 2, 1990.

[39] C. Chen, C. Da-yong, and F. Xue-wei, "Application of Mud Cooling System for Gas Hydrate Exploration in Permafrost," Sci. Rep. Don NTU. Ser. Rock. Geol., vol. 14, no. 181, pp.97–101, 2011.

[40] K. U. Heeschen, S. Abendroth, M. Priegnitz, E. Spangenberg, J. Thaler, and J. M. Schicks, "Gas Production from Methane Hydrate: A Laboratory Simulation of the Multistage Depressurization Test in Mallik, Northwest Territories, Canada," Energy and Fuels, vol. 30, no. 8, pp. 6210–6219, 2016.

[41] S. M. Golmohammadi and A. Nakhaee, "A cylindrical model for hydrate dissociation near wellbore during drilling operations," J. Nat. Gas Sci. Eng., vol. 27, pp. 1641–1648, 2015.

[42] T. S. Kotkoskie, B. Al-Ubaldi, T. R. Wildeman, and E. D. Sloan, "Inhibition of gas hydrates in water-based drilling muds," SPE Repr. Ser., vol. 7, no. 2, 1992.

[43] W. Halliday, D. K. Clapper, and M. Smalling, "New gas hydrate inhibitors for deepwater drilling fluids," in Proceedings of the IADC/SPE Asia Pacific Drilling Technology Conference, APDT, 1998, pp. 201–211.

[44] Q. Chu, J. Su, and L. Lin, "Inhibition performance of amidocyanogen silanol in water-based drilling fluid," Appl. Clay Sci., vol. 185, 105315, 2020.

An Overview of Distributed Methods for Power System State Estimation

S. Asefi, S. Parsegov, and E. Gryazina

Abstract **Power System State Estimation (PSSE) is a key function in building adequate network models for real-time monitoring and analysis. Therefore, PSSE has been a research area of interest for power engineers for a long period of time. Due to the intermittent nature of renewable energy sources, intensively utilized in the power network, the importance of state estimation has increased as well. The complexity and the growing size of the networks may lead to problems with centralized state estimation such as communication bottleneck in real-time analyzing of the system or reliability issues. Distributed state estimation is a solution for the mentioned issues. There are different implementation methods introduced for it. This paper presents a brief review of the recent approaches to distributed PSSE problem, according to the most important factors like iteration number, convergence rate, data needed to be transferred to/from each area and so on. Finally, a comparison between the total efficiency of all applied methods is made.**

Index Terms **Distributed State Estimation; Optimization; Power System**

I. INTRODUCTION

STATE estimation (SE) is an essential part of the current power systems. The major benefits of state estimation are estimation of network parameters based on redundancy in measurements, bad data and topology errors detection, estimating meter measurements for missing or delayed data [1]. Advance state estimation can improve monitoring and control of the power system in the case of contingency occurring. Providing reliable and complete information is the main duty of the state estimator, which has a great importance for online operations and control systems that guarantee security of the power grid [2]. In other words, the main function of the state estimator is to identify the system state by minimizing a specific criterion based on recent system measurements [3]. In addition, the increasing presence of renewable energy sources (RESs) in the power grid demands state estimation to be more precise and fast due to RESs intermittent nature.

Sajjad Asefi is with the Center for Energy Science and Technology, Skolkovo Institute of Science and Technology, Skolkovo Innovation Center, Building 3, Moscow, 121205, Russia. **sajjad.asefi@skoltech.ru**

Sergei Parsegov is with the Center for Energy Science and Technology, Skolkovo Institute of Science and Technology, Skolkovo Innovation Center, Building 3, Moscow, 121205, Russia. **S.Parsegov@skoltech.ru**

Elena Gryazina is with the Center for Energy Science and Technology, Skolkovo Institute of Science and Technology, Skolkovo Innovation Center, Building 3, Moscow, 121205, Russia. **E.Gryazina@skoltech.ru**

Power system state estimation problem has been a matter of concern back in 1970s, when Schweppe et al. [4]-[6] developed first model to solve this problem. Traditionally PSSE is done in a centralized manner, in which a single unit collects all data ('data' here refers to measurement unit data and system parameters such as line impedance) of the system, and an optimization technique is used to solve the PSSE problem. Later on, not only for state estimation but also all optimization problems, distributed solutions attracted researchers' interest. Due to the increase in measurement units and computational demand for growing power networks, there has been a need to apply distributed state estimation to speed up the processing time by spreading the computational tasks among different control units. On the other hand, power systems are increasingly interconnected and the trend for interconnection of systems is expected to continue in the future smart grid. There have been plenty of investigations about distributed state estimation in literature.

In [7], a simple yet general multi-area decentralized state estimation method is described, which can provide a correct estimation of the system states. While the system is in connection with other systems, they only interchange a small amount of border data without any need for data to be processed or manipulated. Authors of [8]-[9] have provided a novel algorithm for distributed state estimation using alternating direction method of multipliers (ADMM). As stated by the authors, besides applying conventional least squares state estimation, the proposed decentralized process constructs a robust state estimator. In [10] and [11] a distributed state estimation using matrix splitting method is presented. First, in [10] authors evaluated the method for DC state estimation, but later in [11] they provided a distributed Gauss-Newton method for AC state estimation. It is to be noted that both papers have considered PMU (phasor measurement units) measurements in addition to conventional SCADA (supervisory control and data acquisition) data. All the mentioned approaches are different in terms of applicability.

Interconnected power systems are managed by independent operators; each operator uses SE to estimate the state of the region of the interconnected system that it controls. Examples of interconnected power systems are the Western Interconnect in the U.S., and the ENTSO-E in Europe [12]. Additionally, decentralization decreases the possibility of a communication bottleneck, which is more probable to happen in a huge system during centralized state estimation [13]. In some cases, due to data privacy and cyber security reasons, the state estimation must be decentralized, e.g., when areas ('area' here refers to a partition of the power system) are different countries. Utilizing distributed topology of power system, after specification of different areas, based on specifying overlapping (neighboring) buses in each area and considering power flow equations, one can find the solution using distributed methods provided in the literature, see e.g. [11], [14].

We have examined different methods mentioned above as well as mathematical solvers to IEEE 14-bus standard test system, and compared the performance of these methods from different points of view, such as the data needed to be transferred or computation time, error of obtained solution compared to centralized one and convergence rate, are compared. The purpose of the paper is to present brief review and comparison of distribute methods in terms of communication burden (the data needed to be transferred to/from each area) and iteration number to get a reasonable solution.

The paper is organized as follows. In section II, the problem formulation is provided. Section III shows the results of the applied methods on the test system. And finally, in section IV the conclusion of this research paper is presented.

II. PROBLEM FORMULATION

The type of PSSE considered in this research is Static SE. Static SE is used to monitor the system during normal operation, in quasi-steady state responding to slowly varying network load and generation. Given the network model, all measurement types, such as power flows, power injections, virtual measurements (based on physical assumption of the system, like zero net power injection at buses with no load or generation) and pseudo measurements (i.e. values that are predicted based on historical data) can be expressed as a function of the system states. It is to be noted that state variables refer to phase angles. The formulation of the SE problem is based on the concept of maximum likelihood estimation [2].

One can write the maximum likelihood equation in general or matrix format:

$$\min J(x) = \min[z - h(x)]^T \times R^{-1} \times [z - h(x)], \quad (1)$$

where R is a covariance matrix, z is the measurements matrix and h(x) is a function that shows the relation between measurements and state variables. In order to solve this optimization problem, the solution must pursue first order optimality condition:

$$\partial J/\partial x = 0 \rightarrow [\partial J/\partial x]^T \times R^{-1} \times [z - h(x)],$$

$$H(x) = \partial h/\partial x \text{ is the Jacobian matrix of } h(x). \quad (2)$$

There are two points of view on the problem. One is DC SE, in which the h(x) is a linear function (that means measurements have linear relation with state variables) and we can do the matrix calculation directly. The other one is AC SE, in which h(x) is nonlinear and we must use other methods like Newton, Gauss-Newton, etc., to solve it.

This paper deals with only DC SE. As stated before, if we consider a linear relation between measurement units and state variables ($h(x) = H \times x$, where H indicates the measurement matrix and x represents all voltage phase angles θ of the power system buses), the solution to (1) can be obtained in a single step as follows, meeting the first order optimality condition:

$$(H^T R^{-1} H)x = H^T R^{-1} z, \quad (3\text{-a})$$

$$x^* = (H^T R^{-1} H)^{-1} \times H^T R^{-1} z. \quad (3\text{-b})$$

In order to calculate (3) we need to access all data in the system by a single (or centralized) control unit. As mentioned before, issues like the increase in the number of measurement units in the power system, communication bottlenecks and data security are the main reasons that lead power system to utilize decentralized approaches. Further, a brief overview of the known approaches to the recent distributed power system state estimation is provided.

A. Matrix splitting (I)

In order to solve problem (1) in a distributed manner, one can use matrix splitting method and after a certain number of iterations the answer converges to the centralized solution. The main equation of matrix splitting for a problem of $Ax = y$ is:

$$x^{t+1} = M^{-1} Nx^t + M^{-1} y. \quad (4)$$

A is written as the sum of an invertible (or diagonal) matrix M, and a matrix N; i.e. $A = D + E$, or $A = M + N$ so that $M = D + E'_{ii}$ and $N = E - E'_{ii}$. Note that D contains diagonal arrays and E contains off-diagonal arrays of matrix A. And E'_{ii} is a diagonal matrix which is defined as follows:

$$E'_{ii} = \alpha \times \sum_{j=1}^{n} |E_{ij}|, \quad (5)$$

with $\alpha = 1$ assumed for simplicity. It is to be noted that (4) converges if the spectral radius of $M^{-1}N$ matrix be less than 1 ($\rho(M^{-1}N) < 1$). Using (4) iteratively results in convergence to the system's ($Ax = y$) final solution (x^*).

B. Matrix splitting (II)

In this section, we are going to introduce another matrix splitting approach, which is discussed in [15]. The authors considered measurement units in an asynchronous manner, and the results show that many iterations are needed to get a reasonable convergence. However, we consider only synchronous manner of measurement units is considered. Now, let us briefly describe how the method works.

In DC model, the state estimation problem in the least squares setting can be formulated as (1) and (3). Based on what has been stated in (3), this problem has a closed-form solution. Let's assume, $L = H^T R^{-1} H$ and $\upsilon = H^T R^{-1} z$. One way to compute this solution x* is through the gradient based iterative algorithm:

$$x(k+1)=(I-\tau L)x(k) + \tau\upsilon. \tag{6}$$

The parameter τ is selected from the interval $(0, 2||L||^{-1})$; such a τ guarantees the matrix $I - \tau L$ to be Schur stable (i.e. the iterative method converges).

C. Power flow-based method

In this section we are going to discuss the method provided in [7]. This method applies simple power flow and power injection equations. Based on what have been stated in literature, it is clear that the single-area (general) state estimation problem and multi-area state estimation problem can be formulated as follows for DC state estimation:

$$\min_{x_a} J_a(x_a) + \sum_{b \in \Omega_a} J_{ab}(x_a, \tilde{x}_b), \tag{7-a}$$

$$J_a(x_a) = \sum_{b \in \Omega_a^P} \omega_{a,i}^P - P_{a,i}^m - P_{a,i}(.))^2$$

$$+ \sum_{(i,j)\in \Omega_a^{PF}} \omega_{a,ij}^{PF} (P_{a,ij}^m - P_{a,ij}(.))^2, \tag{7-b}$$

$$J_{ab}(x_a,\tilde{x}_b) = \sum_{i \in \Omega_{ab}^P} \omega_{ab,i}^P (P_{ab,i}^m - P_{ab,i}(.))^2 \tag{7-b}$$

$$+ \sum_{(i,j) \in \Omega_{ab}^{PF})} \omega_{ab,ij}^{PF} (P_{ab,ij}^m - P_{ab,ij}(.))^2$$

$$+ \sum_{i \in \Omega_{ab}} \omega_{b,i}^x (\tilde{x}_{b,i} - x_{b,i})^2, \tag{7-c}$$

where $J_a(.)$ is weighted measurement error function for area a involving only state variables of area a; J_{ab} is weighted measurement error function for area a involving state variables of area a and b; and Ω_a is the set containing indices for all neighboring areas of area a; ω is weighting factor; $P_{(.),i}^{(.)}$ is active power injection at bus i; + $P_{(.),i,j}^{(.)}$, is power flow in between bus i and j; and m indicates measurement. More detailed explanation can be found in [7]. To solve (7), we applied Matlab solver (Sequential quadratic programming (SQP)) and the results are provided in this paper.

D. ADMM

In [8] a new method was developed for solving distributed PSSE, which is based on ADMM presented in [16]. As claimed by the authors, ADMM increases existing PSSE solvers performance, and convergence of the method to its centralized counterpart is guaranteed, even if we don't have local observability. In general, the decentralized state estimation problem can be formulated as:

$$\min_{xk} \sum_{k=1}^{K} f_k(x_k), \tag{8-a}$$

$$x_k[l] = x_l[k], \ \forall l \in N_k, \forall k, \tag{8-b}$$

where N_k is the set of areas sharing states with area k and $x_{k,l}$ is auxiliary variable introduced per pair of interacting areas k, l.

The constraint forces neighboring areas to consent on their shared variables. Augmented Lagrangian function is as follows:

$$L(\{x_k\}, \{x_{kl}\};\{v_{kl}\})$$

$$:= \sum_{k=1}^{K} [f_k(x_k) + \sum_{l\in N_k}^{K} (v_{k,l}^T (x_{k[l]} - x_{kl}) + c/2 \ ||x_{k[l]} - x_{kl}||_2^2), \tag{9}$$

where $v_{k,l}$ is Lagrangian multiplier and $c > 0$,

$$\{x_k^{(t+1)}\} := \arg\min L(\{x_k\},\{x_{kl}^t\};\{v_{kl}^t\}), \tag{10-a}$$

$$\{x_{kl}^{t+1}\} := \arg\min L(\{x_k^{t+1}\},\{x_{kl}\};\{v_{kl}^t\}), \tag{10-b}$$

$$v_{kl}^{t+1} := v_{kl}^t + c(x_{k[l]}^{t+1} - x_{kl}^{t+1}),\ \forall k \tag{10-c}$$

Let's consider a system which is divided into k areas. Each area collects M_k measurements

$$z_k = H_k\, x_k + e_k, \tag{11}$$

so that x_k contains system states and e_k is random noise vector.

III. RESULTS AND DISCUSSION

In this section, we apply all methods to IEEE 14-bus system, which is the most analyzed system in the literature, and compare the results. Please note that figures 1 to 8 present a comparison of the methods and the convergence curve for vector of variables (**x** is state vector and **t** indicates iteration number). Table 1 summarizes the numerical results related to the number of iterations of different methods, error values compared to centralized solution, computational burden, overall elapsed time and finally the objective function value. Convergence limit ε was set to 10^{-6} for all cases. Two different scales were applied for measuring the error of each method's solution compared to the answer obtained using the centralized method. E_1 is the sum of absolute values of difference between centralized and decentralized solutions (i.e. $\sum|x_{cent} - x_{decent}|$), and E_2 is $\max(|x_{cent} - x_{decent}|)$. Computation time means the time has been spent by computer to solve the problem in a distributed manner. As stated in [17], time delay can be considered between 0.1 to 0.5 second. So, we selected data transmission delay of $t_{delay} = 0.5$ as the worst case. In other words, the overall time can be calculated using the following equation:

$$T_{Overall} = t_{delay} \times \text{iteration} + \text{Computation time}. \tag{12}$$

Finally, the objective function value for optimal state variables, which was obtained applying different methods, was evaluated using (1). In all methods, except the power flow-based method, as explained in previous sections, there is a parameter, which directly affects the behavior of the method's convergence. Considering mathematical criteria as well, we tried to select the best parameters.

TABLE I

Numerical results of IEEE 14 Bus system

Methods	**Iteration**	**E_1**	**E_2**	**Computation burden [s]**	**Overall time [s]**	**Objective value**
Matrix splitting (I)	1024	1.26e-3	1.31e-4	8.4546	529.45	10.0565
Matrix splitting (II)	2217	2.59e-3	3.15e-4	0.56	1109.06	10.0689
Power flow based	40	5.61e-4	5.61e-4	2.83	22.83	10.5615
ADMM	245	2.43e-3	2.43e-3	0.4282	122.93	12.036

It is to be noted that system data and area specification for 14-bus system is adapted from [14]. Figures show results for matrix splitting (I), matrix splitting (II), power flow-based and ADMM methods, respectively. The centralized objective value for 14-bus system using (1) and (3) is 10.0524. In the case of matrix splitting (II) or ADMM method (i.e. see Fig. 4 and 8), it is notable that one of the states (or variables) passes the convergence criterion due to the high deviation in the beginning steps of the process. In order to avoid this problem stopping criterion has been considered after a certain number of iterations, based on system size (e.g. for 14-bus system applying matrix splitting (II) it will be considered after 300th iteration).

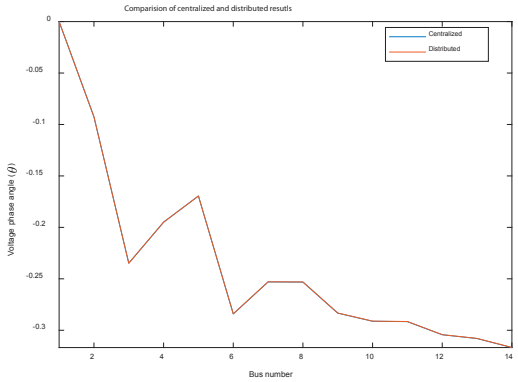

Fig. 1. Comparison of centralized and decentralized voltage phase angle (in radian) using matrix splitting (I) for 14 bus DC system

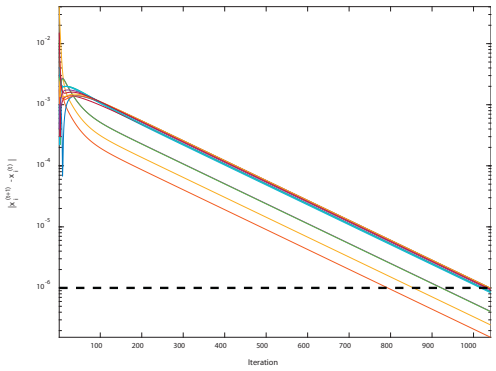

Fig. 2. Convergence curve for vector of variables using matrix splitting (I) for 14 bus DC system (each line shows the convergence process of a variable)

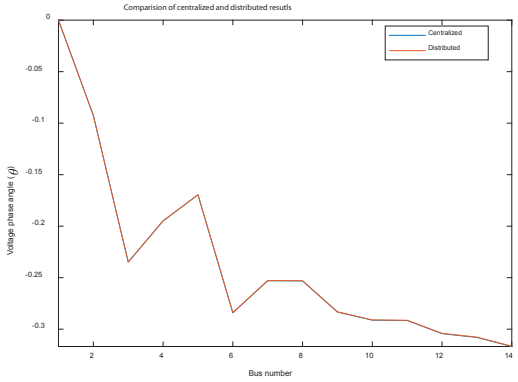

Fig. 3. Comparison of centralized and decentralized voltage phase angle (in radian) using matrix splitting (II) for 14 bus DC system

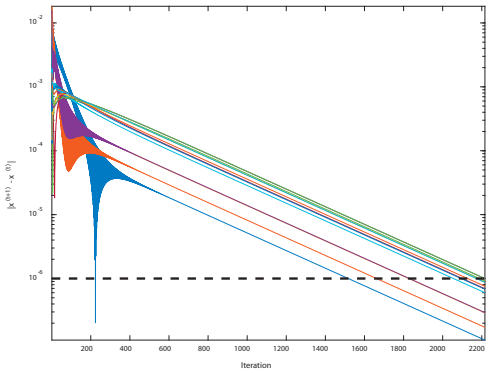

Fig. 4. Convergence curve for vector of variables using matrix splitting (II) for 14 bus DC system

Another essential issue is the amount of data needed to be transmitted for each method. Both matrix splitting methods need 2-hop (or neighbor of neighbor, check [10] for detailed definition), when there is a power injection in the neighboring node, which may cause requesting more data from the neighboring areas in breach of the privacy and security considerations. In contrast, the other two methods do not require such a data.

IV. CONCLUSION

In this paper, we provided a brief detailed overview of recent decentralized (or distributed) methods for PSSE. Considering obtained numerical results and demonstrated figures for IEEE 14-bus system, the application of decentralized method will show the same results as the centralized method. If we increase the delay time, the number of iteration will play a vital role in overall consumed time, but if we decrease it (to milliseconds), the number of iterations can be negligible as well. In the case of minimum data transfer and considering consumed time, power flow-based and ADMM methods are good choices, or in the case of more accurate objective value for small systems, matrix splitting (I) is good. The power flow-based method has less

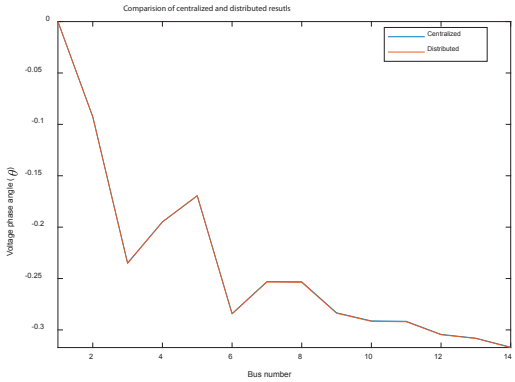

Fig. 5. Comparison of centralized and decentralized voltage phase angle (in radian) using power flow-based method for 14 bus DC system

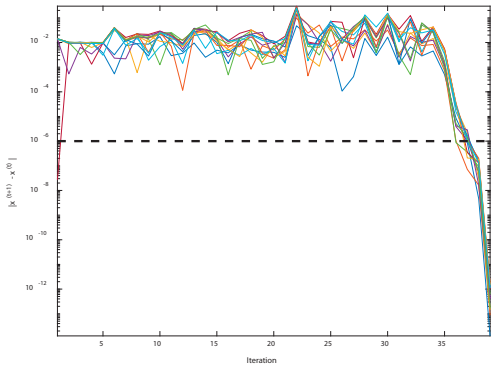

Fig. 6. Convergence curve for vector of variables using power flow-based method for 14 bus DC system

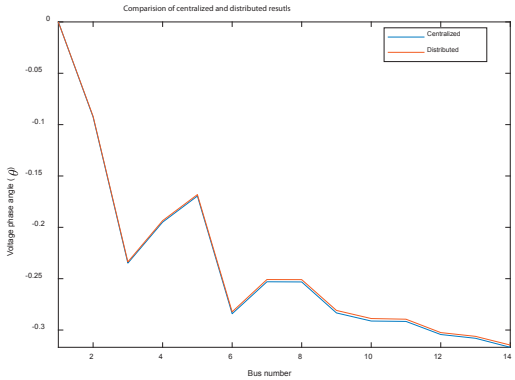

Fig. 7. Comparison of centralized and decentralized voltage phase angle (in radian) using ADMM for 14 bus DC system

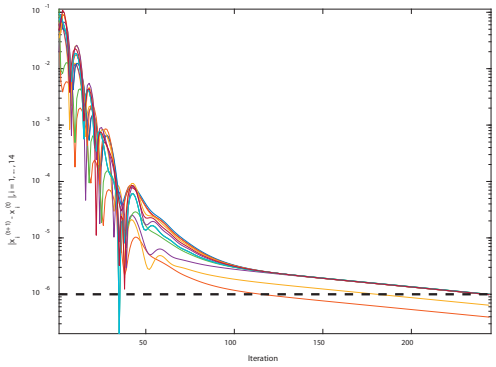

Fig. 8. Convergence curve for vector of variables using ADMM for 14 bus DC system

iteration number. Considering this fact, one may select the power flow based method as the best one, but this method needs a solver for finding the best solution, which there is no guarantee to reach to the best solution. Overall, making a final decision about the best method is not an easy task and is highly dependent on the need of the power utility.

Applying methods to high dimension test systems and making a comparison from a cyber-security point of view are directions for future research.

V. REFERENCES

[1] J. Wood, B. F. Wollenberg, and G. B. Sheblé, "Power generation, operation, and control," John Wiley & Sons, 2013.

[2] A. Gomez-Exposito, A. J. Conejo, and C. Canizares, "Electric energy systems: analysis and operation," CRC press, 2018.

[3] F. Ahmad, A. Rasool, E. Ozsoy, R. Sekar, A. Sabanovic, and M. Elitas, "Distribution system state estimation-a step towards smart grid," Renew-able and Sustainable Energy Reviews, vol. 81, pp. 2659–2671, 2018.

[4] F. C. Schweppe, "Power system static-state estimation, part iii: Implementation," IEEE Transactions on Power Apparatus and Systems, no. 1, pp. 130–135, 1970.

[5] F. C. Schweppe and D. B. Rom, "Power system static-state estimation, part ii: Approximate model," IEEE Transactions on Power Apparatus and Systems, no. 1, pp. 125–130, 1970.

[6] F. C. Schweppe and J. Wildes, "Power system static-state estimation, part i: Exact model," IEEE Transactions on Power Apparatus and Systems, no. 1, pp. 120–125, 1970.

[7] A. J. Conejo, S. de la Torre, and M. Canas, "An optimization approach to multi-area state estimation," IEEE Transactions on Power Systems, vol. 22, no. 1, pp. 213–221, 2007.

[8] V. Kekatos and G. B. Giannakis, "Distributed robust power system state estimation," IEEE Transactions on Power Systems, vol. 28, no. 2, pp.1617–1626, 2013.

[9] V. Kekatos, E. Vlahos, D. Ampeliotis, G. B. Giannakis, and K. Berberidis, "A decentralized approach to generalized power system-state estimation," in 5th IEEE International Workshop on Computational Advances in Multi-Sensor Adaptive Processing (CAMSAP), pp. 77–80, 2013.

[10] A. Minot and N. Li, "A fully distributed state estimation using matrix splitting methods," in American Control Conference (ACC). IEEE, pp. 2488–2493, 2015.

[11] A. Minot, Y. M. Lu, and N. Li, "A distributed Gauss-Newton method for power system state estimation," IEEE Transactions on Power Systems, vol. 31, no. 5, pp. 3804–3815, 2016.

[12] V. Ognjen and G. Dán. "Security of fully distributed power system state estimation: Detection and mitigation of data integrity attacks," IEEE Journal on Selected Areas in Communications, vol. 32, no. 7, pp. 1500–1508, 2014.

[13] R, Zhengwei, Y. C., Shaowei Huang, M. Heleno, and Y. Xia. "A Fully Distributed Coordination Method for Fast Decoupled Multi-Region State Estimation," IEEE Access, vol. 7, pp. 132859–132870, 2019.

[14] V. Kekatos, G. Wang, H. Zhu, and G. B. Giannakis, "PSSE redux: Convex relaxation, decentralized, robust, and dynamic approaches," arXiv preprint arXiv:1708.03981, 2017.

[15] P. Frasca, H. Ishii, C. Ravazzi, and R. Tempo, "Distributed randomized algorithms for opinion formation, centrality computation and power systems estimation: A tutorial overview," European Journal of Control, vol. 24, pp. 2–13, 2015.

[16] S. Boyd and L. Vandenberghe, "Convex optimization," Cambridge university press, 2004.

[17] M. Glavic and T. Van Cutsem, "Tracking network state from combined SCADA and synchronized phasor measurements," in IREP Symposium Bulk Power System Dynamics and Control-IX Optimization, Security and Control of the Emerging Power Grid, pp. 1–10, 2013.

Focus

Magnetron Sputtering of Electron Transport Materials for Perovskite Photovoltaics

Artyom V. Novikov

Abstract

Perovskite solar cells (PSCs) are one of the most promising photovoltaic technologies. They offer the benefits of high power conversion efficiency, solution processability and the possibility of manufacturing flexible and stretchable solar cells. However, several significant problems, the major one being poor operational stability, prevent their large-scale commercialization. Therefore, a significant research effort is directed towards overcoming these problems. One of the ways to improve both the stability and efficiency of PSCs is rational engineering of charge-transport layers. Magnetron sputtering is a powerful method that can be used for this purpose. It allows the smooth and uniform deposition of a wide range of materials and provides means of fine-tuning their optical, electrical and structural properties. Moreover, this method is compatible with most of the industrial processes. In this paper a brief overview of the magnetron sputtering use in the design of electron transport layers for PSCs is presented.

Index Terms

Electron Transport Materials; Magnetron Sputtering; Perovskite Solar Cells

I. NOMENCLATURE

V_{oc}	open-circuit voltage (V)
J_{SC}	short-circuit current (mA/cm^2)
FF	fill factor (%)
PCE	power conversion efficiency (%)
CTL	charge transport layer
ETL	electron transport layer

A.V. Novikov is with the Center of Classical Materials, Skolkovo Institute of Science and Technology, Skolkovo Innovation Center, Building 3, Moscow, 121205, Russia. **Artyom.Novikov@skoltech.ru**

II. INTRODUCTION

PEROVSKITE solar cells recently revolutionized the field of photovoltaics. In less than 10 years from the first publication featuring this technology [1] they reached certified power conversion efficiency of more than 25% and now are rivaling the standard silicon-based solar cells [2]. They are also extremely attractive to industry because of the possibility to form high-quality perovskite films by solution processing. This, in turn, allows the use of flexible plastic substrates and the application of cost-effective roll-to-roll technology in the manufacturing of solar panels [3]. Moreover, all the precursors for the production of the photoactive materials used in PSCs are very cheap making the potential cost of generated electricity significantly lower than in the case of all other currently used technologies [4].

However, perovskite photovoltaics faces a number of significant challenges on its way to commercialization. The main among these challenges is the relatively low operational stability of PSCs. It was shown by several research groups that oxygen, humidity, elevated temperatures, electric field, and light-soaking can induce rapid degradation of complex lead halides used as light absorbers in PSCs [5]. And while lead-free absorbers present a widely discussed alternative, to date the success of such materials was very limited [6]. Therefore, the major research effort in the field is currently aimed at the enhancement of the stability of PSCs based on conventional lead-halides.

State-of-the art research indicates that the major perovskite degradation pathways include the formation of volatile byproducts such as molecular iodine, etc. [7]. Such species can leave the active layer, thus making the degradation process irreversible. However, the reactions that lead to the formation of volatiles can be potentially reversed in the absence of degradation factors if the volatiles are trapped inside the active layer.

This is the task where a rational design of charge transport layers (CTLs) and, more specifically, electron transport layers can be invaluable. A CTL featuring good charge extraction and transport properties paired with low gas permeability can increase the PSCs' lifetime significantly. And among other techniques employed for CTL, processing magnetron sputtering is one of the most promising because it allows the achievement of smooth and uniform surface morphology and precise control of such parameters as stoichiometry and presence of surface defects [8].

The field of perovskite photovoltaics is developing at an incredibly fast rate; therefore, a frequent review of the state-of-the-art achievements is required for a clear understanding of the current situation. In this article, a brief overview of the operating principles of perovskite photovoltaics and magnetron sputtering will be presented to form a background for further discussion. After that, the key results in the development of ETLs for PSCs using the sputtering technique will be highlighted. Finally, based on the reviewed information, the author will present his suggestions for future research in this area.

III. PEROVSKITE SOLAR CELLS OPERATING PRINCIPLE

As in all other photovoltaic technologies, in PSCs the current is generated upon the absorption of the light by the active layer. The energy of absorbed photons causes the excitation of the electrons from the valence band (VB) of the perovskite material to the conduction band (CB). Thus, exciton (a bound pair of electron and hole) is formed. A peculiar property of halide perovskites partially responsible for their unique photovoltaic performance is extremely low exciton binding energy which allows for nearly instant generation of free charge carriers. Following the dissociation of the exciton, electrons and holes move into ETL and hole-transport layer (HTL), respectively, where they are extracted from the perovskite and move further to the corresponding electrodes. Most often, one of these electrodes is transparent to allow the passage of the light to the active layer. Transparent conductive oxides (TCO) such as indium-tin oxide, fluorine-doped tin oxide (FTO), aluminum-doped zinc oxide (AZO), etc., are frequently used as materials for this electrode. The other electrode is typically opaque. Depending on the sequence of the layers in PSC they can be characterized as having n-i-p (also referred to as "conventional") or p-i-n (also called "inverted") configuration. In the first case, ETL is placed on top of the transparent electrode followed by the perovskite/HTL/opaque electrode stack. In contrast, in p-i-n structure CTLs come in the reversed order [9]. An illustration of both configurations is presented in Fig. 1.

The need for the introduction of two additional charge-transport layers in PSC is justified by the necessity of spatial separation of the positive and negative charge carriers. If such separation is not achieved, the charge carriers would undergo recombination on their way to the electrodes which will drastically decrease the power conversion efficiency (PCE) of the cell [10].

This factor determines the major requirement for CTLs. They need to simultaneously have an ability to efficiently extract and transport charge carriers of their corresponding type (electrons for ETL and holes for the HTL) and completely block the transport of the opposite type. This is achieved by the selection of the materials with the proper band alignment for CTLs. The diagram presented on the Fig. 2 shows an example of the energy level alignment in the perovskite solar cell and illustrates the principle of charge separation. To facilitate the extraction of the electrons the electron transport material (ETM) should have the position of the conduction band close to the perovskite's CB. Similarly, hole-transport material's (HTM's) valence band should be as close to the perovskite's VB as possible. At the same time, the need to block the transport of holes through the ETL and electrons through the HTL places another limitation. The VB of ETM needs to be much lower than that of the perovskite, and CB of HTL has to be significantly higher than the perovskites. Such an alignment creates a driving force for the selective extraction of the charge carriers in the respective layers and a potential barrier for the countermovement of charges [11].

Since this paper is primarily concerned with ETMs, several inorganic ETMs reported in the literature are shown on the scheme [12]-[14]. For all other layers, the most frequently used materials are selected.

Achieving a good band alignment is crucial for obtaining high-performance PSCs since it directly affects its photovoltaic characteristics (mainly open-circuit voltage, V_{oc}). It should be noted that all of these oxide-based ETMs satisfy the criteria of band alignment stated above (except for of WO_3 having the position of CB slightly lower than the desired level). Therefore, from this point of view, they all are viable candidates for PSCs.

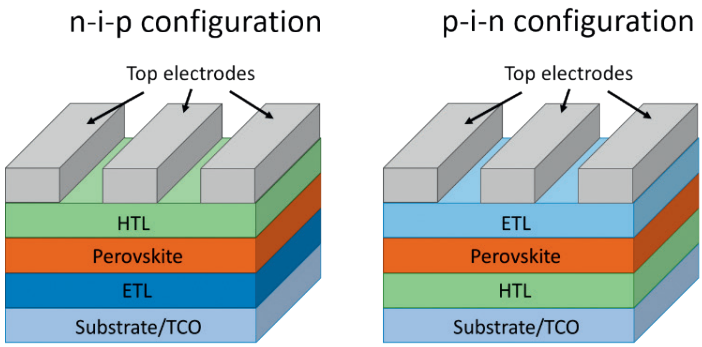

Fig. 1. Schematic illustration of the PSC architecture in n-i-p and p-i-n configurations

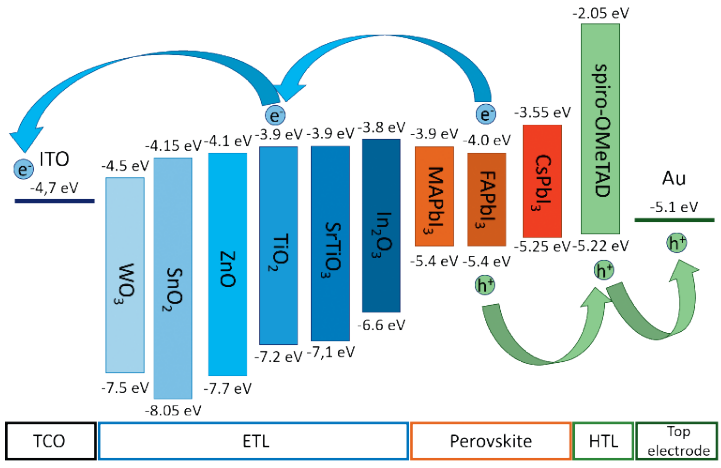

Fig. 2. Energy level alignment in the perovskite solar cells and the scheme of charge carrier separation

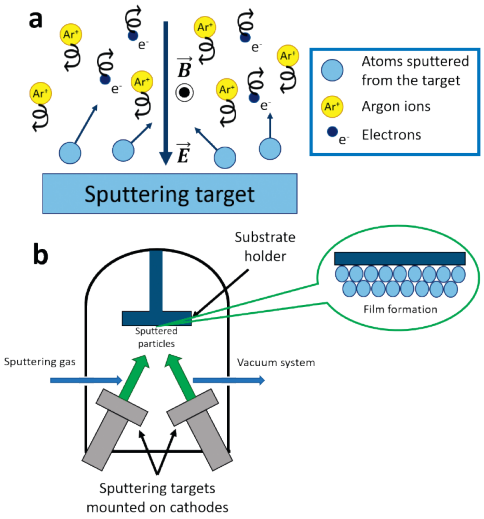

Fig. 3. a – The mechanism of magnetron sputtering; b – Schematic illustration of the magnetron sputtering setup

IV. BASICS OF MAGNETRON SPUTTERING

Magnetron sputtering (MS) is a method of material deposition belonging to the so-called physical vapor deposition (PVD) type of techniques. Fig. 3 illustrates the basic scheme of this process.

Since it is a vacuum-based technology, the process is carried out at low pressures (typical range is 10^{-4} – 10^{-2} mbar). Only a very small amount of sputtering gas necessary for the ignition of the plasma is present in the sputtering chamber. The sputtered material is present in the form of a dense and uniform sputtering target mounted on the cathode of the sputtering system. During the deposition process perpendicular electric and magnetic fields are generated near the target. This causes electrons (presented in a very small concentration in the sputtering gas) to accelerate in the direction orthogonal to the target. They move by the spiral trajectories and collide with the atoms of the sputtering gas. If these electrons have high enough energy, such collisions cause ionization of the sputtering gas, thus, forming the plasma. The electrons emitted from these collisions are in turn accelerated by the field and ionize more gas atoms creating an ionization cascade.

After the ionization, the ions of sputtering gas move by similar spiral trajectories towards the target and bombard the surface of the target. The impact of the gas ions may transfer the amount of energy sufficient for the target atoms to leave the surface. In this case they are ejected in all directions. Some of these particles eventually aggregate on the substrates which are typically fixed above the target [8], [15].

Most often, argon is used as a sputtering gas due to its inert nature and relative abundance. However, there are exceptions to this. For instance, to sputter light elements (such as carbon) it can be beneficial to use other light gases (i.e. neon) [16] while heavier gases (krypton, xenon) are better suited for heavy metals (tungsten etc.) [17] due to the better transfer of momentum between the particles. However, in practice they are rarely used because of their high cost.

Sputtering technique allows the deposition of any material that will not irreversibly decompose under the bombardment of the argon ions. It is a straightforward and frequently employed method for deposition of metals, metal oxides and nitrides as well as some other (mainly inorganic) materials. However, it should be noted that in case of dielectric materials (most of semiconductors also falls into this category) there is one additional problem. The bombardment of the target with the charged particles leads to the accumulation of the charge on it, which distorts electrical field in the its vicinity. Therefore, shortly after the beginning the sputtering process would be impossible. To overcome this issue, radiofrequency (RF) mode of sputtering is employed. In this mode the anode-cathode bias is alternated with high frequency (13.56 MHz is established as standard frequency). Such alternation prevents the charge accumulation and allows the deposition of dielectric materials. In contrast, conducting materials (metals, graphite, some of the TCOs etc.) can be deposited both in direct current (DC) and RF modes [8].

There are several important features that distinguish magnetron sputtering from other PVD techniques. First, the sputtered particles undergo a series of collisions with the sputtering gas atoms on their way to the substrate. A consequence of this is a significant scattering of such particles, which in turn leads to the elimination of shadowing effects in MS and good coverage of the surfaces with the complex profile (e.g. step coverage).

Second, there are a lot of parameters that can be changed during the deposition – sputtering gas pressure (which determines the number of collisions between the particles and their mean free path), sputtering power, substrate temperature and many others. It is also possible to apply bias to the substrates, inducing the ion bombardment of their surface to influence the morphology of the formed film. These variables make the deposition process much more complicated but simultaneously allow a tremendous degree of control to the skilled specialist.

One of the most important features of MS is the possibility to switch from the purely PVD process to a chemical vapor deposition (CVD). This is done by the introduction of the reactive gas into the sputtering chamber along with the sputtering gas. Most often, oxygen or nitrogen are employed as reactive gases to produce oxides and nitrides respectively [18]. As it will be shown later on in this paper, sometimes it can be a significant advantage in fabrication of high-quality films.

Aside from such versatility and controllability, magnetron sputtering has such important advantages as high reproducibility and uniformity of coatings coupled with a reasonable price and potential for integration with roll-to-roll processing. Assuming that TCO-based electrodes are typically produced by MS method, it is more than reasonable to use it in the processing of other layers of PSCs as well.

V. DEPOSITION OF ELECTRON TRANSPORT MATERIALS FOR PSCs USING MAGNETRON SPUTTERING

As it was mentioned earlier, a number of oxide materials was employed as ETMs for perovskite photovoltaics. All of them can be processed using magnetron sputtering technique. However, up to date a relatively small number of reports featuring sputtering deposition of metal oxides for this purpose has been published. Moreover, these published papers make use of only three most common oxides – titanium dioxide (TiO_2), zinc oxide (ZnO) and tin oxide (SnO_2) [19]. Therefore, in this chapter a brief overview of the current state-of-the-art achievements in this field will be presented with the emphasis on the major approaches to improve the quality of the obtained ETLs. After that, several possible directions for further development will be highlighted.

A. Presence of reactive gas and surface defects control

The presence or absence of reactive environment is one of the most influential aspects of the high-quality oxide-based ETL fabrication for PSCs. The composition of the sputtering gas can strongly influence the presence of bulk and surface defects, and thus impact the conductivity of the film and interfacial recombination.

Magnetron sputtering was identified as a technique that provides the means of precise control over the presence of surface defects. TiO_2 being one of the most explored ETMs in PSCs is often processed by solution-based techniques. However, it was shown that resulting films contain surface hydroxyl groups and other defects that decrease the PCE of the solar cell. Sputtered TiO_2, however, lacked such defects. Although the efficiency in this case (15.9%) was lower than in case of high-temperature solution-processed TiO_2 (16.6%), the fabrication process was fully compatible with the use of flexible PET substrates which was not allowed in case of high-temperature deposition. Moreover, sputtered TiO_2 provided reasonable efficiencies with layer thickness up to 100 nm [20]. Such a thick ETL can efficiently block the diffusion between active layer and the surrounding layers. Low sensitivity to ETL thickness was also reported for sputtered zinc oxide [21].

It was repeatedly shown that for SnO_2 to work as ETL it is extremely important to maintain a highly oxidative environment during the sputtering process. The main reason for that is the possibility of oxygen loss due to low pressure and sputtering damage. In oxygen deficient media Sn^{+4} can be partially reduced to Sn^{+2} which can compromise ETLs electron extraction and transport capabilities since SnO is a p-type semiconductor and can induce charge carrier recombination.

There is still some controversy as to what concentration of oxygen is the best. One paper suggested that O_2 content up to 90% leads to a more complete oxidation of Sn-O backbone and decreases the number of surface -OH groups, which can behave like shallow electron trap states. That fact was confirmed by X-ray photoelectron spectroscopy (XPS) studies of the sputtered films. Further increase of O_2 content didn't show any significant improvement. In the same work a proper optimization of a thickness and sputtering rate led to the high PCE of 20.2% [22].

In another case, it was revealed that the slight deviation from the stoichiometry might be beneficial and $Ar:O_2$ ratio of 2:3 is the best because higher concentration of O_2 leads to the decrease in the oxygen vacancies concentration. And oxygen vacancies play a key role in SnO_x conductivity. In this case, a 18% PCE was achieved [13], [23].

However, in another report a very small O_2 concentration of 9% was used to sputter a high-quality tin oxide film from the ceramic target. An interesting addition to that is the fact that all other layers of the PSCs including light absorber (mixed-cation and mixed-halide perovskite) and HTL (copper phthalocyanine) were also vacuum-processed, which is an interesting concept for improvement of uniformity and reproducibility of thin films comprising PSC. Such an approach yielded 15.1% PCE [24]. A similar effect was observed later in another publication [25].

One way to combine the advantages of highly oxidative environment and high concentration of vacancies is to actively heat the substrates during the deposition. It was shown that in case of fully reactive SnO_x deposition using metal target a substrate heating can induce the formation of vacancies. This also lowers the CB position improving the band alignment with the perovskite. Electrochemical impedance spectroscopy (EIS) was used to prove better charge-transfer from the perovskite to high-vacancy tin oxide. However, after exceeding some temperature the decrease of the SnO_x transmittance made the overall PCE to drop slightly. Therefore, a careful balance of the deposition parameters is required to achieve the best results [26]. A similar result can be sometimes achieved by a simpler process of post-deposition annealing of ETL. It was shown that in PSCs employing TiO_2 deposited by MS technique PCE can be increased from 9.8% to 12.5% with the addition of the annealing step at 500 °C. The main improvement in this case came from the open-circuit voltage [27].

In case of zinc oxide, however, it was shown that the high O_2 concentration can have a negative impact on the PSCs characteristics. It was reported that the sputtering by pure argon causes a slight downshifting of ZnO CB which creates a higher driving force for charge transfer [28]. Another report contained evidence that there is an optimal O_2 concentration in plasma ($Ar:O_2$ ratio 1:4) that leads to the smallest number of defects. Simultaneously, such conditions promote the growth of larger grains [29]. Such varied influence of O_2 suggests a significant complexity of the process and dictates the need for a more comprehensive investigation of the oxygen influence on the ETL's properties.

In one of the most comprehensive studies of the sputtered zinc oxide films a straightforward way to influence the surface composition of ZnO was found. It was shown that the working pressure during the sputter deposition has a dramatic impact on the properties of obtained films. Higher pressure limits the energy of charged particles in the plasma and therefore reduces the number of defects in the films. XPS study of the samples sputtered at high and low working pressures revealed a significant decrease in the number of oxygen vacancies and chemisorbed hydroxyls on the surface. In addition to that, photoluminescence (PL) measurements were used to confirm better charge extraction capabilities of such films. Films sputtered at high pressure also were more hydrophobic, which led to the formation of larger perovskite grains on top of ZnO layer, beneficial for both stability and efficiency of PSCs. Another important factor that was underlined in this paper is the necessity to anneal ZnO just before the perovskite deposition to eliminate all adsorbed water, since it can induce a significant perovskite degradation at the interface. Such careful engineering of the deposition process led to the high PCE of 17.3% [30].

B. Texturing effect of the sputtered films

One of the most prominent examples of what could be achieved by magnetron sputtering in the context of ETLs for PSCs was the selective deposition of TiO_2 with the preferential {001} facets [31]. The authors of this report suggested that while {101} orientation is predominant in most of the sputtered titania films since it has the surface energy value twice as low compared to other orientations. This can be changed by a rational design of sputtering conditions. The reason for dominance of {101} facets in films lies in the stability of such facets which is caused by their high density. However, if a substrate bias is applied this same factor will reduce the stability of {101} facets dramatically, since the dense structures are much more susceptible to the sputtering. At the same time, {001} facets have ionic channels facing perpendicular to the surface allowing argon ions to pass deeper into the film dissipating their energy without sputtering TiO_2. After the application of the substrate bias, the formation of the films with predominant {001} facets was confirmed by XRD and high-resolution microscopy studies [31].

Further, the authors proved that {001} facets have much better charge extraction properties and form an excellent contact with the perovskite. The effect of this was clearly visible by the decrease of the PL intensity and significantly improved JSC and FF values of the fabricated devices. One more important factor is the morphology of the sputtered films. In case of the films sputtered under the substrate bias, a strong columnar orientation of the titania grains was observed which contributed to the conductivity of the films. In summary, this approach resulted in 17.25% PCE without any passivation coatings (compared to 15.6% for {101}-dominated samples) [31].

C. Sputtering for PSCs with inverted configuration

To date, most of the research groups working on magnetron sputtering of ETLs focused their attention on n-i-p configuration. It is easily explained by the fact that in case of p-i-n configuration ETL should be processed on top of the perovskite layer which produces added complications. It was reported several times that magnetron sputtering process can induce a significant damage to the underlying organic materials [32]. This also applies to the perovskite absorbers. Such damage causes a lot of defects to appear on the surface of the layer which leads to a significant charge carrier recombination and a decrease in photovoltaic performance of the devices. Although there have been some indications that it is possible to significantly reduce the sputter damage of the perovskite by a proper optimization of deposition regime [33], the more promising approach is the insertion of a buffer interlayer between the perovskite and ETL in this case.

Interestingly enough, one of the earliest reports on the use of sputtered ZnO in the PSCs featured p-i-n configuration. In this work a thin interlayer of fullerene C_{60} which is one of best organic n-type semiconductors was used to protect the perovskite surface from being damaged by plasma. Dark J-V measurements were carried out to confirm the improvement in the perovskite-ETL interface quality. It was also shown that the thickness of such interlayer is of vital importance. Too thin C_{60} layer was not able to prevent the sputtering damage by itself while too thick layer induced high series resistance in the PSC which in turn decreased the FF of the device. In both instances a suboptimal performance of the solar cells was observed. However, for optimal thickness of 15 nm a quite remarkable PCE of 10.9% was achieved which is higher than in the reference system employing a fullerene derivative [60]PCBM as the only ETM (10.6%). It should be noted that although this PCE is far from current records, it is still a considerable achievement given that both perovskite processing techniques made a huge progress in the recent years [34] and a large step in the understanding of the HTL influence on PSC performance was made. Consequently, PEDOT:PSS used in this work is no longer considered to be the best HTL for inverted PSCs and is typically substituted by some other materials such as nickel oxide or PTAA [35], [36]. Both of these improvements would most likely significantly enhance the PCE in this case [37].

Inspired by this work, another research group used the same approach to fabricate PSCs based on $FAPbBr_3$ perovskite material which has high bandgap. This is typically an undesirable property for a light absorber due to lower light harvesting. However, in case of perovskites it can sometimes be compensated by a high V_{oc} value and better stability. In this case a solution-processed fullerene derivative [60]PCBM was used as an interlayer. In addition to that, aqueous HBr was used to improve the surface topography of the perovskite film which is of paramount importance in case of sputtering on top of the perovskite. Such technique allowed to achieve 8.3% efficiency of $FAPbBr_3$-based solar cells which is considered to be a high PCE for this perovskite material [38].

D. ETM doping

While ETM doping can be easily done by co-sputtering from two different targets and is a potentially attractive way to improve the charge carrier mobility and tune the energy level alignment, it remains nearly unexplored in the context of PSCs.

Zinc oxide is the most frequently doped ETM in this context. A variety of different dopants can be used to improve its properties. One of such dopants is gallium. Ga^{+3} ion has similar ionic radius and M-O bond length to zinc which prevents a significant distortion of the ZnO structure during the doping. It was reported to be successfully processed by magnetron sputtering. The resulting films had favorable band alignment with the perovskite and higher charge carrier concentration than pristine ZnO. Additionally, they displayed a high transmittance (> 87 %) in wide spectral range. The computational simulation provided theoretical PCE of 21.1% for PSCs with such ETL. However, this calculation is yet to be tested in real devices [39].

Aluminum and fluorine were also tried as dopants [40]. The sputtered ZnO films that contained small amounts of ZnF_2 and Al_2O_3 additives demonstrated improved charge carrier mobility and concentration values. Also, they possess a high transmittance in near infra-red spectral range, which is highly important in case of potential manufacturing of tandem solar cells. A PCE of more than 15% was achieved in this work. The only major downside of this method is high substrate temperature (320 °C for optimal conditions) during the deposition, which limits its use in p-i-n or flexible devices [40].

Magnesium doping of ZnO has also been proved to be an effective way to tailor ETM's CB position and bandgap. It can be readily achieved by co-sputtering of ZnO and MgO targets while keeping substrates at room temperature. However, while Mg-doped ZnO has higher transparency and favorable band alignment, its resistivity is increased by the addition of Mg^{+2} ions leading to the decrease of J_{SC} value and overall PCE of the device [41].

Tin oxide is not as frequently doped as ZnO for use as ETM. Typically, doped SnO_2 is used as TCO. However, there has been a report featuring tantalum as a potential dopant for SnO_2. The optimized film sputtered at substrate temperature of 270 °C had a combination of high transmittance and low resistivity. Unfortunately, this material hasn't been tested in PSCs for now [42].

VI. POTENTIAL FOR FUTURE RESEARCH

As it was stated above, magnetron sputtering provides a huge number of parameters that can be changed to influence the deposition process. The examples presented in this article clearly demonstrate a tremendous impact of these parameters on the performance of PSCs. Therefore, a deeper understanding of their impact is required to achieve the best possible PCE.

The absence of consensus on the exact influence of oxygen during the ETM sputtering is one of the most puzzling phenomena. Although a great amount of work has been done in this area, a more comprehensive study of this matter is needed to find out the optimal balance between oxygen vacancies-induced increase of ETM's conductivity and the number of surface defects that lead to a higher rate of charge carrier recombination.

Another unexplored domain is ETMs beyond TiO_2, SnO_2 and ZnO. A number of different ETLs has been reported that can be processed by MS. For example, solution-processed $BaTiO_3$ – a perovskite oxide was used as a thin coating on top of mesoporous TiO_2. An increase of all photovoltaic parameters was observed with the use of such coating leading to the PCE growth from 16.1% to 17.9% [43]. Moreover, sputtered $BaTiO_3$ has already been used as UV-blocking and tunable antireflection coating for other photovoltaic technologies [44], [45]. Therefore, it seems to be a good candidate for testing as a potential sputtered ETL for PSCs.

Another perovskite oxide, $SrTiO_3$ has also been used as electron transport material for highly efficient PSCs [46]-[48]. The same applies to indium oxide In_2O_3 that was used both as a standalone ETL and in combination with other ETMs [49]-[51]. Similarly, ZrO_2 has been reported as a potential alternative to titanium dioxide [52]. One more metal oxide that was used as ETM in PSCs is WO_3. The PSCs fabricated using this ETM demonstrated a very low hysteresis. However, it was shown that WO_3 is extremely sensitive to the presence of defects [53] and MS provides unrivaled potential for defect tuning in metal oxides.

The facts presented above justify the screening of additional sputtered metal oxides besides those already used in PSCs, since a proper optimization of such ETMs can lead to a significant improvement in the solar cell performance.

And finally, although PCE of PSCs using sputtered ETLs was an object of thorough optimization, another vital aspect of its performance was left nearly without investigation until now. The stability of PSCs is the weakest point of this technology. And here a good control over the interface quality provided by MS can allow for a significant breakthrough. It is especially attractive to deposit a dense and thick CTL on top of the perovskite layer to trap its volatile decomposition products inside. Therefore, a systematic investigation of the impact of several different ETMs processed under various conditions on the stability of PSCs is highly desirable.

VII. CONCLUSION

Magnetron sputtering is a powerful technique that can be employed in perovskite photovoltaics. A large set of tools in the form of various deposition parameters such as working pressure, sputtering gas composition, substrate temperature and bias, etc. provided by this method allows for a precise control over the deposition process and highly efficient engineering of the deposited film properties. To date, three electron transport materials – TiO_2, SnO_2 and ZnO were thoroughly optimized for use as sputtered ETMs for PSCs. In many cases such optimized layers led to PCE higher than in the reference systems employing solution-processed ETLs. Additional benefit of using MS for industry is high uniformity and reproducibility of coatings necessary for large-scale production of solar panels. Furthermore, there is a huge potential for further development such as the additional screening of different materials, optimization of their structure and stoichiometry and assessment of their influence on PSCs stability.

VIII. REFERENCES

[1] A. Kojima, K. Teshima, Y. Shirai, and T. Miyasaka, "Organometal Halide Perovskites as Visible-Light Sensitizers for Photovoltaic Cells," J. Am. Chem. Soc., vol. 131, no. 17, pp. 6050–6051, May 2009.

[2] "Best research-cell efficiency chart, NREL." https://www.nrel.gov/pv/cell-efficiency.html (accessed Mar. 30, 2020).

[3] H. Li, C. Zuo, A. D. Scully, D. Angmo, J. Yang, and M. Gao, "Recent progress towards roll-to-roll manufacturing of perovskite solar cells using slot-die processing," Flex. Print. Electron., vol. 5, no. 1, p. 014006, Jan. 2020.

[4] M. Cai, Y. Wu, H. Chen, X. Yang, Y. Qiang, and L. Han, "Cost-Performance Analysis of Perovskite Solar Modules," Adv. Sci., vol. 4, no. 1, p. 1600269, Jan. 2017.

[5] R. Wang, M. Mujahid, Y. Duan, Z. Wang, J. Xue, and Y. Yang, "A Review of Perovskites Solar Cell Stability," Adv. Funct. Mater., vol. 29, no. 47, p. 1808843, Nov. 2019.

[6] S. F. Hoefler, G. Trimmel, and T. Rath, "Progress on lead-free metal halide perovskites for photovoltaic applications: a review," Monatsh Chem., vol. 148, no. 5, pp. 795–826, May 2017.

[7] A. F. Akbulatov et al., "Probing the Intrinsic Thermal and Photochemical Stability of Hybrid and Inorganic Lead Halide Perovskites," J. Phys. Chem. Lett., vol. 8, no. 6, pp. 1211–1218, Mar. 2017.

[8] G. Bräuer, "Magnetron Sputtering," in Comprehensive Materials Processing, Elsevier, 2014, pp. 57–73.

[9] A. K. Jena, A. Kulkarni, and T. Miyasaka, "Halide Perovskite Photovoltaics: Background, Status, and Future Prospects," Chem. Rev., vol. 119, no. 5, pp. 3036–3103, Mar. 2019.

[10] J.-P. Correa-Baena et al., "Promises and challenges of perovskite solar cells," Science, vol. 358, no. 6364, pp. 739–744, Nov. 2017.

[11] Z. Song, S. C. Watthage, A. B. Phillips, and M. J. Heben, "Pathways toward high-performance perovskite solar cells: review of recent advances in organo-metal halide perovskites for photovoltaic applications," J. Photon. Energy, vol. 6, no. 2, p. 022001, Apr. 2016.

[12] K. Mahmood, S. Sarwar, and M. T. Mehran, "Current status of electron transport layers in perovskite solar cells: materials and properties," RSC Adv., vol. 7, no. 28, pp. 17044–17062, 2017.

[13] G. Bai et al., "High performance perovskite sub-module with sputtered SnO_2 electron transport layer," Solar Energy, vol. 183, pp. 306–314, May 2019.

[14] Y. You, W. Tian, L. Min, F. Cao, K. Deng, and L. Li, "TiO_2 /WO_3 Bilayer as Electron Transport Layer for Efficient Planar Perovskite Solar Cell with Efficiency Exceeding 20%," Adv. Mater. Interfaces, vol. 7, no. 1, p. 1901406, Jan. 2020.

[15] P. J. Kelly and R. D. Arnell, "Magnetron sputtering: a review of recent developments and applications," Vacuum, vol. 56, no. 3, pp. 159–172, Mar. 2000.

[16] P. C. Zalm, "Energy dependence of the sputtering yield of silicon bombarded with neon, argon, krypton, and xenon ions," J. Appl. Phys., vol. 54, no. 5, pp. 2660–2666, May 1983.

[17] C. Paturaud, G. Farges, M. C. Sainte Catherine, and J. Machet, "Influence of sputtering gases on the properties of magnetron sputtered tungsten films," Surface and Coatings Technology, vol. 86–87, pp. 388–393, Dec. 1996.

[18] J. Musil, P. Baroch, J. Vlček, K. H. Nam, and J. G. Han, "Reactive magnetron sputtering of thin films: present status and trends," Thin Solid Films, vol. 475, no. 1–2, pp. 208–218, Mar. 2005.

[19] K. Mahmood, S. Sarwar, and M. T. Mehran, "Current status of electron transport layers in perovskite solar cells: materials and properties," RSC Adv., vol. 7, no. 28, pp. 17044–17062, Mar. 2017.

[20] S. S. Mali, C. K. Hong, A. I. Inamdar, H. Im, and S. E. Shim, "Efficient planar n-i-p type heterojunction flexible perovskite solar cells with sputtered TiO_2 electron transporting layers," Nanoscale, vol. 9, no. 9, pp. 3095–3104, Mar. 2017.

[21] L. Liang et al., "Magnetron Sputtered Zinc Oxide Nanorods as Thickness-Insensitive Cathode Interlayer for Perovskite Planar-Heterojunction Solar Cells," ACS Appl. Mater. Interfaces, vol. 6, no. 23, pp. 20585–20589, Dec. 2014.

[22] L. Qiu et al., "Scalable Fabrication of Stable High Efficiency Perovskite Solar Cells and Modules Utilizing Room Temperature Sputtered SnO_2 Electron Transport Layer," Adv. Funct. Mater., vol. 29, no. 47, p. 1806779, Nov. 2019.

[23] H. Tao et al., "Room-temperature processed tin oxide thin film as effective hole blocking layer for planar perovskite solar cells," Appl. Surf. Sci., vol. 434, pp. 1336–1343, Mar. 2018.

[24] M. Kam, Y. Zhu, D. Zhang, L. Gu, J. Chen, and Z. Fan, "Efficient Mixed-Cation Mixed-Halide Perovskite Solar Cells by All-Vacuum Sequential Deposition Using Metal Oxide Electron Transport Layer," Sol. RRL, vol. 3, no. 7, p. 1900050, Jul. 2019.

[25] W. Sun et al., "Reactive-Sputtered Prepared Tin Oxide Thin Film as an Electron Transport Layer for Planar Perovskite Solar Cells," Coatings, vol. 9, no. 5, p. 320, May 2019.

[26] F. Ali et al., "Tuning the Amount of Oxygen Vacancies in Sputter-Deposited SnO_x films for Enhancing the Performance of Perovskite Solar Cells," ChemSusChem, vol. 11, no. 18, pp. 3096–3103, Sep. 2018.

[27] S. Ge et al., "The improvement of open circuit voltage by the sputtered TiO_2 layer for efficient perovskite solar cell," Vacuum, vol. 128, pp. 91–98, Jun. 2016.

[28] Z.-L. Tseng, C.-H. Chiang, and C.-G. Wu, "Surface Engineering of ZnO Thin Film for High Efficiency Planar Perovskite Solar Cells," Sci Rep, vol. 5, no. 1, p. 13211, Oct. 2015.

[29] W. Zhao et al., "Stoichiometry control of sputtered zinc oxide films by adjusting Ar/O_2 gas ratios as electron transport layers for efficient planar perovskite solar cells," Solar Energy Materials and Solar Cells, vol. 178, pp. 200–207, May 2018.

[30] A. Thote et al., "High-Working-Pressure Sputtering of ZnO for Stable and Efficient Perovskite Solar Cells," ACS Appl. Electron. Mater., vol. 1, no. 3, pp. 389–396, Mar. 2019.

[31] A. Huang et al., "Achieving High Current Density of Perovskite Solar Cells by Modulating the Dominated Facets of Room-Temperature DC Magnetron Sputtered TiO_2 Electron Extraction Layer," ACS Appl. Mater. Interfaces, vol. 9, no. 3, pp. 2016–2022, Jan. 2017.

[32] S. Dangtip et al., "Study of low power deposition of ITO for top emission OLED with facing target and RF sputtering systems," J. Phys.: Conf. Ser., vol. 100, no. 4, p. 042011, Mar. 2008.

[33] B. A. Nejand, V. Ahmadi, S. Gharibzadeh, and H. R. Shahverdi, "Cuprous Oxide as a Potential Low-Cost Hole-Transport Material for Stable Perovskite Solar Cells," ChemSusChem, vol. 9, no. 3, pp. 302–313, Feb. 2016.

[34] Z. Shi and A. Jayatissa, "Perovskites-Based Solar Cells: A Review of Recent Progress, Materials and Processing Methods," Materials, vol. 11, no. 5, p. 729, May 2018.

[35] Z. H. Bakr, Q. Wali, A. Fakharuddin, L. Schmidt-Mende, T. M. Brown, and R. Jose, "Advances in hole transport materials engineering for stable and efficient perovskite solar cells," Nano Energy, vol. 34, pp. 271–305, Apr. 2017.

[36] X. Yang, H. Wang, B. Cai, Z. Yu, and L. Sun, "Progress in hole-transporting materials for perovskite solar cells," J. Energy Chem., vol. 27, no. 3, pp. 650–672, May 2018.

[37] W.-C. Lai, K.-W. Lin, T.-F. Guo, P. Chen, and Y.-T. Wang, "Conversion efficiency improvement of inverted $CH_3NH_3PbI_3$ perovskite solar cells with room temperature sputtered ZnO by adding the C_{60} interlayer," Appl. Phys. Lett., vol. 107, no. 25, p. 253301, Dec. 2015.

[38] A. S. Subbiah, S. Agarwal, N. Mahuli, P. Nair, M. van Hest, and S. K. Sarkar, "Stable p-i-n $FAPbBr_3$ Devices with Improved Efficiency Using Sputtered ZnO as Electron Transport Layer," Adv. Mater. Interfaces, vol. 4, no. 8, p. 1601143, Apr. 2017.

[39] Y. Chen, Y. Hu, Q. Meng, H. Yan, W. Shuai, and Z. Zhang, "Natively textured surface of Ga-doped ZnO films electron transporting layer for perovskite solar cells: further performance analysis from device simulation," J Mater Sci: Mater. Electron., vol. 30, no. 5, pp. 4726–4736, Mar. 2019.

[40] X. Ji et al., "Fabrication of high-performance F and Al co-doped ZnO transparent conductive films for use in perovskite solar cells," Solar Energy Materials and Solar Cells, vol. 190, pp. 6–11, Feb. 2019.

[41] J. Chantana et al., "Micro-scale current path distributions of Zn_1-Mg O-coated SnO_2:F transparent electrodes prepared by sol-gel and sputtering methods in perovskite solar cells," Thin Solid Films, vol. 669, pp. 455–460, Jan. 2019.

[42] N. M. Nguyen et al., "Synthesis of Tantalum-Doped Tin Oxide Thin Filmsby Magnetron Sputtering for Photovoltaic Applications," J. Elec. Mater., vol. 46, no. 6, pp. 3667–3673, Jun. 2017.

[43] J. Qin, Z. Zhang, W. Shi, Y. Liu, H. Gao, and Y. Mao, "Enhanced Performance of Perovskite Solar Cells by Using Ultrathin $BaTiO_3$ Interface Modification," ACS Appl. Mater. Interfaces, vol. 10, no. 42, pp. 36067–36074, Oct. 2018.

[44] A. K. Sharma, B. G. Priyadarshini, B. R. Mehta, and D. Kumar, "An amorphous barium titanate thin film improves light trapping in Si solar cells," RSC Adv., vol. 5, no. 74, pp. 59881–59886, Jul. 2015.

[45] Ľ. Scholtz, P. Šutta, P. Calta, P. Novák, M. Solanská, and J. Müllerová, "Investigation of barium titanate thin films as simple antireflection coatings for solar cells," Appl. Surf. Sci., vol. 461, pp. 249–254, Dec. 2018.

[46] M. Neophytou et al., "Enhancing the Charge Extraction and Stability of Perovskite Solar Cells Using Strontium Titanate (SrTiO3) Electron Transport Layer," ACS Appl. Energy Mater., vol. 2, no. 11, pp. 8090–8097, Nov. 2019.

[47] T. Mahmoudi, Y. Wang, and Y. Hahn, "$SrTiO_3/Al_2O_3$ -Graphene Electron Transport Layer for Highly Stable and Efficient Composites-Based Perovskite Solar Cells with 20.6% Efficiency," Adv. Energy Mater., vol. 10, no. 2, p. 1903369, Jan. 2020.

[48] Y. Okamoto, R. Fukui, M. Fukazawa, and Y. Suzuki, "$SrTiO_3/TiO_2$ composite electron transport layer for perovskite solar cells," Materials Letters, vol. 187, pp. 111–113, Jan. 2017.

[49] J. Dong et al., "Enhanced performance of TiO_2-based planar perovskite solar cells by In_2O_3 interfacial modification layer," Organic Electronics, vol. 75, p. 105426, Dec. 2019.

[50] P. Wang et al., "Gradient Energy Alignment Engineering for Planar Perovskite Solar Cells with Efficiency Over 23%," Adv. Mater., vol. 32, no. 6, p. 1905766, Feb. 2020.

[51] S. Yoon et al., "Solution-processed indium oxide electron transporting layers for high-performance and photo-stable perovskite and organic solar cells," Nanoscale, vol. 9, no. 42, pp. 16305–16312, 2017.

[52] D. Bi et al., "Using a two-step deposition technique to prepare perovskite ($CH_3NH_3PbI_3$) for thin film solar cells based on ZrO_2 and TiO_2 mesostructures," RSC Adv., vol. 3, no. 41, p. 18762, Jul. 2013.

[53] F. Ali et al., "Low Hysteresis Perovskite Solar Cells Using an Electron-Beam Evaporated WO_{3-x} Thin Film as the Electron Transport Layer," ACS Appl. Energy Mater., vol. 2, no. 8, pp. 5456–5464, Aug. 2019.

Note

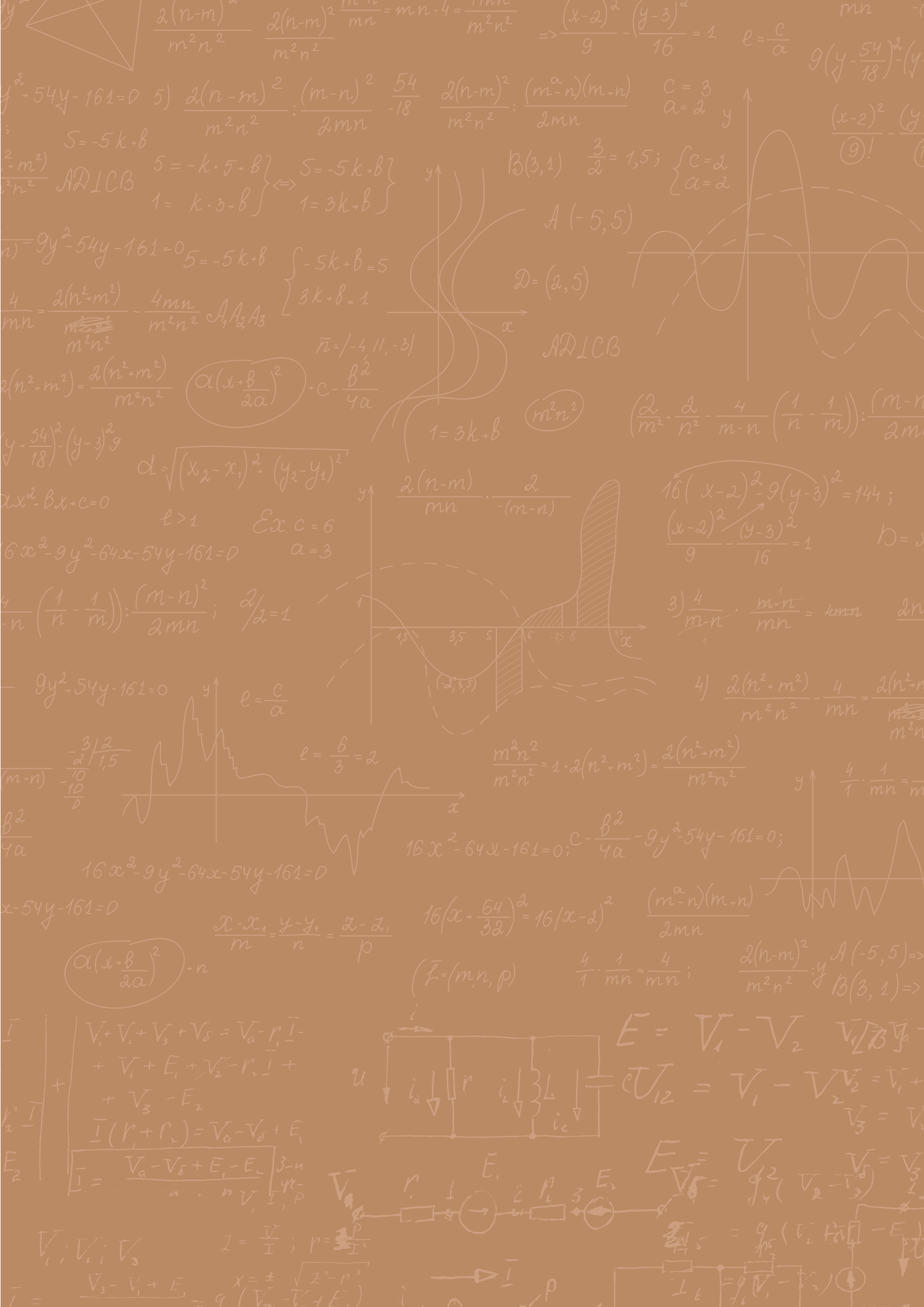

Skolkovo Institute of Science and Technology
Bolshoy Boulevard 30, bld. 1
www.skoltech.ru/en